Eindhoven University of Technology

Characterization and reactivity of olivine and model catalysts for biomass gasification

Document Version:

Publisher's PDF, also known as Version of Record (includes final page, issue and volume numbers)

Please check the document version of this publication:

• A submitted manuscript is the version of the article upon submission and before peer-review. There can be important differences between the submitted version and the official published version of record. People interested in the research are advised to contact the author for the final version of the publication, or visit the DOI to the publisher's website.
• The final author version and the galley proof are versions of the publication after peer review.
• The final published version features the final layout of the paper including the volume, issue and page numbers.

Link to publication

Characterization and Reactivity of Olivine and Model Catalysts for Biomass Gasification

PROEFSCHRIFT

ter verkrijging van de graad van doctor aan de
Technische Universiteit Eindhoven,
op gezag van de rector magnificus prof.dr.ir. C.J. van Duijn,
voor een commissie aangewezen
door het College voor Promoties,
in het openbaar te verdedigen
op woensdag 26 november 2014 om 16:00 uur

door

Remco Johannes Lancee

geboren te Utrecht

Dit proefschrift is goedgekeurd door de promotoren en de samenstelling van de promotiecommissie is als volgt:

Voorzitter:	prof.dr. D.J. Broer
Eerste promotor:	prof.dr. J.W. Niemantsverdriet
Tweede promotor:	prof.dr. H.J. Veringa
Copromotor:	dr. H.O.A. Fredriksson
Leden:	prof.dr. S.R.A. Kersten (Universiteit Twente)
	Univ.Prof.Dipl.-Ing.Dr.techn. H. Hofbauer
	(Technische Universität Wien)
	prof.dr.ir. E.J.M. Hensen
Adviseur:	dr.ing. C.M. van der Meijden (ECN)

"Be yourself. Unless you can be a unicorn,
In that case, you should always be a unicorn"

Elle Lothlorien, *Alice in Wonderland*

"Life is what happens to you while you're busy making other plans"

John Lennon in *Beautiful Boy*

Characterization and Reactivity of Olivine and Model Catalysts for Biomass Gasification

Remco J. Lancee

CONTENTS

Characterization and Reactivity of Olivine and Model Catalysts for Biomass Gasification

To meet the increasing demand for renewable, CO_2-neutral energy, biomass (in particular waste products) can be used for the production of fuels, such as hydrogen, synthetic natural gas or Fischer-Tropsch diesel. Conversion of biomass to fuels can be performed using gasification as an initial step in the conversion. The resulting primary products CO, H_2, CO_2 and CH_4 can then easily be used within present infrastructure.

Amongst the different gasification techniques, fluidized-bed gasification is preferred for biomass. However, a major disadvantage of the conventional biomass gasification process is the high concentration of N_2 in the product gas, resulting from the partial combustion of biomass with air. This can be avoided by using indirect fluidized-bed gasification. In indirect gasification, the combustion and gasification take place in separate reactor vessels, which are coupled together. This type of reactor, where a circulating bed material is used to transport the heat from the combustion zone to the gasification zone, is therefore also referred to as a dual fluidized-bed reactor. Although this approach avoids the problems associated with N_2, one of the main problems of biomass gasification still remains, namely the formation of tars, that pollute the product gases and the reactor.

By using a catalytically active bed material during gasification, it is possible to improve the efficiency of the process and to reduce the content of tars in the product gas. Olivine $((Mg,Fe)_2SiO_4)$ is widely used as an active bed material for catalytic cracking of tars during gasification of biomass in dual fluidized-bed reactors. The elemental composition, addition of Fe and high temperature treatments influence the catalytic properties of this mineral. However, olivine is not a stable material under process conditions, relevant for biomass gasification.

Moreover, the exact catalytic function of olivine is not yet fully understood. The central questions of this research are thus: How does olivine

change during exposure to the different conditions, representative for gas environments present in indirect biomass gasification reactors and how does this behavior relate to the performance of olivine as a biomass gasification catalyst?

The dynamic behavior of olivine under realistic model conditions, i.e. alternatingly oxidizing and reducing gas environments at 750 °C, is presented in chapter 3. Significant changes in phase composition of the material, depending on the gas composition and the duration of the treatments, were found using XPS, XRD, XAS and SEM. A large fraction of the iron, both in the bulk and at the surface of the investigated material, is present as free Fe-phases, which are sensitive to changes in the gas environment. In addition, the elemental composition of the surface changes dramatically depending on the gas composition. After exposure to oxidizing environments, the amount of Fe at the surface is twice as high as after reduction. Furthermore, the reduction of the iron oxides upon switching from oxidizing to reducing conditions shows that olivine can transport oxygen from the combustor into the gasifier.

Chapter 4 describes the capability of olivine to transport oxygen in greater detail. Mössbauer spectroscopy confirmed that during oxidation, iron segregates out of the olivine matrix, forming free iron oxide phases. Thermo Gravimetric Analysis (TGA) was used to quantify oxygen transport under alternating oxidizing/reducing conditions. The TGA results indicate that at least 18% of the iron, present in olivine, participates in the oxygen-transfer process, on the time scale of minutes. XPS, combined with depth profiling, provided further insight into the dynamic behavior of olivine under relevant conditions. Iron enrichment at the surface is observed after oxidation and upon subsequent reduction, the iron quickly redistributes in the olivine towards the original, more homogeneous distribution.

During long term, continuous use as bed material in biomass gasification, olivine gets coated by materials stemming from the biomass ash. The nature of this bed material coating and the influence of the coating on the catalytic reactivity is described in chapter 5. SEM-EDS analysis showed that already after 30 h of biomass gasification, a surface layer, containing calcium and potassium, is formed on olivine. XPS depth profiling showed

that this Ca- and K-rich surface layer also contains carbonate species and is more than 0.5 micrometer thick. A mechanism for the coating of the bed material is proposed, involving iron segregation to the surface during the first stages of use of olivine as a bed material. Ash compounds are incorporated in this surface layer, in which Fe is still mobile and K is able to penetrate deep into the particles, because of its volatility.

The WGS-activity of the ash-coated olivine is almost a factor 5 higher than that of uncoated material. Biomass ash compounds were also found to be WGS active and are known to be active towards tar reduction as well.

Since natural olivine is, as most minerals, an inhomogeneous material, it is not well suited for studying the iron - silica interaction in detail. The goal of the research described in chapter 6 was to prepare a high surface area model catalyst, involving uniform, colloidal Fe-nanoparticles, dispersed on a spherical, non-porous support. Such a model catalyst represents a convenient compromise between the high surface area porous industrial catalysts and the planar model catalyst, for detailed model studies of the correlation between catalyst composition, morphology and reactivity. Monodisperse SiO_2 spheres with diameters between 850 - 900 nm have been be synthesized and impregnated with iron nanoparticles. The resulting, well defined Fe/SiO_2 model catalyst can be studied with both electron microscopy and XPS on one hand and with XRD and other bulk characterization techniques on the other hand.

The work described in this thesis contributes with important information on the fundamental properties of olivine, used as catalytically active bed material in indirect biomass gasification. Significant changes in surface chemistry and morphology were observed. Iron, a well-known catalytic material, is highly mobile in olivine. This high mobility leads to the formation of free Fe-oxide phases, in turn resulting in redox behavior and oxygen transport. Moreover, during use in biomass gasification, a Ca- and K-rich layer forms on the bed material, which influences its reactivity.

These observations contribute to revealing the details of the catalytic processes in biomass gasification and will help selecting the optimal process conditions to achieve optimal performance of olivine as a catalyst in indirect gasification reactors.

1

Introduction

1.1 BIOMASS

The depletion of conventional coal, gas and oil, which are currently the most important sources for fuels, and growing climatologic problems are forcing us to develop new technologies that enable a more sustainable society. An additional driver for the use of non-fossil fuel resources is energy security, as the majority of fossil fuels is produced in politically unstable regions. As a consequence, new ways to meet our energy needs have to be considered. Most likely, multiple energy sources will be used, preferably renewable ones, like solar, wind and biomass.

Renewable energy sources will play an increasingly significant role in energy supply to meet the growing demand. In 2013, renewables amounted to 280 million tons of oil equivalent in energy use, which is only 2.2% of the total energy use in the world, according to the BP statistical review [1]. Their expected growth rate is 6.4% per year and renewables and other new fuel sources are predicted to contribute to 43% of the increment in energy production to 2035 [2].

For centuries, biomass has been the largest primary energy source in the world, and now, this role has been taken over by coal, oil and gas. In principle, biomass is defined as all biological material originating from (recently) living organisms. However, when considering biomass as an energy source, this is mostly limited to plants and plant-based materials. One of the main reasons for the renewed interest in biomass as a renewable energy source, is that it can be considered CO_2 neutral. The CO_2 that is released during combustion of biomass was taken up from the atmosphere during its growth, thereby closing the carbon cycle. If biomass is not combusted, but used to produce liquid fuels or hydrogen, it can even become a CO_2 negative fuel, provided that part of the CO_2 that is produced during these processes can be separated and sequestrated.

In contrast to solar and wind, biomass is the only renewable energy source that contains carbon, which allows direct conversions to fuels and chemicals. The amount of fuels and chemicals, produced from biomass will grow rapidly in the coming decades. According to the Shell Energy Scenario from 2008, biomass is expected to represent around 15% of the yearly primary energy use by 2050 [3].

However, the use of biomass for energy and fuels is not without controversy, since some energy crops like corn and sugar cane can be used either as food or as (source for) biofuels. The use of land for growing energy crops instead of crops used for food, led to a dramatic increase in world food prices during late 2007 and early 2008 [4]. Therefore, attention has shifted to biomass sources that do not compete with food production. The fuels derived from this kind of biomass is referred to as second generation biofuels or advanced biofuels (bio-ethanol, bio-oil, bio-diesel etc.).

The conversion processes of biomass to heat, fuels or chemical can roughly be divided in two categories: bio-chemical conversion and thermo-chemical conversion. The bio-chemical processes, fermentation, anaerobic digestion and composting, make use of bacteria, enzymes or other microorganisms to convert the biomass into more useful forms. Thermo-chemical processes can be divided in combustion, torrefaction, pyrolysis and gasification, depending on the process temperature and oxygen partial pressure. The focus of the work presented in this thesis lays on gasification, which is the partial oxidation of biomass at temperatures, typically in the range 800 - 900 °C [5].

1.2   CATALYSIS AND CATALYSTS

Catalysts are the workhorses of today's chemical industry and play a vital role in the four most successful industrial sectors in the world: petroleum refining, chemicals production, energy generation and food production. The impact of catalysis on the world economy is enormous: the worldwide catalyst manufacturing industry was valued at 19.2 billion USD in 2012 and is expected to increase to over 24 billion USD in 2018 [6]. This may seem a relatively small number, but it is estimated that the total impact of catalysis and catalytic processes is more than 10 trillion USD per year, contributing to almost 20% of the world's GDP [7].

The term *catalysis* was first used by the Swedish chemist Jöns Jacob Berzelius in 1830. He stated that a catalyst influences the course of a reaction, but remains unchanged itself. This was also known as contact catalysis. Several years later, Faraday discovered that surfaces provide the
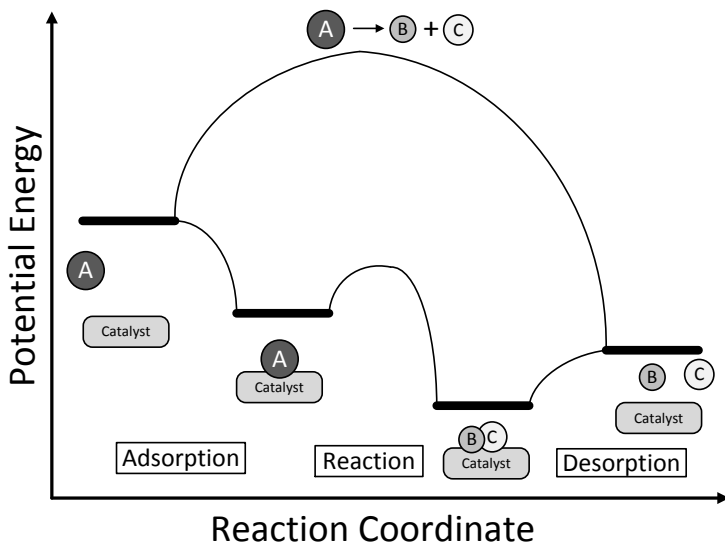
Figure 1.1: Potential energy diagram of uncatalyzed (top reaction path) and catalyzed (bottom reaction path) reactions. Adapted from [8]

reaction sites during catalysis. In 1895, Ostwald coined the first proper definition of a catalyst: *A catalyst is a substance that influences the rate of a chemical reaction, without itself appearing into the products, but does not influence the equilibrium.* As a substance that slows a reaction down is also a catalyst according to this definition, the contemporary definition is: *A catalyst is a substance that increases the rate at which a chemical reaction approaches equilibrium without becoming itself permanently involved.*

The role of a catalyst in a heterogeneous reaction is illustrated in figure 1.1. In this potential energy diagram, the higher the potential energy barrier is, the more energy it costs to overcome this barrier. The non-catalytic reaction of reactant A that decomposes to products B and C proceeds via a pathway involving a substantially higher barrier than the catalytic route. The initial step is the adsorption of the reactant on the catalyst. Because this is a spontaneous reaction, the potential energy decreases in this step with no activation barrier. The second step is the reaction of A to form B and C on the catalyst surface. This reaction typically requires an activation energy that is significantly lower than

for the uncatalyzed reaction. After the products B and C have been formed, they should desorb from the surface to close the catalytic cycle. Desorption is not a spontaneous process, it requires energy as well.

Nevertheless, the total amount of energy required to complete a reaction cycle through the catalytic route is less than in the non-catalytic case. Hence, the reaction is accelerated or can be carried out at a lower temperature. Another important issue is that the catalyst is re-obtained unaltered after each catalytic cycle. In theory this means that the catalyst can be reused endlessly.

A catalyst functions thus by providing an alternative reaction pathway. This alternative route is usually more complex, involving several elementary reaction steps, but in terms of energy more favorable.

Apart from being active, a successful catalyst should be selective and stable as well. A selective catalyst produces less undesired byproducts, requiring less separation, which is usually the most energy intensive part of a chemical process. Moreover, catalysts should be stable, both mechanically and chemically, to withstand deactivation over time.

Catalysts come in many forms and they can be atoms, molecules, solid surfaces and even enzymes. In general, one distinguishes three types of catalysts, namely heterogeneous-, homogeneous- and biocatalysts.

This thesis concerns heterogeneous catalysis, where the catalyst is in a different phase than the reactants. In 99% of all cases, heterogeneous catalysts are solids and catalyze reactions between liquid or gaseous species. Heterogeneous catalysts typically consist of an active metal dispersed in a support, to enhance the efficiency by improving the contact between the catalytic surface and the reactants. The support can be an impenetrable solid or a porous system. As sometimes expensive materials, such as precious transition metals, are used as the catalytically active species, metals are usually dispersed as nanometer-sized particles. The smaller the particles are, the more surface area is available for reaction. These different length scales of a typical heterogeneous catalyst are illustrated in Fig. 1.2.

Catalysts are classified 'homogeneous' if they are present in the same phase as the reactants. Homogeneous catalysts are known to be highly selective and active, but their drawback is the difficult separation of the
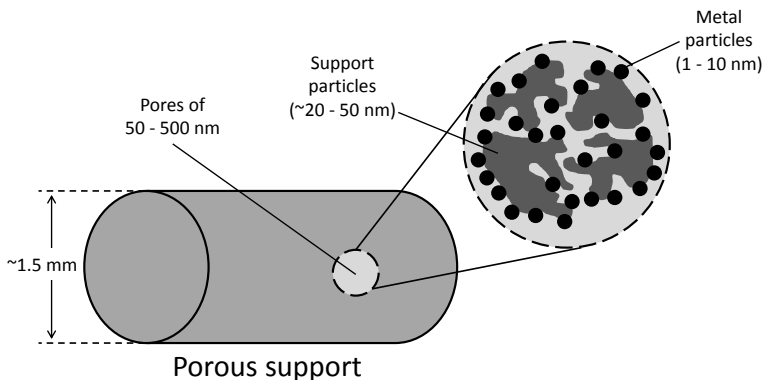
Figure 1.2: Different length scales in a heterogeneous catalyst

catalyst from the reaction mixture. As a result, homogeneous catalysts are less suitable for large, high-throughput chemical processes.

In biocatalysis, the catalyst consists of an enzyme that is built from various proteins. Enzymes are highly selective because of the key-lock (enzyme-substrate) principle. The importance of biocatalysis is increasing every year, especially in food, pharmaceutical and fine chemicals industry.

1.3 GASIFICATION

In the context of this thesis, gasification is the process of converting carbon feedstock to a combustible gas consisting mainly of carbon monoxide (CO) and hydrogen (H_2). Apart from these gases, methane (CH_4) and carbon dioxide (CO_2) are formed in minor amounts. Gasification is usually done by heating the feedstock to high temperatures in sub-stoichiometric amounts of oxygen or steam, to prevent total combustion. The process of gasification was first described by Jan Pieter Minckelers in 1784 [9], who discovered that if coal was heated in the absence of oxygen, a gas escaped which was lighter than air. This gas was flammable and could be used for lighting and cooking purposes, and this gas was later named town-gas.

Gasification of coal is done at high temperatures and pressures. These conditions are, however, less suitable for the gasification of biomass, since
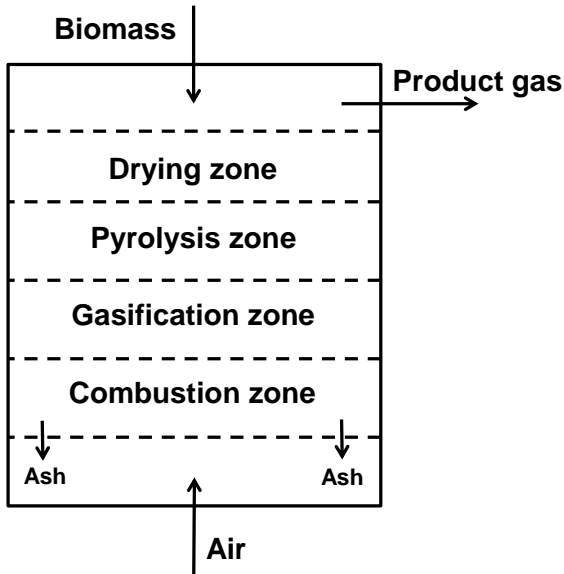
Figure 1.3: Schematic representation of a conventional biomass gasification reactor

it is difficult to feed biomass to a pressurized vessel. Therefore, biomass gasification is usually performed under atmospheric pressure in either fixed-bed or fluidized-bed gasification systems.

A schematic representation of a conventional fixed-bed gasifier is shown in figure 1.3. Biomass is fed from the top and air is blown in from the bottom. The biomass passes four different zones in the reactor, which are in 'fixed' positions. Because gasification in an endothermic process, it requires addition of energy in the form of heat. This heat is provided by partial combustion of the biomass at the bottom of the reactor. This results in a temperature gradient in the reactor, where the temperature is the highest in the combustion zone and decreases to about 200 °C in the drying zone. In this zone, the biomass is dried and thereafter converted to char and pyrolysis oil in the pyrolysis zone, where already some product gases are formed. The gasification process proceeds in the gasification zone and the unconverted biomass particles are combusted in the combustion zone. This results in the formation of ash residue, which falls through a grate in the bottom of reactor, where the air is blown in.

In fluidized-bed gasification, biomass particles are fluidized with a bed material by the gasifying agent. Compared to fixed-bed gasifiers, fluidized-bed gasifiers have several advantages [10, 11]. Since the density of biomass particles is low compared to coal, these particles have a poor fluidization quality. By adding an inert bed material, such as quartz sand, the fluidization quality increases and the mass and heat transfer characteristics improve. Fluidized-bed gasification can be further classified in bubbling fluidized-bed, dual fluidized-bed or circulating fluidized-bed gasifiers, of which the latter two are suitable for indirect biomass gasification, which is further explained in section 1.4.

One of the main problems associated with biomass gasification is the formation of tar. Tars are defined as the organics produced under thermal or partial-oxidation regimes (gasification) of any organic material and are generally assumed to be largely aromatic [12]. The formation of tars during biomass gasification decreases the total efficiency of the process. Moreover, tars can cause fouling of equipment and they can block downstream pipelines, preventing efficient work-up of the product gases. The tar formation during biomass gasification can to some extent be controlled by the process operating conditions and the use of additives [13].

Van Paasen and Kiel from the Energy Research Institute in The Netherlands (ECN) have identified five classes of tars, listed in table 1.1. This classification is based on the possible impact of the respective tars on the gasification process. Especially the heavy tars (Tar classes 1 and 5) can cause major problems, since they condense already at relatively high temperatures (500 °C). This means that all the downstream lines have to be heated to at least the tar dewpoint temperature to prevent this condensation.

Tar removal during biomass gasification can be achieved in several ways, which can be divided in primary and secondary methods, depending on the location where the tar is removed. If the tar is removed in the gasifier itself, it is called a primary method and if the tar is removed downstream of the gasifier, the methods are named secondary. Examples of secondary measures include scrubbing or gas cleaning of the product gas, and have extensively been reviewed by Anis and Zainal [15]. Pri-

Table 1.1: Classification of tar compounds [14]

Tar group	Name	Property	Tar compounds
Class 1	GC-undetectable (>6 rings)	Very heavy PAHs	Determined by subtracting the GC-detectable tar fraction from the total gravimetric tar
Class 2	Heterocyclic aromatics	Highly water soluble	Pyridine, phenol, cresol, quinoline
Class 3	Aromatics (1 ring)	Very low condensability and water solubility	Xylene, styrene, toluene
Class 4	Light PAHs (2–3 rings)	Condense at intermediate temperature and high concentration	Naphthalene, biphenyl, acenaphthylene, fluorene, phenanthrene, anthracene
Class 5	Heavy PAHs (4–6 rings)	Condense at high temperature and low concentration	Fluoranthene, pyrene, chrysene, benzo-fluoranthene, benzo-pyrene, perylene

PAHs: Polycyclic Aromatic Hydrocarbons

mary tar removal is achieved by using a tar conversion catalyst inside the gasification reactor. Several reviews of catalysis for biomass gasification have been published [16, 17] and give a good overview of the advantages and disadvantages of several catalytically active materials.

1.4 INDIRECT FLUIDIZED-BED GASIFICATION

Indirect fluidized-bed gasification is a special case of fluidized-bed gasification, where the gasification and the partial combustion take place in separate reactors, connected to each other. The major advantage of this process is that the product gas is almost free of N_2, which significantly increases the energy density of the product gas. Other advantages of this technique are more efficient conversion of the biomass fuel, no need for an costly air separation unit and that CO_2, from the partial combustion, is naturally separated from the product gases. The indirect fluidized-bed gasification is schematically illustrated in figure 1.4.

Biomass and steam, as the gasification agent, are fed to the gasification zone, where the biomass is converted to gaseous products, char and tar. The product gas is separated from the circulating bed material, which, together with the unconverted biomass, char and tar, is fed into a combustion reactor. In the combustion zone, air is introduced and
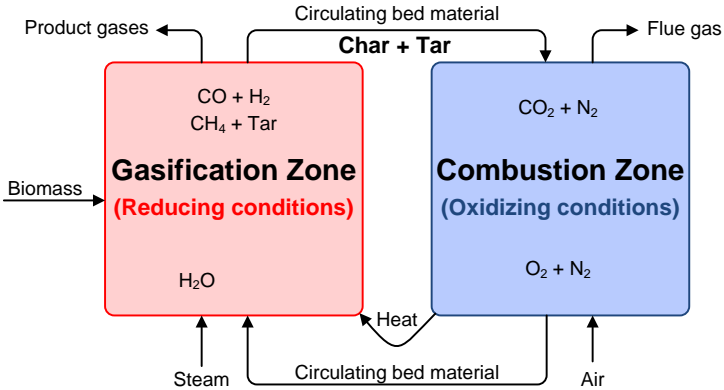
Figure 1.4: Schematic representation of the indirect gasification principle

the non-gaseous biomass residues, char and tar are combusted. This combustion or oxidation process heats the bed material, conventionally inert quartz sand. After the ash has been removed, the bed material is recirculated back to the gasification zone, where it provides the necessary heat for the endothermic gasification process.

Two examples of different types of indirect gasification systems that are employed in practice are the dual fluidized-bed gasification (DFB) system in Güssing, Austria and the MILENA process at ECN in Petten, which is a fast internally circulating fluidized-bed (FICFB) process.

The DFB system in Austria has been developed at the Vienna University of Technology and has been scaled up to a 8 MW combined heat and power plant, which has been running successfully since 2002 [18].

In the ECN MILENA gasification process, illustrated in figure 1.5, the gasification reactor is situated inside the combustion vessel. In this way, there is optimal heat transfer, both from the bed material and through the reactor wall. This concept was developed from a 30 kW lab-scale gasifier in 2004 to a 800 kW pilot plant in 2008 [19]. This system is designed with a riser as gasification zone, which has the advantage that the fluidization area is small, requiring less steam to fluidize the bed. The combustion zone is a bubbling fluidized-bed (BFB) with a longer residence time than
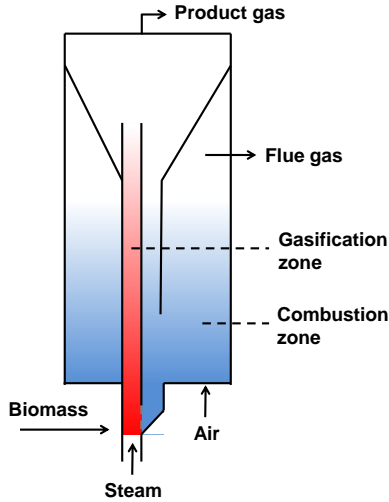
Figure 1.5: The ECN MILENA gasification process

in the gasification zone, allowing complete combustion of all the tar and char residues.

The overall ECN MILENA process is designed to produce Synthetic Natural Gas (SNG). Gasification of biomass is a promising way to produce this biogas [20]. In the Netherlands, around 45% of the energy that is used comes from natural gas [21], mostly for heating of buildings. Therefore, synthetic natural gas (SNG) can easily be introduced as a renewable fuel, since the present infrastructure for gas can be used.

The schematic flow sheet of the conversion of biomass to SNG is shown in figure 1.6. The gasification process is the first step, where the biomass is converted to mainly synthesis gas. Before the synthesis gas can be used to make SNG (CH_4), the product gas of the gasifier needs to be free of tars and other contaminants, such as ammonia and sulfur-containing compounds. These gases are poisons for the nickel in the
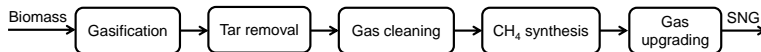
Figure 1.6: Biomass gasification as a first step to Bio-SNG

methanation catalysts. After the synthesis gas has been converted to CH_4, the gas needs to be upgraded, recycling the unconverted CO and H_2, and removing the CO_2 and H_2O, which are byproducts and then, the SNG is ready for injection in the existing grid.

1.5 CATALYTICALLY ACTIVE BED MATERIALS

Despite the advantages of indirect gasification, the formation of tars is still a problem. One of the primary methods for improving the gas quality is replacing the conventionally used inert quartz sand by a bed material, which is catalytically active towards tar conversion. Such a catalytically active bed material should increase the overall efficiency of the process by promoting char gasification, converting the unwanted tar molecules into the desired hydrogen and carbon monoxide, thereby changing the product gas composition [22]. Several catalytically active bed materials have been suggested [16, 23], amongst others: catalysts based on nickel, olivine and dolomite.

Because of the fast deactivation of Ni-based catalysts in the gasifier and the low costs of the natural minerals dolomite and olivine, these minerals are frequently used as primary catalysts during indirect biomass gasification [22].

Dolomite is an magnesium ore with as general formula $MgCO_3$-$CaCO_3$. To improve its mechanical stability, dolomite is usually calcined prior to use as a catalyst in circulating fluidized-bed reactors [23]. During calcination, it decomposes into MgO-CaO by releasing CO_2. The calcined dolomite can then be used in the gasification reactor as a primary catalyst without further modification.

Olivine is an iron-magnesium silicate and is one of the most abundant minerals found in the earth's mantle [24], and was also found to exist in meteorites [25] and on Mars [26]. The molecular formula of olivine is generally written as $(Mg,Fe)_2SiO_4$ and the Mg_2SiO_4 content is usually around 90%. Olivines have a high melting point of around 1600 °C and a hardness of 6.5 - 7 on Mohs scale, which is comparable to quartz, but much higher than dolomite, which has a hardness of 3.5 - 4 [27].

The activity and reactivity of dolomite and olivine in biomass gasification have been the subject of many studies. The combination of magnesium-oxide and calcium-oxide, as in calcined dolomite, has shown a better activity towards tar reduction compared to its constituents separately [28].

Fluidized-bed gasification of biomass with dolomite or olivine as bed material results in a lower tar concentration in the product gas, compared to sand [29], and dolomite is slightly more active than olivine. Koppatz et al. [30] showed that if quartz sand was replaced by olivine as bed material in a 100 kW DFB reactor, the tar content of the product gas decreased significantly between 35 and 60% . The performance of olivine as primary catalyst is dependent on the pre-treatment: oxidized olivine showed a lower tar conversion than dolomite [31], whereas olivine in the reduced state showed a higher tar conversion for fluidized-bed pyrolytic gasification of cellulose.

The performance of dolomite and olivine as bed materials in fluidized-bed gasification was compared by Corella et al. [32]. Although dolomite was shown to be 1.4 times more active than olivine, it generated a lot of particulates, due to attrition. This makes dolomite less suitable for use as bed material in indirect biomass gasification, since a lot of particles will be blown out the gasifier with the product gas and cause problems in filters, due to the small particle size.

Because of the advantages and disadvantages mentioned here, both the DFB gasifier in Güssing and the ECN MILENA gasifier use olivine as the active bed material [19].

1.6 OLIVINE

The first report of the use of olivine as a bed material for biomass gasification was published in 2000 by Rapagna and coworkers [33]. The researchers found a good performance of olivine towards tar reduction with a negligible production of fines in the fluidized-bed, which is a major problem with the use of dolomite.

Three olivines from different origins were compared by Kuhn et al. for steam reforming of model tar compounds and the most active catalyst

was olivine, originating from Austria and mined by Magnolithe GmbH [34]. Devi et al. reported that pre-treatment of olivine at high temperatures could improve the catalytic performance as bed material [35]. This increased activity was explained by the increased iron concentration at the surface of the catalyst [36].

Several other researchers have identified iron as the catalytically active component in olivine, when used as a tar decomposition catalyst in biomass gasification. When olivine was used as a support for a 10 wt.% Fe catalyst in a DFB reactor, it performed better in tar reforming compared to bare olivine [37, 38]. Addition of iron to olivine thus helps the tar destruction. Moreover, olivine and Fe/olivine can act as oxygen carriers, transporting oxygen from the combustion zone to the gasification zone.

The activity of iron towards tar reduction during biomass gasification was confirmed by Nordgreen and coworkers, who identified metallic iron as a good tar depletion catalyst [39]. Iron oxide, however, did not demonstrate any catalytic activity in converting tars during gasification of biomass. In another study, they found that the activity of iron was dependent on both the temperature of the bed and the oxygen potential of the surrounding gas environment [40].

The thermodynamically most stable phases in olivine change with changing partial oxygen pressures. This dynamic behavior of olivine was already reported in 1974 by Nitsan, who calculated the so-called 'stability field of olivine' [41], i.e. the temperature and gas conditions under which olivine is the thermodynamically stable phase. These calculations showed that Fe_3O_4, SiO_2, pyroxene ($(Mg,Fe)SiO_3$) and olivine are the stable phases after treatment in oxidizing environments (oxygen fugacity of $> 10^{-6}$ atm). The same phases are expected under reducing conditions (oxygen fugacity $< 10^{-12}$ atm), with the exception that metallic Fe is expected instead of Fe_3O_4.

Swierczynski et al. investigated the state of iron during oxidation and reduction of olivine under the catalyst working conditions [42]. In oxidizing environments, iron was extracted from the olivine matrix and formed reducible iron oxide phases. The formation of these oxides was dependent on the oxidation temperature and limited by the thermodynamics of the system. Upon reduction, part of the oxide phases reduced to metallic

iron, whereas another part of the free oxide phases was reintegrated back into the olivine structure.

1.7   THE SCOPE OF THIS THESIS

Its dynamic properties greatly influence the performance of olivine as a biomass gasification catalyst. In different gas environments, different phases will form, due to the changing thermodynamic stability.

In view of the catalytic function of olivine, iron is the most interesting component, because it is the active component in the tar reduction. Iron can be extracted from the olivine phase upon oxidation [42], and will migrate to the surface of the olivine particles [36]. These free iron phases can subsequently be reduced by gases, which are typically present in the gasification zone. If iron changes oxidation state, the catalytic activity of olivine will change as well.

Moreover, alternating oxidation and reduction of olivine in the different zones of the indirect gasifier implies that olivine transports oxygen from the combustion zone to the gasification zone.

However, the exact catalytic function of olivine is not yet fully understood. The central questions of this research are thus: How does olivine change during exposure to the different conditions, representative for gas environments present in indirect biomass gasification reactors and how does this behavior relate to the performance of olivine as a biomass gasification catalyst?

The work described in this thesis is divided into seven chapters:

- Chapter 2 describes shortly the experimental techniques that were used during this research.

- The dynamic behavior of olivine under realistic model conditions is presented in chapter 3.

- Chapter 4 describes the role of iron in the chemical looping process. Oxygen transport is determined under realistic conditions, since exact figures or relations to quantify the amount of this transported oxygen were unknown.

- During long term, continuous use as bed material in biomass gasifi-
  cation, olivine gets coated by materials stemming from the biomass
  ash. Chapter 5 describes the nature of this bed material coating and
  the influence of the coating on the reactivity is determined.

- Since natural olivine is, as most minerals, an inhomogeneous mate-
  rial, the composition and catalytic behavior vary with the different
  origins [34]. Therefore, olivine is not suitable to study the iron - sil-
  ica interaction in detail. Chapter 6 describes the first steps towards
  the development and characterization of an iron on silica model
  catalyst. This well-defined catalyst allows detailed study of the iron
  particles in relation to the silica support.

- In the conclusion and outlook (chapter 7), the results of all chapters
  will be discussed in relation to the impact on the indirect biomass
  gasification process.

REFERENCES

[1] BP Statistical Review of World Energy 2014 (http://www.bp.com/en/global/corporate/about-bp/energy-economics/statistical-review-of-world-energy.html).

[2] BP Energy Outlook 2035 (2014) (http://www.bp.com/en/global/corporate/about-bp/energy-economics/energy-outlook.html).

[3] Shell Energy Scenarios to 2050 (2008) (http://www.shell.com/global/future-energy/scenarios/2050.html).

[4] A. Ajanovic, Energy 36 (2011) 2070–2076.

[5] P. McKendry, Bioresource Technology 83 (2002) 47–54.

[6] Transparency Market Research, Global Refinery Catalyst Market (2013)

[7] ACS Catalysis (http://catl.sites.acs.org/)

[8] I. Chorkendorff and J. W. Niemantsverdriet, *Concepts of Modern Catalysis and Kinetics*, Wiley-VCH, Weinheim, 2003.

[9] J. P. Minckelers, *Mémoire sur l'air inflammable tiré de différentes substances*, 1784.

[10] J. Pecho, T. J. Schildhauer, M. Sturzenegger, S. Biollaz and A. Wokaun, Chemical Engineering Science 63 (2008) 2465–2476.

[11] K. Zhang, J. Chang, Y. Guan, H. Chen, Y. Yang and J. Jiang, Renewable Energy 49 (2013) 175–184.

[12] T. A. Milne and R. J. Evans, National Renewable Energy Laboratory, NREL/TP-570-25357 (1998) .

[13] T. Damartzis and A. Zabaniotou, Renewable and Sustainable Energy Reviews 15 (2011) 366–378.

[14] S. V. B. van Paasen and J. H. A. Kiel, ECN report ECN-C-04-013 (2004) .

[15] S. Anis and Z. A. Zainal, Renewable and Sustainable Energy Reviews 15 (2011) 2355–2377.

[16] D. Sutton, B. Kelleher and J. R. H. Ross, Fuel Processing Technology 73 (2001) 155–173.

[17] D. A. Bulushev and J. R. H. Ross, Catalysis Today 171 (2011) 1–13.

[18] H. Hofbauer, R. Rauch, K. Bosch, R. Koch and C. Aichernig, *Biomass CHP plant Güssing - A success story*, Pyrolysis and Gasification of Biomass and Waste, A. V. Bridgewater (Ed.), CPL Press, Newbury, Berks, UK, 2003.

[19] C. M. van der Meijden, *Development of the MILENA gasification technology for the production of Bio-SNG*, PhD Thesis, Eindhoven University of Technology, 2010.

[20] J. Kopyscinski, T. J. Schildhauer and S. M. A. Biollaz, Fuel 89 (2010) 1763–1783.

[21] Energiebalans Centraal Bureau voor de Statistiek (juni 2014)

[22] H. de Lasa, E. Salaices, J. Mazumder and R. Lucky, Chemical Reviews 111 (2011) 5404–5433.

[23] Y. Shen and K. Yoshikawa, Renewable and Sustainable Energy Reviews 21 (2013) 371–392.

[24] P. Cordier, S. Demouchy, B. Beausir, V. Taupin, F. Barou and C. Fressengeas, Nature 507 (2014) 51–56.

[25] M. I. Petaev and A. J. Brearley, Science 266 (1994) 1545–1547.

[26] J. F. Mustard, F. Poulet, A. Gendrin, J.-P. Bibring, Y. Langevin, B. Gondet, N. Mangold, G. Bellucci and F. Altieri, Science 307 (2005) 1594–1597.

[27] www.mindat.com

[28] J. Delgado, M. P. Aznar and J. Corella, Industrial & Engineering Chemistry Research 36 (1997) 1535–1543.

[29] F. Miccio, B. Piriou, G. Ruoppolo and R. Chirone, Chemical Engineering Journal 154 (2009) 369–374.

[30] S. Koppatz, C. Pfeifer and H. Hofbauer, Chemical Engineering Journal 175 (2011) 468–483.

[31] C. Vilela, *Primary Methods in Biomass Gasification for Gas Conditioning and Cleaning*, PhD Thesis, Eindhoven University of Technology, 2012.

[32] J. Corella, J. M. Toledo and R. Padilla, Energy & Fuels 18 (2004) 713–720.

[33] S. Rapagna, N. Jand, A. Kiennemann and P. U. Foscolo, Biomass and Bioenergy 19 (2000) 187–197.

[34] J. N. Kuhn, Z. Zhao, L. G. Felix, R. B. Slimane, C. W. Choi and U. S. Ozkan, Applied Catalysis B: Environmental 81 (2008) 14–26.

[35] L. Devi, K. J. Ptasinski and F. J. J. G. Janssen, Fuel Processing Technology 86 (2005) 707 – 730.

[36] L. Devi, M. Craje, P. Thüne, K. J. Ptasinski and F. J. J. G. Janssen, Applied Catalysis A: General 294 (2005) 68–79.

[37] M. Virginie, J. Adanez, C. Courson, L. F. de Diego, F. Garcia-Labiano, D. Niznansky, A. Kiennemann, P. Gayan and A. Abad, Applied Catalysis B: Environmental 121-122 (2012) 214–222.

[38] S. Rapagna , M. Virginie, K. Gallucci, C. Courson, M. D. Marcello, A. Kiennemann and P. U. Foscolo, Catalysis Today 176 (2011) 163–168.

[39] T. Nordgreen, T. Liliedahl and K. Sjöström, Fuel 85 (2006) 689–694.

[40] T. Nordgreen, V. Nemanova, K. Engvall and K. Sjöström, Fuel 95 (2012) 71–78.

[41] U. Nitsan, J. Geophys. Res. 79 (1974) 706–711.

[42] D. Swierczynski, C. Courson, L. Bedel, A. Kiennemann and S. Vilminot, Chemistry of Materials 18 (2006) 897–905.

2

Experimental Techniques

Since the performance of catalysts is determined by their structure on different levels, catalyst characterization is of vital importance. Characterization can provide insight in the exact properties of an active site or surface and enables researchers to distinguish good and poor catalysts.

The aim of catalyst characterization is to determine the composition and structure of the catalytic surface, ideally under reaction conditions and in atomic detail [1]. There are many different techniques and different kinds of information carriers are used, for example: photons, electrons, ions or electromagnetic fields.

Each technique has its own specific strength and weakness. Some characterization methods use e.g. electrons, which have a short mean free path, so these measurements must be done in vacuum. On the other hand, if one wants to study nanometer sized metal particles with electron microscopy, these particles must be accessible to the the electron beam. Particles inside a large porous support are thus difficult to study with microscopy techniques.

Such limitations are often referred to as the pressure gap and materials gap in catalyst characterization, since they require that the catalyst is studied under conditions that are vastly different from those applied in a catalytic process. However, some techniques allow to study the catalyst under its real working condition, at high temperature and pressures. These techniques are classified as in-situ or operando.

This chapter describes the characterization techniques that have been used to carry out the research described in this thesis.

2.1   X-RAY DIFFRACTION

X-Ray Diffraction (XRD) is the most frequently used technique in catalyst characterization [1, 2]. X-rays have the advantage that they are energetic enough to penetrate solids and the diffracted X-rays can then give information about the internal structure of the material.

The schematic representation of XRD is shown in figure 2.1. The X-ray source emits photons, which are scattered elastically by atoms in a lattice. When the lattice is ordered, as in a crystal or crystallite phase inside a material, the scattered X-rays can interfere constructively. A requirement for the constructive interference is that the difference in distance that the radiation travels (dashed part in the insert in Fig. 2.1) must be an integer times its wavelength. If this is the case, the conditions for interference are fulfilled, and the diffracted X-rays are in phase as well.

The intensity of these diffracted X-rays is recorded by a detector, and the 2θ angle is determined as well. The distance d between two lattice planes can be calculated from the diffraction peaks in the XRD diffractogram according to Bragg's law:

$$n \cdot \lambda = 2d \cdot \sin(\theta) \quad \text{with } n = 1, 2, ... \tag{2.1}$$

In this relationship, λ is the wavelength of the X-rays, θ is the angle of reflection, relative to the surface normal and n is an integer called the order of the reflection. The wavelength of the X-rays depends on the type of target material used inside the cathode X-ray tube. The most common X-ray source used for XRD is a copper target, which emits Cu Kα X-rays with an energy of 8.04 keV and a wavelength of 0.154 nm.

The set of diffraction peaks and corresponding d-spacings calculated from these diffraction peaks are characteristic for a certain compound and the crystallographic phases present in this compound, and extensively documented in databases, such as the Powder Diffraction Files (PDF) from the International Centre for Diffraction Data (ICDD) [3].

Next to identifying the phases present in a compound or catalyst, XRD can also provide information about the size of the crystals in the sample. The theoretically very sharp diffraction lines broaden in XRD
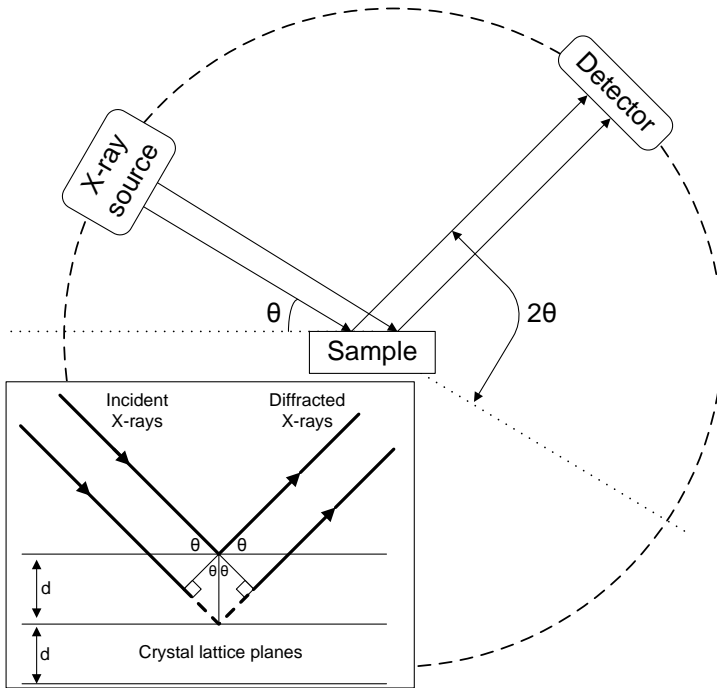
Figure 2.1: Schematic representation of XRD, the insert shows constructive interference

due to inhomogeneous strain and lattice imperfections. The Scherrer equation relates the average crystallite particle size L to the width of a corresponding diffraction line:

$$L = \frac{K \cdot \lambda}{B \cdot \cos(\theta)} \tag{2.2}$$

In this formula, K is the Scherrer constant (usually taken as unity, when exact particle shape is unknown), λ is the wavelength of the incident X-rays, B is the full width at half maximum (FWHM) of the reflection and θ is the angle of reflection in radians.

In this work, XRD is used to determine which mineral phases are present in olivine and how these phases change upon different gas treatments.

2.2   X-RAY PHOTOELECTRON SPECTROSCOPY

X-ray Photoelectron Spectroscopy (XPS) is a spectroscopic characterization technique that makes use of the photoelectric effect to determine the chemical composition of materials. The photoelectric effect was first discovered by Hertz in the 1880s, but it was Einstein, who described the effect in detail in 1905 using his theory on quantum mechanics [4].

XPS was first named "Electron Spectroscopy for Chemical Analysis" (ESCA) and was developed from the late 1960s on by professor Kai Siegbahn and coworkers at the Uppsala University in Sweden. Siegbahn was awarded the Nobel Prize in Physics in 1981 for his contribution to the development of high-resolution electron spectroscopy.

The basic principle of XPS is illustrated in Fig. 2.2. A sample is irradiated with X-rays and photoelectrons are ejected as a result of this irradiation, as described by the photoelectric effect. The electrons leaving the sample are collected by a detector and the signal is measured as counts per second (cps). Moreover, the detector measures the kinetic energy of the ejected photoelectrons as well, so the energy balance for the photoemission process is as follows:

$$h\nu = E_b + \varphi + E_k \tag{2.3}$$

In which h is Plancks constant, ν is the frequency of the incident X-rays ($h\nu$ is the photon energy), E_b is the binding energy of the photoelectrons, φ is the work function of the spectrometer (difference between Fermi level and vacuum level) and E_k is the kinetic energy of the photoelectrons. In XPS, the X-ray source emits photons with a known, constant frequency, so $h\nu$ is a known constant as well as the work function φ. When the
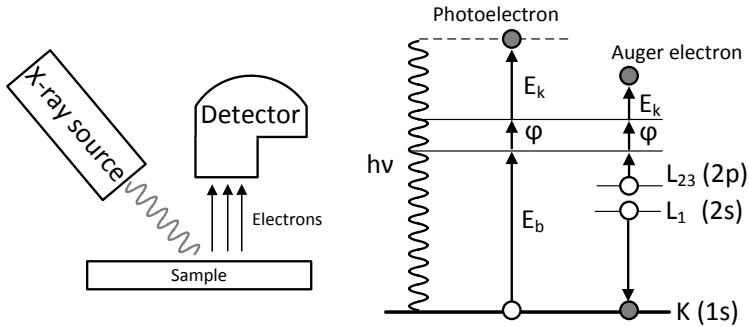
Figure 2.2: Schematic principle of XPS

kinetic energy is measured, the binding energy can be calculated by rewriting Eq. 2.3 to:

$$E_b = h\nu - \varphi - E_k \qquad (2.4)$$

This binding energy depends primarily on the type of element, its oxidation state and the chemical environment of the specific atoms. For example, the Fe 2p peak appears at a lower binding energy for metallic iron than for Fe^{3+} in Fe_2O_3. The latter has a 4 eV higher binding energy. This is because the 26 electrons in the metallic iron feel a lower attractive force to the nucleus, which has a charge of 26+, than the 23 electrons of Fe_2O_3. Moreover, electronegative ligands can change the chemical environment of atoms. By withdrawing electrons from the atom, they decrease the local electron density, thereby increasing the binding energy these electrons will experience. Neighboring ions give their contributions via the Coulomb interaction, which reduces the effect of the atoms overcharge. Hence, peaks from atoms with a more electronegative environment (e.g. the C 1s electrons of C=O) will appear at a higher binding energy than peaks from atoms with a neutral environment (e.g. C–C).

Apart from photoelectron peaks, an XPS spectrum usually shows peaks from Auger electrons as well. In the Auger process, the electron hole left behind in a lower shell by an ejected photoelectron is filled by an electron

from a higher energy level. The energy associated with in this process can be released either as a photon or by ejecting a second electron. Since the energy levels for each element are fixed, the Auger electrons reach the detector with a kinetic energy that is independent of the X-ray source energy. Therefore, depending on the photon energy of the X-ray source, according to eq. 2.4, these Auger peaks will appear at different binding energies when different sources are used.

By convention, the x-axis in XPS spectra is plotted from high to low binding energy, since the kinetic energy is measured and E_{kin} is inversely proportional to the binding energy. Each element has a series of photoelectron peaks, corresponding to each core level electron with a binding energy that is lower than the photon energy of the X-rays.

XPS is a surface sensitive technique, since the inelastic mean free path of electrons inside a material is on the order of a few to 5 nm (limited by scattering). In other words, electrons that are liberated deep inside the material do not have sufficient energy to leave the sample, since they collide with the lattice atoms and lose part of, or all their initial kinetic energy. Therefore, only electrons from atoms close to the surface of the material are able to reach the detector. This is also the main reason that XPS is generally carried out in ultra-high vacuum, with pressures in the measurement chamber in the 10^{-9} mbar range.

A typical XPS spectrum for olivine is shown in Fig. 2.3. The intensity of the detected photoelectrons is plotted as (electron) counts per second as a function of their binding energy.

In this spectrum, all elements present at the surface of the sample can be identified using their photoelectron peaks, corresponding to each core level electron with a binding energy that is lower than the photon energy of the X-rays. These peaks all appear at a characteristic binding energy and these energies are extensively documented for most elements [5]. Apart from the peaks that originate from the elements present in olivine ($(Mg,Fe)_2SiO_4$), a peak originating from carbon can be observed as well. A carbon peak is usually observed in XPS experiments for samples that have been exposed to air, and originates from the deposition of adventitious carbon species from the atmosphere onto the sample.
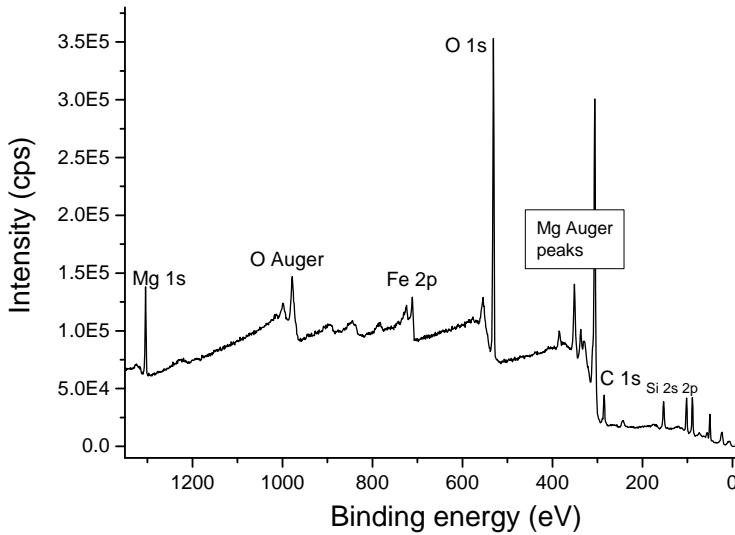
Figure 2.3: XPS wide scan of an olivine sample

The area of the peaks in the spectrum is proportional to the relative atomic concentration of the respective element at the surface. However, each peak area needs to be corrected for the specific sensitivity. This so-called Relative Sensitivity Factor (RSF) is dependent on the cross-section of the respective electron subshell [6, 7]. If all the peaks are divided by their RSFs, it is straightforward to obtain the quantitative surface composition of the sample. Since XPS is surface sensitive, surface species tend to be over estimated.

In addition to quantitative information, XPS can also be used to provide qualitative information about the surface elements. To obtain this information, usually a high resolution region scan is recorded from a specific photoelectron peak. This detailed spectrum can provide information on the relative abundance of atoms in a certain oxidation state. For instance, the Fe 2p region can provide information on the relative concentration of different oxidation states of iron surface species. The Fe 2p peak for metallic iron has a significantly lower binding energy (707 eV) compared to the Fe 2p peak originating from Fe_2O_3, which lies around 711 eV. The ratio of the areas of both peaks determines the relative

concentration of each iron species and can thus be used to quantify the degree of reduction of the iron at the surface of the sample.

2.2.1 *XPS Depth Profiling*

The surface sensitivity of XPS is often an advantage in catalysis research, since catalytic processes take place at the surface of the active species. Although the overall bulk concentration of these species is typically low, their relative surface concentration is high. Therefore, XPS provides information about the active part of catalyst particles, specifically. In some cases, however, information from material deeper inside the sample is desired. This can be achieved by XPS in combination with depth profiling.
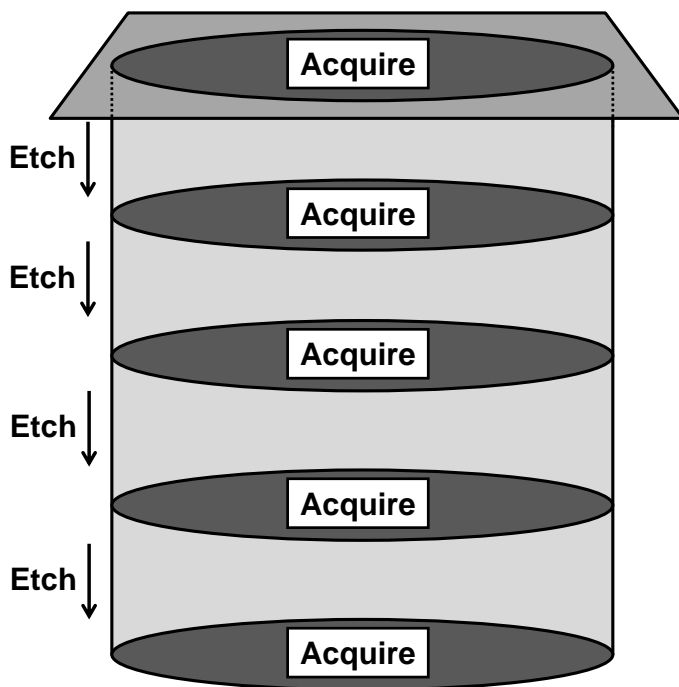
Figure 2.4: XPS depth profiling: Alternating measurements and removal of material

The principle of XPS depth profiling is shown in Fig. 2.4. Basically, it involves analysis of the surface, followed by removal of a layer of the material at the surface. If this process is repeated for several cycles, information about the material is gathered as a function of depth, i.e. distance from the surface of the original sample in the direction of the surface normal.

The removal of material is usually achieved by bombarding the sample with an energetic ion-beam, most frequently Ar^+. This process is called sputtering or etching. After each ion gun etch period, a new surface is exposed and an XPS spectrum is acquired for analysis. The amount of material removed in each sputter step, and hence, the precise sample depth at which each XPS spectrum is recorded depends on the time the ion gun is used per step and its sputter rate.

The sputter rate is influenced by the ion gun settings and the type of sample material that is etched. For the ion gun, the type of ions used, their respective energy and angle to the sample determine the sputter rate. For the sample material, the sputter rate depends on the sputter yield for the different elements and the surface morphology. If the energy of the incident ions is not transferred equally between the atoms in the sample, preferential sputtering may occur. This means that atoms from one species, for example oxygen, are removed more efficiently than atoms of another element. Apart from being removed by the high energy ions, atoms at the outer surface can also be driven inside the surface layer of the sample. This ion-gun induced mixing of the surface atoms is called knock-on mixing or forward sputtering.

In XPS, depth profiles are usually specified by the etching time, because in most cases, it is difficult to convert this etch time to an absolute length depth scale. Therefore, the sputter rates of XPS machines are frequently related to an international standard, which currently is a Ta_2O_5/Ta foil with an accurately determined oxide thickness [8].
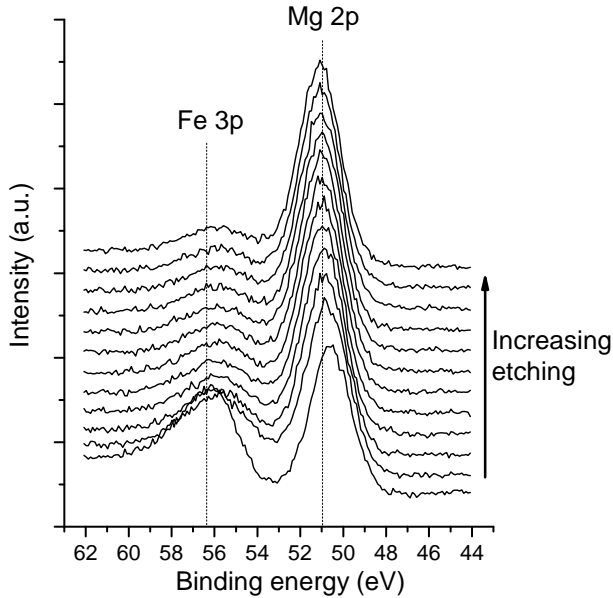
Figure 2.5: Close-up of the Fe 3p - Mg 2p region during a XPS depth profile experiment of olivine, showing the presence of iron in the outer region of the sample

Figure 2.5 shows an example of XPS depth profiling from an olivine sample. A series of detailed Fe 3p - Mg 2p spectra are shown, where the bottom spectrum is recorded from the outer surface of the particle and each subsequent spectrum is recorded after a subsequent ion beam etch. The area under the Fe 3p peak decreases with increasing etching, while the area of the Mg 2p signal slightly increases, indicating that iron is not homogeneously distributed in the sample. The iron concentration at the outer surface is higher compared to deeper inside the sample.

Although depth profiles generally yield good quantitative information, one should be cautious when deriving qualitative information from depth profiles. Bombarding the sample with high energy ions can induce chemical transformations. If, for instance, oxygen is removed at a higher rate compared to the metal in a metal oxide, the material deeper inside the sample may show a lower oxidation state compared to the surface

species. This sputtering induced reduction can be an effect of the etching rather than a real feature in the sample.

2.3 MÖSSBAUER SPECTROSCOPY

Mössbauer spectroscopy is based on the Mössbauer effect, which was discovered by Rudolf Mössbauer in 1958. For this discovery, he was awarded the Nobel Prize in physics in 1961 "*for his researches concerning the resonance absorption of gamma radiation and his discovery in this connection of the effect which bears his name*" [9]. The Mössbauer effect involves the recoil-free emission and absorption of gamma rays by nuclei in a solid and is illustrated in figure 2.6.

When atoms are free to move, i.e. in a gas, a decaying excited nucleus cannot emit photons of sufficient energy to excite a similar nucleus to the same excited level, because recoil energy is involved. The phenomenon of recoil energy is best known if one fires a gun or if one wants to jump from a floating boat to the shore.

The energy of photons emitted by nuclear decay of the source-nucleus is the difference of the energy levels E_0 minus the recoil energy E_R. The energy required to excite another nucleus in the ground state, which experiences the recoil energy as well, to the excited state E_0, equals E_0 +
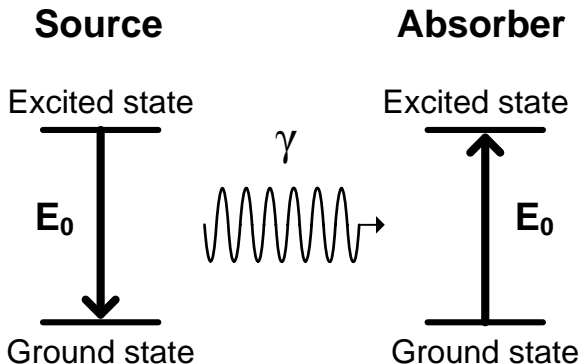
Figure 2.6: The Mössbauer effect: Recoil-free emission and absorption of gamma rays
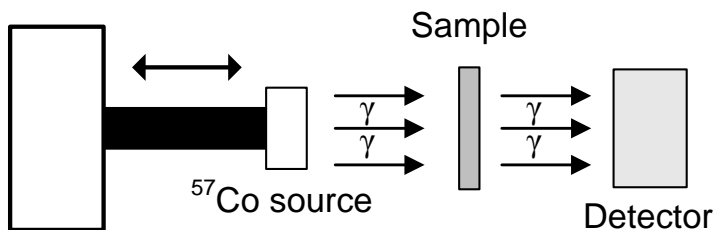
Figure 2.7: Schematic representation of a Mössbauer spectroscopy set-up

E_R. In other words, emission and absorption of the same gamma-ray by identical free nuclei is not possible.

However, if the atomic nuclei are bound together in a solid lattice, these nuclei are not able to recoil freely. The crystal lattice will take up this recoil energy as lattice vibrations. These lattice vibrations are quantized according to quantum mechanical rules, and a fraction of the emission and absorption events will be recoil-free, which is shown schematically in figure 2.6. Mössbauer spectroscopy makes uses of this effect, where excited source nuclei emit gamma rays that are resonantly absorbed by nuclei in a sample which contains the same isotopes.

Not all elements in the periodic table have isotopes that are Mössbauer active, and the most relevant isotopes for catalysis research are ^{57}Fe and ^{57}Co, which account for >90% of all Mössbauer related catalysis publications [10].

Figure 2.7 shows a schematic representation of a Mössbauer spectroscopy set-up, operated in transmission mode, which is frequently used to study iron containing materials. The solid powder sample is exposed to gamma radiation, produced by the radioactive cobalt source. The detector measures the intensity of the radiation that is transmitted through the sample.

The nuclei of the different iron compounds (metallic, oxides, etc.) all have slightly different energy levels. This means that if the atoms in the sample are present in a different chemical environment than the atoms in the source, the radiation will be transmitted to the detector, because the energy levels in the sample are slightly different from the emitted radiation. However, for atoms in the source and in the sample that are

in the exact same chemical environment, the Mössbauer effect will be observed and some of the radiation will be absorbed by the sample and the detector will detect less transmittance.

To facilitate identification of different energy levels, the energy of the source needs to be varied. In practice, this is done by using the Doppler effect: the source is accelerated towards and from sample by a linear motor. Hereby, the Doppler effect produces the shift in photon energy, required to observe all transitions of the compounds of interest. Consequently, the transmission is usually plotted as a function of the velocity of the source. For iron catalysts, this velocity usually ranges from −12 to +12 mm/s.

In Mössbauer spectra, generally three types of interactions are observed; isomer shift, quadrupole splitting and magnetic splitting. Usually, all three effects are observed in one single spectrum.

Isomer shift derives from an electric monopole interaction and is caused by the Coulomb interaction between the nucleus and the surrounding s-electrons. Because the electron density is different for a nucleus in the ground-state than in the excited-state, this effect causes the whole spectrum to shift to higher or lower energies. The isomer shift yields valuable information on the ionization state of the iron in the sample.

The electric quadrupole splitting is a result of the interaction between the electric field gradient and the electric quadrupole moment of the nucleus. An Fe atom in the excited state has a non-spherical charge distribution around the nucleus, which causes an electric quadruple moment. This results in two peaks in the Mössbauer spectrum. The quadrupole splitting, the difference in energy of the two peaks gives an indication of the magnitude of the electric gradient at the nucleus. This splitting gives information on the symmetry in the sample. For example, iron in a cubic (6-fold) environment has a Quadruple Splitting (QS) of zero, whereas iron in a hexagonal (cylindrical) environment can be strongly asymmetric, which results in a large QS.

Finally, the magnetic hyperfine splitting is caused by the interaction of the nucleus with the surrounding magnetic field and is often referred to as the nuclear Zeeman effect. When the nuclear magnetic dipole moment interacts with the magnetic field around the nucleus, the excited energy

levels are split in four levels. The ground state is split in two levels, so this gives eight theoretical transitions. However, 2 transitions are forbidden, resulting in six peaks in the transmission spectrum. Nuclear magnetic fields in iron containing materials can be as high as 50 T and can help in identifying the exact types of iron-oxide phases inside for instance minerals.

2.4 THERMOGRAVIMETRIC ANALYSIS

Thermogravimetric analysis (TGA) is a commonly used technique for studying reactive gas-solid systems. Basically, in TGA the mass of a sample is measured as a function of time. During the measurement time, the temperature is increased or decreased and the sample can be exposed to a reactive gas flow. TGA data is usually reported as mass or mass change as a function of the temperature.

A set-up for TGA typically consists of a very accurate balance and a furnace to heat the sample material. A computer controls the furnace and records the exact mass of the sample as a function of the sample temperature. A gas flow is used to control the sample environment during measurement. This gas flow can be either inert or contain species that interact with the sample to study reactions.

TGA is frequently used to determine certain properties of polymers, such as absorbed moisture content, degradation temperature or the amount of organic and inorganic components. For catalysis research, TGA systems can be equipped with a mass spectrometer and the mass loss during heating can be related to the respective compounds that evolve from the sample upon heating. For example, an used catalyst can be heated and exposed to oxygen. The temperatures at which CO and CO_2 come of, can then be related to the types of carbon that were deposited on the catalyst during use.

2.5 CONCLUSION

In the study described in this thesis, XRD was used for bulk characterization. XRD provided useful information on the changes in bulk

composition of olivine upon different treatments. These changes did not only concern the iron, but magnesium species as well. Moreover, carbon depositions could be observed after some treatments.

XPS was the most intensively used characterization technique for this research. It was obviously used for surface characterization. Depth profiling provided more insight in the iron surface and sub-surface enrichment and formation of a coating layer during industrial use.

Mössbauer spectroscopy yielded valuable information on the iron species in olivine, since it allows in-situ characterization and only focuses on the iron in olivine.

To determine the capabilities of olivine to transport oxygen, TGA was used in alternating oxidizing and reducing environments to measure the mass change of the sample during these treatments. The mass change could then be related to the amount of oxygen that can be transported under industrial conditions.

X-ray Absorbtion Spectroscopy (XAS) was only used for a minor part to obtain information on the relative distribution of the iron species, so this technique is not described in this chapter.

Electron microscopy, specifically transmission (TEM) and scanning (SEM), was used to obtain visual information on the olivines surface and to characterize the model catalysts. Since no detailed information was obtained with these techniques, they are not mentioned in this chapter.

REFERENCES

[1] J. W. Niemantsverdriet, *Spectroscopy in Catalysis*, Wiley-VCH, Weinheim, 2007.

[2] J. P. Dormans, R. J. Lancee and J. W. Niemantsverdriet, *Statistics on Catalyst Characterization*, Internal Report, Eindhoven University of Technology, 2006.

[3] www.icdd.com

[4] A. Einstein, Annalen der Physik 322 (1905) 132–148.

[5] J. F. Moulder, W. F. Stickle, P. E. Sobol and K. D. Bomben, *Handbook of X-ray Photoelectron Spectroscopy*, Perkin-Elmer Corporation, 1992.

[6] J. H. Scofield, Journal of Electron Spectroscopy and Related Phenomena 8 (1976) 129–137.

[7] C. D. Wagner, Journal of Electron Spectroscopy and Related Phenomena 32 (1983) 99–102.

[8] J. F. Watts and J. Wolstenholme, *An Introduction to Surface Analysis by XPS and AES*, John Wiley & Sons Ltd., 2003.

[9] www.nobelprize.org/nobel_prizes/physics/laureates/1961

[10] J.-M. M. Millet, Advances in Catalysis 51 (2007) 309–250.

3

Dynamic Behavior of Olivine under Model Conditions

ABSTRACT

This chapter describes the stability of Austrian olivine under model conditions, resembling those in a gasifier. Powder samples were heated to 750 °C and exposed to oxidizing (O_2, H_2O, CO_2) or reducing gases (CO, H_2) or mixtures thereof. Significant changes in phase composition of the material, depending on the gas composition and the duration of the treatments, were found using XPS, XRD, XAS and SEM.

A large fraction of the iron in the investigated material is present as free Fe-phases, which are sensitive to changes in the gas environment. After exposure to oxidizing gases the free Fe phases are: Fe_2O_3 and Fe_3O_4 or $MgFe_2O_4$. Upon exposure to reducing gases, the iron oxides are converted into Fe^0 and Fe_3C and formation of graphitic carbon is observed.

In addition, the elemental composition of the surface changes dramatically depending on the gas composition. After exposure to oxidizing environments, the amount of Fe at the surface is twice as high as after reduction. The reduction of the iron oxides upon switching from oxidizing to reducing conditions shows that olivine transports oxygen from the combustor into the gasifier. Finally, both the decreasing amount of surface-Fe and the carbon deposition observed after exposing olivine to reducing conditions can result in significant catalyst deactivation.

3.1   INTRODUCTION

Gasification in fluidized-bed reactors is one of the preferred routes for converting biomass into useful, sustainable and CO_2 neutral fuels. An attractive feature of biomass gasification is that the resulting primary products, CO, H_2, CO_2 and CH_4 can easily be integrated within the present infrastructure. Technology for converting CO and H_2 into conventional fuels, such as diesel or substitute natural gas, is already at hand, as well as an extensive distribution system for natural gas.

In a conventional fluidized-bed reactor, gasification and partial combustion take place in the same chamber. Therefore, if air is used as gasification medium, the product gas contains both CO_2 and N_2, requiring a costly separation process. This can be avoided by using a dual fluidized bed reactor [1, 2], where gasification takes place in the absence of air and steam is used as a gasification medium. The bed material and the residues from the gasification process (mainly char) are then circulated into a second chamber where they are exposed to air. The resulting combustion generates heat, and the endothermic gasification process can be sustained by re-injecting the hot bed material into the first chamber. In this way, a major part of the CO_2 is conveniently separated from the product gases (allowing for sequestration) and contamination by N_2 and nitrogen-containing species is avoided. However, tar-formation, resulting from incomplete conversion of the biomass, still constitutes a major obstacle in the way of realizing competitive, large scale production of fuels from biomass. Condensation of tars leads to contamination and clogging of the reactor and subsequent pipes, eventually causing malfunction of the system. By using a catalytically active bed material, it has been shown that the tar concentration in the product gas can be decreased [3, 4, 5, 6].

A catalytic bed material needs to be non-toxic, cheap and attrition resistant. A widely used and investigated candidate is the naturally occurring mineral olivine ($(Mg,Fe)_2SiO_4$) [1, 4, 7, 8, 9, 10, 11]. Although this material has proven activity for tar reduction, the underlying catalytic mechanism is not clear. Furthermore, the exact nature of the material under operational conditions is unknown, making optimization of the

catalyst and the process conditions difficult. Previous work points at Fe as the catalytically active component in olivine as well as in other Fe-containing materials [3, 12, 13]. However, at the temperatures typically applied during gasification (between 700 and 1000 °C) olivine is only thermodynamically stable in gas compositions with partial oxygen pressures within a fairly narrow interval [14] (note that even gases that are nominally oxygen-free may have a partial pressure of oxygen due to chemical equilibrium reactions). It is therefore expected, both from theory and from experimental work that the mineral is subject to significant changes under gasification conditions.

In this chapter, the aim is to clarify the changes in phase composition of olivine upon exposure to the gases present during gasification of biomass at relevant temperatures and for various durations. A naturally occurring olivine is studied, previously shown suitable as catalytic bed material [4, 8, 10, 11]. Exposure to gases is done in a quartz-tube flow-reactor with good control over gas environment and process temperature.

3.2 EXPERIMENTAL

3.2.1 *Materials*

Olivine from Magnolithe GmbH, Austria was used in all experiments. A 3 h, 1600 °C calcination of the material was performed by the mineral supplier. The grain size during this pre-calcination was on the order of 10 mm. Prior to experiments, the olivine was grinded or ball-milled to a powder. The grain diameters were on the order of a few tens of or a few micrometers in diameter, respectively, as estimated from Scanning Electron Microscopy (SEM) images. The specific surface area of the powders, as determined from nitrogen sorption isotherms, was 0.53 m^2/g and 0.8 m^2/g for the grinded and the ball-milled samples, respectively. The larger, grinded particles (0.1 g of sample material per experiment) were used in the experiments analyzed by SEM and X-ray Photoelectron Spectroscopy (XPS) and the ball-milled olivine powder (1 g per experiment) was used for the experiments analyzed by X-ray Diffraction (XRD) and X-ray Absorption Spectroscopy (XAS).

3.2.2   *Treatments*

All treatments of the catalytic olivine powders were performed in a quartz-tube flow-reactor at 750 °C. The gases used were pure Ar, H_2, CO, CO_2 and a 20 vol.% O_2 in Ar mixture. Total flows were set to 200 mL/min. Water was added to the gas streams by passing the gas-mixtures through a bubbler containing de-ionized water, resulting in a water content of 3.5 vol.% at room temperature, as determined by a Mitchell instruments, MDM300 Advanced Dewpoint Hygrometer. In all experiments, the samples were first heated to 750 °C under Ar flow. At this temperature, the gas flow was switched to the reactive gas mixtures for a specified time. After the treatment, the gas mixture was switched back to Ar and the flow-reactor was quickly cooled to room temperature.

3.2.3   *Characterization*

All characterizations were performed ex-situ, after transfer of the powders under ambient conditions from the quartz-tube flow-reactor.

Surface Area: Nitrogen sorption isotherms were measured at –196 °C using a Micromeritics Tristar II 3020, after outgassing the samples for 3h at 180 °C. The Brunauer-Emmett-Teller (BET) equation was used to calculate the specific surface area (S_{BET}).

SEM: A FEI Quanta 3D FEG dual beam was used for the SEM characterizations.

XRD: XRD patterns were recorded using a Bruker D4 Endeavor powder spectrometer using Cu Kα radiation and a scan speed of $0.009° \min^{-1}$. After the high temperature treatments, the olivine powders were mixed with 6% of pure NaCl for accurate calibration of the peak positions. The XRD-references and their respective ICDD-file numbers used where; $(Mg,Fe)_2SiO_4$ #71-1080, $(MgSiO_3)$ #35-610 and 19-606, α-Fe_2O_3 #71-5088, γ-Fe_2O_3 #39-1346, Fe_3O_4 #71-6336, $MgFe_2O_4$ #17-464, FeO #89-687, α-Fe #65-4899, Fe_3C #35-772, graphite #75-1621, MgO #4-829 and NaCl #75-306.

XPS: XPS-spectra were taken using a Kratos Axis Ultra and a Thermo Scientific K-alpha spectrometer with monochromatic Al Kα sources. Analysis and quantification of the measurements was performed using the

Casa-XPS software and Wagner sensitivity factors [15]. Charge neutral-ization was always used and the spectral position adjusted to the Si 2s peak of olivine at 153 eV [16]. For quantification the Mg 2p, Fe 3p, Si 2s, C 1s and O 1s signals were used.

3.3 RESULTS

The experiments presented in this chapter are divided into two sections. The focus in both sections is on investigating the dynamic behavior of olivine exposed to the gases that are present in a typical biomass gasification reactor. In particular, results investigating how the phase composition and morphology of the material changes upon entering the gasification zone from the combustor are described. The experiments described in the first section were done to investigate long-term behavior (hours) of olivine under gasification, i.e. what happens to the catalyst after extended exposure to the gases present in a gasification reactor. In the second section the focus is on the short-term dynamics of the material, i.e. the materials behavior on time scales of one to a few tens of minutes. More specifically, the aim is to answer the question: how fast does the surface elemental composition change in response to a change in the gas environment? All together, this chapter aims at clarifying whether olivine is best thought of as a stable material or if it is a catalyst in constant transition from one configuration to another during use in a dual fluidized-bed gasifier.

3.3.1 *Long Term Trends*

3.3.1.1 *Long term behavior, six standard treatments, four characterization techniques*

Grinded or ball-milled olivine powder samples were treated in a quartz-tube flow-reactor in various gas mixtures, aiming at mimicking the con-ditions in a dual fluidized-bed reactor. The conditions in the combustion zone were accurately reproduced by flowing synthetic air (20% O_2/Ar), here after referred to as O_2, over a thin layer of olivine powder at 750 °C

Table 3.1: Names of the samples presented in the figures in section 3.3.1 and details of the treatment sequences.

Name in figures	1 h, 750 °C, gas flow	1 h, 750 °C, gas flows
Before treat.	Not applied	Not applied
O_2	O_2/Ar 200 mL/min	Not applied
O_2-H_2O	O_2/Ar 200 mL/min	Ar 200 mL/min, 3.5 vol.% H_2O
O_2-H_2O/CO/H_2	O_2/Ar 200 mL/min	CO 100 mL/min, H_2 100 mL/min, 3.5 vol.% H_2O
O_2-CO/H_2	O_2/Ar 200 mL/min	CO 100 mL/min, H_2 100 mL/min
CO	O_2/Ar 200 mL/min	CO 200 mL/min
H_2	O_2/Ar 200 mL/min	H_2 200 mL/min

for 1 h. The conditions for olivine entering the gasification zone from the combustor are somewhat more difficult to simulate since the concentration of the various gases depend on the process conditions as well as on the quality of the biomass and the residence time. Furthermore, the environment that the catalyst is exposed to in the gasification zone is not homogeneous since biomass and steam are gradually converted into products gases. Therefore olivine was first exposed to synthetic air for 1 h as above, and subsequently to the product gases CO and H_2, either separately or in 50/50 vol.% mixtures, for another hour. Since water is one of the other main constituents of the gas mixture in the gasification zone, 1 h pre-oxidized olivine was also exposed to water saturated Ar and syngas by passing the gas streams through a water bubbler. In total seven samples were examined for the long-term behavior. One of them was left untreated and the six remaining samples were treated at 750 °C for 1 h in O_2. Five of the oxygen-treated samples were subsequently treated for another hour (750 °C) in mixtures of Ar, H_2, CO and H_2O, as described in Table 3.1. Samples subjected to these treatments were then characterized using SEM, XRD, XAS and XPS.

Figure 3.1 shows the most interesting SEM micrographs of surfaces of untreated, oxidized and reduced olivine. The surface of the untreated olivine (Fig. 3.1a) is smooth and flat, whereas oxidation for 1h results in the formation of crystallites (Fig. 3.1b). Olivine that has been exposed to water or H_2 after the oxidation still shows crystallites at the surface, but less pronounced. Especially for the H_2-reduced olivine, the crystallites are substantially smaller and rounder (Fig. 3.1c). The three samples exposed
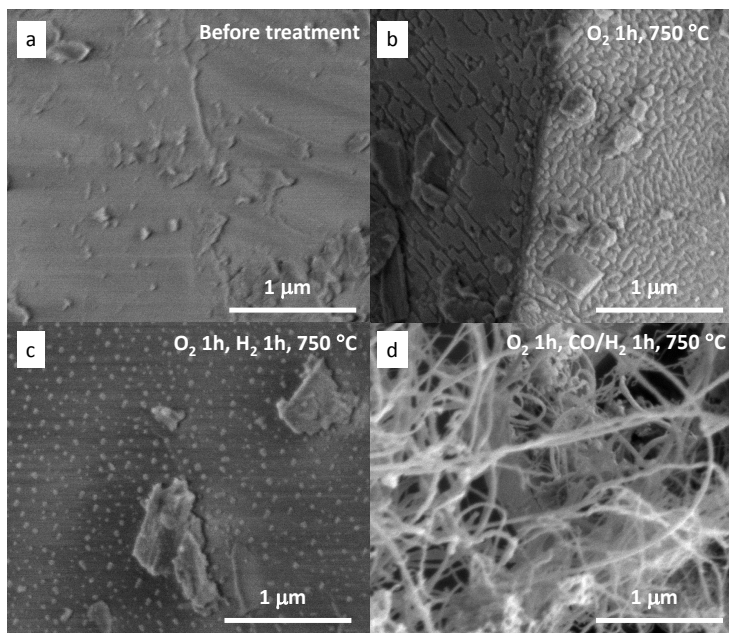
Figure 3.1: SEM micrographs of olivine before (a) and after treatment at 750 °C for 1 h in oxygen (b) followed by 1 h in H_2 (c) or CO/H_2 (d)

to CO-containing gases after oxidation all show deposition of material on the surface. The structure of the deposited material suggests that it consists of carbon fibers (Fig. 3.1d).

Figure 3.2 shows the XRD patterns of seven ball-milled olivine powder samples after the treatments described above. The diffraction peaks of olivine and the strongest peaks of the relevant minor phases observed in the patterns are indicated. All spectra have been normalized to the main diffraction peak of olivine at $2\theta = 36.5\,^\circ$.

It is clear that the main crystalline constituent in all of these samples is olivine. The other crystalline phase that is present in all the samples, regardless of treatment, is pyroxene ($MgSiO_3$). It is also clear from these measurements that the other crystalline phases that form during oxidation and reduction are various iron compounds, graphite and magnesium oxide. This is illustrated in Figure 3.3, where close-ups on the regions of
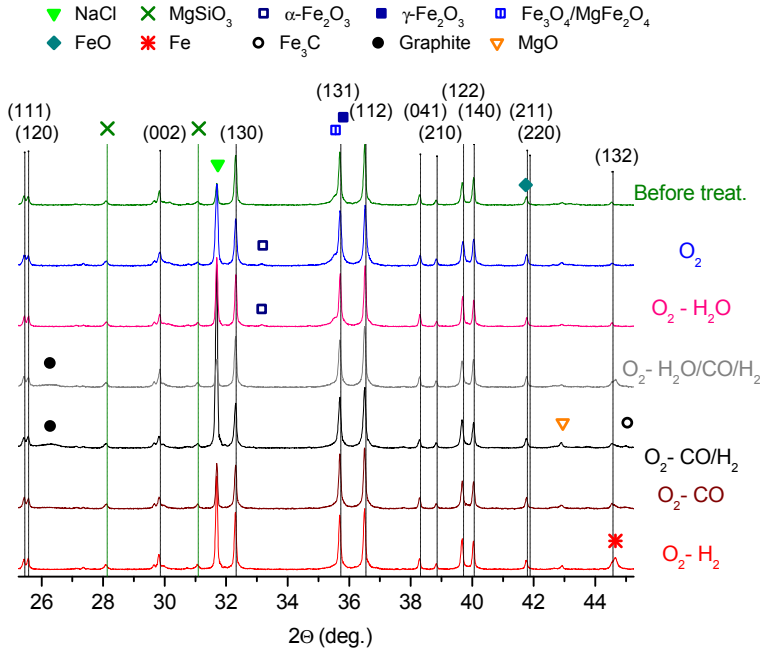
Figure 3.2: XRD patterns of olivine before and after treatment at 750 °C, 1 h in oxygen followed by 1 h in various mixtures of H_2, CO and H_2O. The diffraction peak indices of olivine are indicated together with the position of the main diffraction peak corresponding to other phases observed in the patterns

interest are shown, with the position of the strongest diffraction line of the formed phases indicated.

Fig. 3.3c shows that the material contains a significant fraction of one or both of the indistinguishable spinel phases Fe_3O_4 and $MgFe_2O_4$, even before any high temperature treatment is applied. After treatment in O_2 an additional hematite (α-Fe_2O_3) phase evolves (Fig. 3.3c). For the case where the O_2 treatment is followed by a treatment in H_2O, these phases remain unchanged, whereas a subsequent reducing treatment removes them completely. During reducing treatments, iron carbide (Fe_3C) and/or metallic iron (α-Fe) form (Fig. 3.3e) instead of the iron oxide phases that were present after the initial oxidation treatment. The iron carbide is only observed in the samples treated in CO containing gases. In addition,
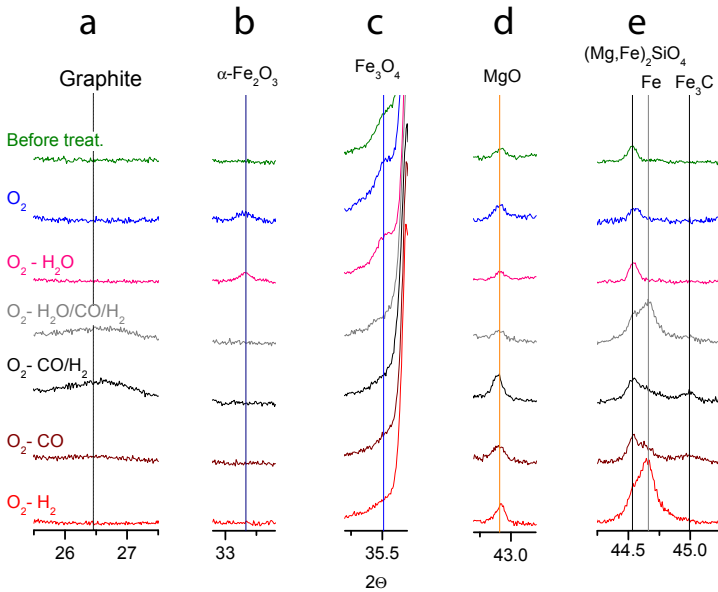
Figure 3.3: Close-ups on the regions where changes are observed in the XRD patterns displayed in Fig. 3.2

a distinct graphite peak can be seen in the patterns of these samples (Fig. 3.3a). This observation lends further support to the hypothesis that the deposits on these samples, observed in SEM (Fig. 3.1d), are indeed carbon fibers. Another observation worth pointing out is that there seems to be a slight increase of magnesium oxide (MgO) in samples treated in H_2 and CO/H_2.

In Figure 3.4a, the XAS-spectra are presented of olivine powders subject to the same treatments as described above. The main observations are that the treatment in O_2 and O_2 followed by H_2O leads to a shift of the main absorption edge towards higher energies. Oxidation followed by reduction in H_2 and CO containing gases on the other hand, leads to a shift to lower energies. Fig. 3.4b shows spectra of iron, iron-oxides and -carbide, presented previously in [17], for comparison. The reference spectra suggest that the shifts observed after oxidation can be interpreted as transformation of the material towards Fe_3O_4, γ-Fe_2O_3 and α-Fe_2O_3. The shifts of the olivine spectra to lower energies as a result of treatment
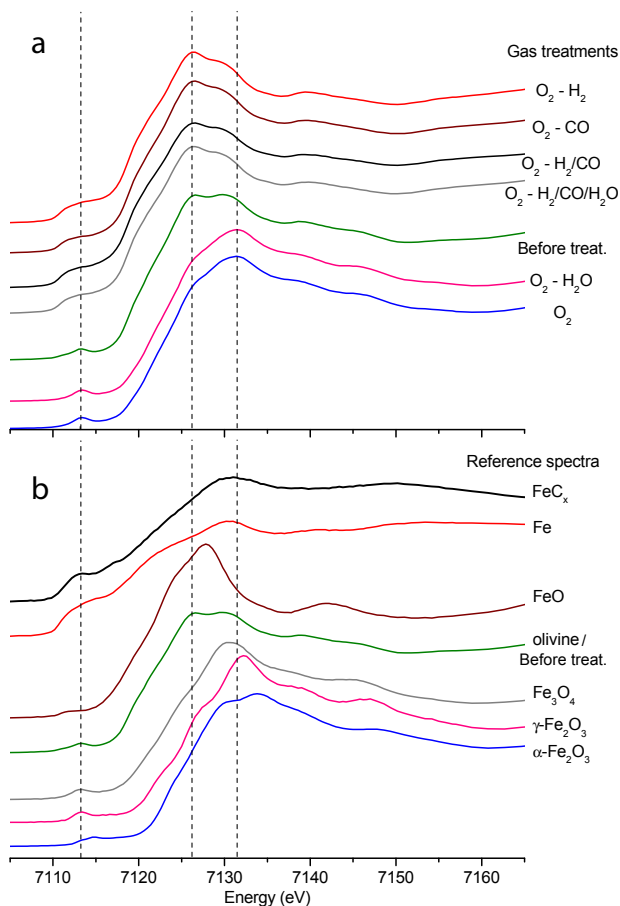
Figure 3.4: a) XAS spectra showing olivine samples before and after treatment at 750 °C, 1 h in O_2 followed by 1h in various mixtures of H_2, CO and H_2O and b) reference spectra of Fe-containing materials. The dashed lines have been added as a guide to the eye

in reducing atmospheres, on the other hand, suggests that metallic Fe, FeO and iron carbide (FeC_x) form, thus confirming the trends observed in XRD.

These trends can be clarified and quantified using linear combinations fits of the references spectra in Fig. 3.4b to reproduce each spectrum in Fig. 3.4a. The weight of each reference spectrum in the fit then corre-

sponds to the amount of that phase present in the material after each treatment. In lack of a good, pure olivine reference, the "before treatment" sample is used to represent the original material. From our XRD measurements, it is clear that this sample contains significant quantities of $MgSiO_3$ and Fe_3O_4 or $MgFe_2O_4$. Furthermore, from the literature it is known that about 45% of the iron in the Austrian olivine (from Magnolithe, as that used in this study) persists in the form of free iron oxide phases [9]. Although the use of a non-pure reference in the linear combination fitting is not ideal, it still provides useful information on the new phases formed after the different treatments. The results are presented in figure 3.5, as change in phase content compared to the untreated material. Positive numbers indicate that the presence of the corresponding phase has increased and vice versa.

This analysis shows that between 25 and 45% of the Fe-containing fraction, present in the original material, is affected by the treatments. Consequently the majority of this fraction remains unaffected. After treatment in oxidizing gases, the amount of iron present as Fe_3O_4, γ-Fe_2O_3
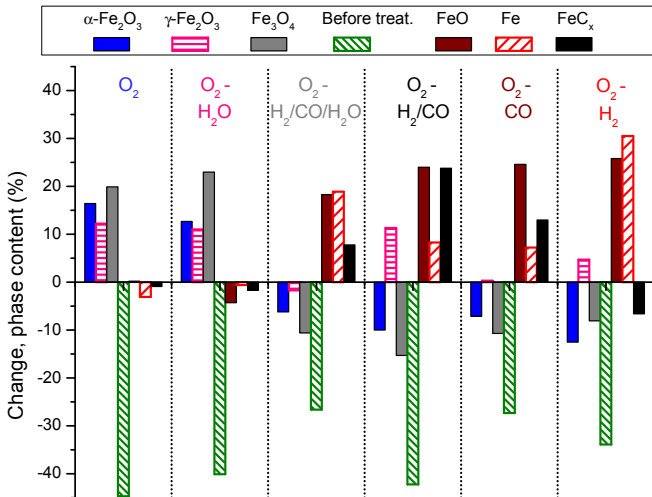
Figure 3.5: Quantification of the change of the content of various Fe-phases present in olivine, before and after treatments in various gas mixtures from linear combination fitting of the XAS spectra presented in Fig. 3.4

and α-Fe_2O_3 increases significantly. Oxidation for 1 h followed by 1 h under reducing conditions converts these iron oxides into metallic Fe, FeO and, if the reducing gas contains CO, into FeC_x. The largest amount of FeC_x is observed after treatment in dry syngas and the largest amount of metallic Fe is observed after treatment in hydrogen.

The surface properties of olivine powders subjected to the same oxidizing and reducing treatments as discussed above were investigated using XPS. Figure 3.6 shows the normalized spectra for the four elements constituting olivine after each treatment.

These measurements show, in similarity with the previously presented XRD and XAS results, that the main changes apply to the iron in the material. The Si 2s peaks, on the other hand, show no significant changes and were therefore used for charge correction of the spectra using the energy previously reported for Si 2s in olivine at 153 eV [16]. Likewise, no significant changes are observed in the Mg 2p peak after the various treatments. In contrast, the Fe 2p region indicates several interesting surface transformations. Although it is not straightforward to exclusively identify different Fe-phases from XPS measurements, it is possible to determine the oxidation state of the material. Literature [18, 19, 20] reveals that the presence of a main Fe $2p_{3/2}$ peak at 711 eV and a satellite peak at 719 eV is characteristic for Fe^{3+} as found, e.g. in Fe_2O_3. For a Fe^{2+}-containing material (as found in FeO or olivine), the corresponding main peak appears at 709 eV and the satellite at 715 eV. For reduced iron (Fe^0), the main peak is positioned at around 707 eV and there are no satellite peaks. These positions are marked with dashed lines in the figure. It is clear that an Fe^{3+}-rich phase (presumably γ-Fe_2O_3 or α-Fe_2O_3) is formed at the surface as a result of exposure to oxidizing conditions (O_2 and O_2 followed by H_2O). This is evidenced by the presence of a broad satellite peak in the Fe 2p spectra around 719 eV as well as by the formation of a low-energy shoulder in the O 1s spectra at 530 eV (typical for metal oxides [20]). For the olivine powders that were first oxidized for 1 h and then subjected to reducing conditions for 1 h, the 719 eV satellite has disappeared or significantly decreased, the main peak is broadened and shifted towards lower binding energies and a peak at 707 eV is observed. These observations indicate that the Fe^{3+}-
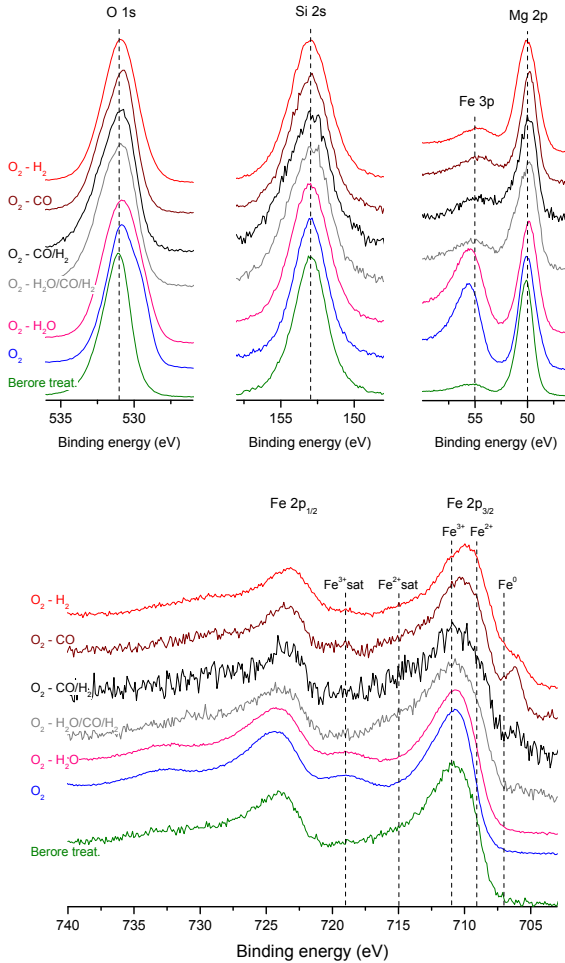
Figure 3.6: XPS spectra of the elements that constitute olivine, before and after treatment at 750 °C, 1 h in oxygen followed by 1 h in various mixtures of H_2, CO and H_2O

phase formed during oxidation is reduced to a combination of Fe^{2+} and Fe^0-dominated iron phases, such as olivine, Fe_3O_4, FeO, α-Fe or FeC_x. Furthermore, the relative intensities of the Fe 3p and Mg 2p peaks indicate significant changes in the amount of Fe present at the surface. Exposure

to oxidizing conditions leads to an increase of surface-Fe whereas a subsequent reduction results in levels similar to those observed before oxidation.

It should be noted that these experiments were not done *in-situ*, i.e. the samples were exposed to air upon transfer from the treatment reactor to the XPS. Therefore, estimations based on the amplitude of the Fe^0 peak is expected to underrate the presence of metallic iron, since surface oxides are known to form rapidly at room temperature and ambient atmosphere. The higher noise levels in the spectra from samples treated in CO-containing gases derives from lower signal intensities due to substantial deposition of carbon on the surface. This will be discussed in depth in the following sections.

3.3.1.2 *Intermediate Gas Compositions*

To investigate the changes in surface composition as a result of exposure to gases with different oxidizing power in greater detail, various mixtures of CO_2/CO were used. By changing the relative content of the two gases, the oxygen content in the gas can be fine-tuned via the equilibrium reaction:

$$CO + 0.5O_2 \rightleftarrows CO_2 \tag{3.1}$$

Figure 3.7 shows normalized C 1s, Fe 3p/Mg 2p and Fe 2p peaks for olivine powders that were first exposed to O_2 for 1 h followed by 1 h in different CO_2/CO gas mixtures with CO_2 contents ranging from 0 to 100 vol.%. After treatment in pure CO_2, the material remains oxidized, exhibiting spectra resembling those after exposure only to O_2 (see Fig. 3.6). However, already after including 10 vol.% CO in the gas mixture, the Fe^{3+} is reduced to Fe^{2+}, as seen by the decreasing intensity of the Fe 2p satellite peak at 719 eV. Very little happens to the material when the CO_2 content is decreased further down to 20 vol.% (spectra for concentrations in between not shown), whereas below this concentration the peak at 707 eV, characteristic for metallic iron (Fe^0) or iron carbide, slowly starts to grow. A decrease in the Fe 3p/Mg 2p ratio is also observed as the CO_2 content is reduced, indicating a decrease of the iron content at the surface. For samples treated in CO_2-rich gas mixtures, the C 1s peak is small and
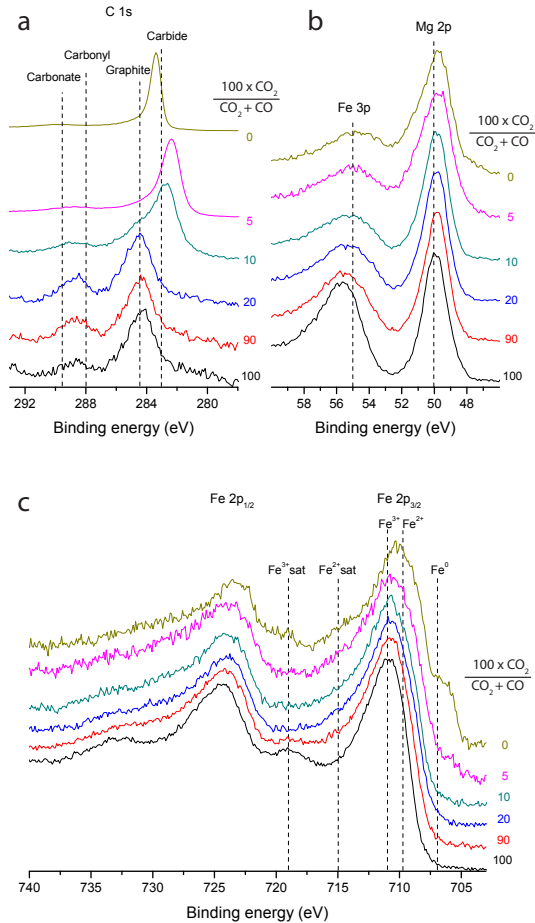
Figure 3.7: XPS spectra from samples treated at $750\,^{\circ}\text{C}$ in O_2 for 1 h followed by 1 h in CO_2/CO mixtures with CO_2 contents of 0, 5, 10, 20, 90 and 100 vol.%

representative for carbon species naturally introduced onto the sample surface by exposure to airborne contaminants during transfer from the quartz-tube reactor to the XPS chamber. However, when the CO_2 content of the gas mixture is decreased to 10 vol.% a new carbon peak, typical for carbides [20], starts to grow at around 283 eV. For even lower CO_2 contents the carbon peak amplitude grows significantly and for pure CO
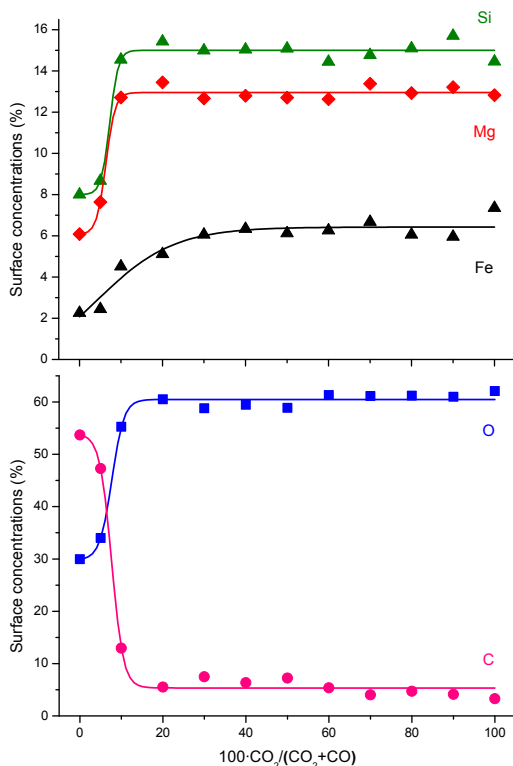
Figure 3.8: Quantification of the XPS-derived elemental composition of the olivine surface after treatment at 750 °C in O_2 for 1 h followed by 1 h in various mixtures of CO_2 and CO ranging from 0 to 100 vol.% CO_2. The lines are sigmoidal fits serving as guides to the eye

a shift of the peak to higher energy is observed. As observed in the previous sections, both iron carbide and graphitic carbon form on the sample surface after treatment in pure CO. However, repeated measurements of samples subjected to the same treatments show that the position of the carbon peak varies significantly between nominally identical samples. This is likely due to differential charging of the conducting carbon layer deposited on the insulating olivine; C 1s spectra of samples with thick carbon over-layers should therefore be interpreted with caution.

The elemental surface composition of the powders exposed to the various CO_2-CO mixtures, calculated from the XPS-data, is presented in figure 3.8. The quantification clearly demonstrates that the most significant changes of the surface elemental composition take place when the CO_2 content of the gas mixture is decreased to 20 vol.% or below. At 20 vol.% CO_2 content, there is first a small decrease in the Fe content at the surface and in more CO_2 deficient gas mixtures, a significant build-up of carbon on the surface is observed.

3.3.2 *Time-Dynamics of the Surface Elemental Composition*

In order to elucidate the dynamic behavior of olivine in different gas environments, fresh, grinded material was exposed to well defined gas environments at 750 °C for various durations and the surface elemental

Figure 3.9: Surface elemental composition of olivine measured with XPS. The material was first exposed to O_2 and then to H_2 (open symbols, dashed lines) or H_2O (solid symbols, solid lines). Each measurement point refers to a separate sample subject to the treatment up to that point

composition after each time-interval was analyzed using XPS. Figure 3.9 shows olivine, first exposed to O_2 for durations up to 1h and subsequently exposed to H_2 or H_2O for time durations up to 1 h.

The key observations are the following: (i) upon exposure to O_2, simulating the catalysts presence in a combustion chamber, the amount of iron at the surface increases, initially at the expense of Si and in the longer run at the expense of Mg. (ii) Switching gas environment from O_2 to H_2 reverses this process, i.e. the iron surface content decreases and is initially replaced by Si, and after a longer duration of time, also by Mg. (iii) By switching from O_2 to H_2O, the iron content at the surface is maintained. (iv) The surface concentration of iron is roughly twice as high under oxidizing conditions (O_2 or H_2O) as under reducing conditions (H_2) and (v) the changes in surface elemental composition happen fast and are significant already after one minute. This is true also for the change in chemical state of the surface iron, which goes from the fully oxidized hematite state to the reduced state already after the first minute under reducing conditions.

The exposure of oxidized olivine to H_2 and H_2O serves to simulate the exposure of the catalyst material to the conditions in the gasification zone. However, in the gasification zone, the catalyst is exposed to carbon-containing gases (as well as to the biomass itself), which results in significant changes in the olivine, as demonstrated in previous sections. Figure 3.10 shows a similar sequence of measurements as in Fig. 3.9, but where the oxidation treatment is followed by reduction in syngas and that ends with an oxygen treatment.

Again, the surface content of iron increases during oxidizing conditions and decreases under reducing conditions. However, the most striking feature observed from these measurements is the build-up of carbon on the surface during exposure to syngas. Before exposure to carbon-containing gas, between 4.5 and 6.1% of carbon is observed on the surface of the catalyst. These small quantities of carbon are expected, as a result of the contact with atmospheric contaminants during transfer from the treatment reactor to the XPS. However, after a one minute exposure to syngas, the amount of carbon on the surface is roughly doubled (11.5%) and after an hour carbon constitutes more than 90% of the surface atoms.
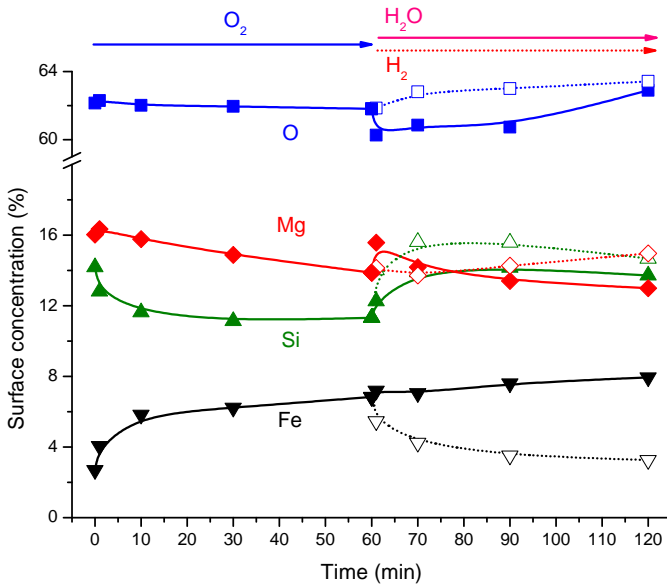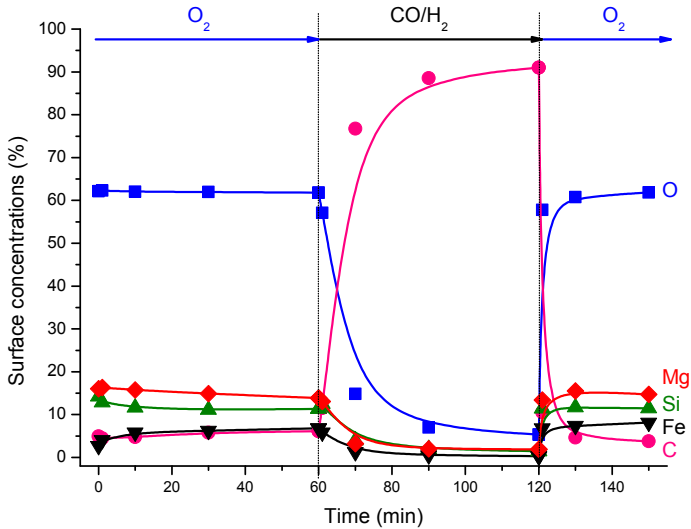
Figure 3.10: Surface elemental composition of olivine measured with XPS. The material was first exposed to O_2 and then to a 50/50 mixture of CO and H_2 and finally to O_2 again. Each measurement point refers to a separate sample, subjected to the treatment up to that point

This carbon layer is then quickly combusted when the sample is exposed to oxygen. A similar build-up of carbon on the olivine surface is observed for the other CO-containing mixes (not shown), and is most significant for the case of pure syngas, somewhat slower in wet syngas and slower yet in pure CO.

To further investigate and emphasize the dynamics of the olivine exposed to alternating gas environments on time scales relevant in a dual fluidized bed reactor, experiments were performed with short pulses of alternating oxidizing and reducing gas. The samples were exposed to oxygen for one minute, oxygen was then purged out with Ar for one minute followed by exposure to CO for one minute and another minute of Ar purging. This four-minute cycle was repeated up to 10 times and the response of olivine after various numbers of cycles (or fraction of cycles) is shown in figure 3.11.

These measurements show that the material readily responds to the changing gas environments on the short time-scales of a treatment cycle.
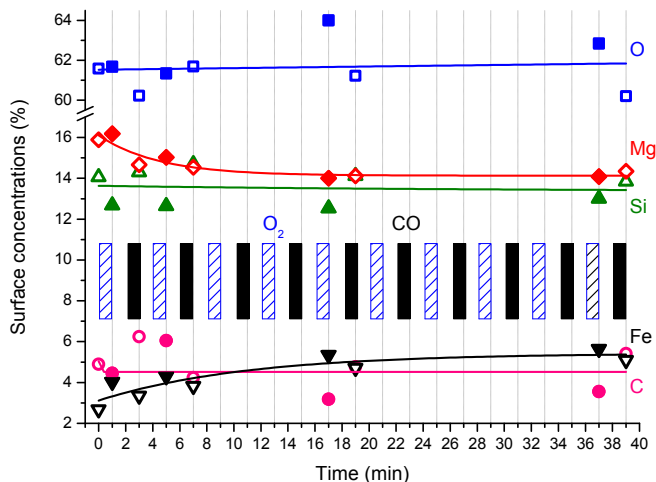
Figure 3.11: Surface elemental composition of olivine measured with XPS after various numbers of alternating O_2-CO cycles at $750\,^\circ$C. Solid symbols represent measurements done after an O_2 step in a cycle and open symbols the material after a CO step. The solid, black rectangles in the background mark the time where the samples were exposed to CO and the blue, striped rectangles mark where there was an O_2 flow. The solid lines are exponential fits to the data, serving as guides to the eye

After the oxidation step in each cycle, the amount of iron at the surface increases significantly at the expense of Si, whereas the opposite is true after the reduction steps. Superimposed on this effect is a slower response, in which the amount of iron at the surface increases at the expense of magnesium. Furthermore, no accumulation of carbon on the surface is observed after repeated cycles, although there is generally more carbon present after a CO step than after an O_2 step, as expected.

3.4   DISCUSSION

The experiments presented in this chapter demonstrate that olivine is a very dynamic material under conditions typical for biomass gasification. Changes in the gas composition at relevant temperatures result in a fast response in the chemical state of the material. These changes predominantly concern the Fe present in the material.

The XRD measurements (see Fig. 3.2 and Fig. 3.3) show that the Austrian olivine contains a significant fraction of the crystalline spinel phase (Fe_3O_4 or $MgFe_2O_4$), even before any high-temperature treatments were applied. This is in agreement with previous studies [9, 10], where Mössbauer spectroscopy showed that almost half of the iron in olivine (of the same origin as that studied here) is present in the form of free oxides, predominantly $MgFe_2O_4$ and non-crystalline α-Fe_2O_3. The presence of these free Fe-phases stems from exclusion of Fe from the olivine matrix during the pre-treatment done by the mineral supplier.

XRD and XAS (Fig. 3.2, Fig. 3.3, Fig. 3.4 and Fig. 3.5) show that oxidation of the material at 750 °C in O_2 for 1 h results in formation of the Fe^{3+}-rich phases: α-Fe_2O_3, γ-Fe_2O_3, and Fe_3O_4 and/or $MgFe_2O_4$, the latter two henceforth referred to as spinel. The XRD measurements show clearly the formation of crystalline α-Fe_2O_3 while the XAS measurements indicate the formation of γ-Fe_2O_3 and spinel as well. This discrepancy can stem from the fact that both γ-Fe_2O_3 and spinel XRD-patterns overlap significantly with the main peaks of olivine and that small changes therefore are hard to detect. Indeed, the elemental composition of our olivine can be expressed as $(Mg_{0.93},Fe_{0.07})_2SiO_4$ [9], indicating that the vast majority of the material is actually constituted of pure Mg_2SiO_4, with no inclusion of Fe. Therefore, even a total conversion from one Fe-containing phase to another, would come through as a relatively small change in the XRD measurements. In XAS, on the other hand, only the Fe in the material contributes to the measurement and the material does not have to be crystalline. Therefore, the latter technique is sensitive even to minor changes in the Fe-carrying phases and detects changes also in amorphous material.

Subsequent treatment of the oxidized olivine in H_2O-saturated Ar for 1 h at 750 °C shows no significant change in the Fe-phases. A similar treatment in reducing gases, on the other hand, results in a clear decrease of the Fe^{3+}-rich phase content. Both XRD and XAS show that these phases are converted to metallic Fe and, if the reducing gas contains CO, to iron carbide. In addition, the XAS measurements suggest the formation

of FeO, which is not seen in XRD, likely for the same reasons already discussed above. Both techniques show that the formation of metallic Fe is most pronounced after treatment in H_2. Iron carbide formation, on the other hand, is most efficient upon treatment in dry syngas.

These measurements show that the main change in the material upon exposure to oxidizing or reducing gases is simply conversion of the Fe already excluded from the olivine matrix, e.g. conversion of iron oxides to metallic iron and/or carbide upon reduction. However, both the XRD and XAS-measurements indicate that additional free Fe-phases are formed during these treatments, a somewhat surprising result considering the low temperatures applied. The XAS data in particular suggest that the observed Fe-phases are formed at the expense of the original Fe-carrying material, which consist at least to 50% of olivine and pyroxene. The 26 – 45% decrease of the original material content, suggest that another 13 – 22.5% of the Fe is converted from the olivine or pyroxene phases into other iron phases.

The formation of free Fe-phases from olivine is in accordance with thermodynamic calculations [14], showing that olivine is only stable in a fairly narrow range of oxygen partial pressures, termed the stability field. For gas environments with a higher oxygen partial pressure, olivine is expected to decompose into SiO_2, $MgSiO_3$ and Fe_3O_4. At oxygen contents below the stability field of olivine, decomposition to SiO_2, $MgSiO_3$ and Fe^0 is expected. Under oxidizing conditions corresponding to air, Fe_2O_3 is expected to form from Fe_3O_4, whereas reduction in H_2, CO or mixes thereof is expected to result in the formation of metallic Fe and FeC_x, respectively [13, 21]. Thus, in all these measurements, olivine and the free Fe-phases behave in accordance with thermodynamic predictions. However, no SiO_2 is observed in our XRD measurements, indicating that the Fe exclusion leaves behind an amorphous SiO_2 component.

Thermodynamics determine which of the mineral phases are stable in a certain gas environment. Therefore, changes in the gas composition are expected to lead to changes in the material. These changes should be most significant at the surface of the material, where the material is in direct contact with the gases. Indeed, XPS (see Fig. 3.6) characterization of the materials surface reveals the same trends as observed by the bulk

techniques XRD and XAS. After treatment in oxidizing environment, the Fe is oxidized to an Fe^{3+} type of material. Under the conditions applied here, this phase should be α-Fe_2O_3, as also observed by XRD. After treatment in reducing gases, the Fe^{3+} is reduced to a combination of Fe^{2+} and Fe^0. The Fe^0 is characteristic for metallic Fe or FeC, while the Fe^{2+} is the signature of a Fe_3O_4, FeO or olivine [16, 18, 19, 20]. Upon exposure to air at room temperature, reduced Fe is quickly oxidized to form a thin surface oxide layer. Therefore, since the high-temperature treatments were done ex-situ, an oxidized surface layer is expected, also on the reduced samples. Since a significant contribution from Fe^0 is still observed in the XPS-measurements and since large amounts of metallic Fe and FeC are observed with XRD, it is fair to assume that the surface was completely reduced during treatment, but re-oxidized during transfer to the XPS-chamber.

Another important observation from the XPS measurements (see Fig. 3.6, Fig. 3.7, Fig. 3.8, Fig. 3.9, Fig. 3.10 and Fig. 3.11) is that the amount of Fe at the surface of the olivine increases after oxidizing treatment. This has been reported previously [12, 22] as a consequence of treatments at 900 °C for 1 h or longer and was then interpreted as surface enrichment of Fe at the expense of Mg or as redistribution of the surface Fe. However, by investigating also the short term behavior (see Fig. 3.9 and Fig. 3.11), it was found that the Fe enrichment at the surface takes place on two time scales; a fast response on the time scale of one minute and a slower response, on the time scale of 20 minutes to 1 h. On the short time scale the amount of surface-Fe increases at the expense of Si, whereas on the longer time scale, Fe increases at the expense of Mg. Upon switching from oxidizing to reducing conditions, the trends are reversed i.e. the Fe surface concentration decreases first quickly, re-exposing Si and then continues to decrease more slowly, re-exposing Mg. It should also be mentioned that the oxidation-state of the surface-Fe changes from the Fe^{3+} dominated state (observed after oxidation) to the Fe^{2+}/Fe^0 state (observed after reduction), already during the first minute after switching gases.

The long-term change in surface elemental composition is consistent with an enrichment mechanism due to diffusive exchange of Fe- with

Mg-atoms at the surface of olivine, as suggested in previous work [12]. The short-term behavior, however, is not likely due to diffusion, which is a slow process at these temperatures [23, 24]. A tentative explanation for the short-term change in surface concentration of Fe can instead be provided by considering the following: It is known that natural minerals in general, including olivine, are not perfectly homogeneous materials on the microscale [25, 26]. It is also known that almost half of the Fe in the olivine, investigated in this study, is present in the form of free Fe-phases [9, 10]. Furthermore, Fe is more likely to segregate out of Fe-rich olivines, since Fe-diffusion is faster in these domains and since the stability field for Fe-rich olivine is narrower than that of Mg-rich olivines [14, 24, 27]. Free Fe-phases are known to form hematite crystallites at the surface of olivine upon oxidation [25, 28, 29, 30], in agreement with what has been observed in SEM (see Fig. 3.1d). Assuming that Fe has segregated out predominantly from Fe rich domains in the olivine, the olivine can be seen as a material where Fe-particles are supported on amorphous SiO_2. Since the volume of Fe-particles increases upon oxidation and decreases upon reduction, this would lead to the observed effect with a fast increase of the Fe signal on the expense of Si, as observed here. It is also important to note that the amount of surface-Fe changes reversibly (or increases slightly) after repeated oxidation-reduction cycles (Fig. 3.11), indicating that no sintering of the free Fe occurs.

The experiments discussed so far were all done using mixtures of the gases that are present in a biomass gasifier. While the conditions in a combustor are accurately simulated by the oxidation in O_2/Ar, the other gas mixtures are not reproducing the conditions during gasification as accurately. These are rather somewhere in-between the oxidizing environment of H_2O-saturated Ar and the reducing mixtures of H_2, CO and H_2O. This interval of intermediately oxidizing gas-mixtures was investigated through the experiments with CO_2/CO mixtures (Fig. 3.7 and Fig. 3.8). It was seen that for the majority of CO_2/CO mixtures (20–90 vol.% CO_2) the surface-Fe was neither in the completely oxidized Fe_2O_3 state, nor the reduced Fe^0 state, but in an intermediate state. This state is dominated by Fe^{2+} which is significant both for Fe_3O_4, FeO and olivine. These phases cannot be distinguished in these measurements. However,

it is known that for lower CO_2 concentrations, FeO is thermodynamically favored over Fe_3O_4. The reduction of the Fe_3O_4 crystallites to smaller FeO provides a tentative explanation of the observed decrease in Fe surface content at around 20 vol.% CO_2, preceding the C deposition.

3.4.2   *Carbon*

This chapter provides extensive proof of carbon build-up on the surface of olivine after treatment in CO-containing gas. XRD shows that in addition to the formation of metallic Fe and Fe_3C, a significant amount of crystalline graphitic material is formed. This is confirmed by SEM, where carbon fibers can be clearly seen. The carbon formation is most efficient in syngas, followed by water saturated syngas and pure CO. The deposition of carbon on Fe-containing catalysts is a well-known phenomenon and is due to the Boudouard reaction (Eq. 3.2) and the CO hydrogenation reaction (Eq. 3.3) [31, 32]:

$$2CO \rightarrow CO_2 + C_{solid} \qquad\qquad (3.2)$$

$$CO + H_2 \rightarrow H_2O + C_{solid} \qquad\qquad (3.3)$$

In pure CO, equation 3.2 represents the only possible source of deposited carbon, while in syngas both reactions are possible. The latter of the two reactions have been found to be the faster source of carbon deposition on Fe [31]. Thus the results found here with carbon build-up being fastest in dry syngas and slowest in pure CO, are not surprising.

From the experiments with varying compositions of CO_2/CO (see Fig. 3.7 and Fig. 3.8), it is clear that carbon deposition is preceded by reduction of Fe^{2+} to Fe^0. This is in accordance with theoretical and experimental observations [13, 32]. It is also predicted that there is a narrow interval in gas composition where metallic Fe is stable but carbon-deposition is not yet thermodynamically allowed. Furthermore, Nordgreen et al. [13] showed that tar cracking on Fe-based catalysts is significantly more efficient on metallic Fe than on oxides. However, carbon-deposition by decomposition of CO and/or H_2 under too reduc-

ing conditions is of course unwanted in a practical application. Therefore, these results suggest that the optimum gas composition, under which Fe_3O_4 reduction starts but carbon-deposition is still suppressed, is between 15–20 vol.% CO_2, in a CO_2/CO mixture at 750 °C.

The experiments where the catalyst was first treated in CO-containing gas (resulting in carbon-deposition), followed by oxidation (see Fig. 3.10 and Fig. 3.11) show that deposited carbon is quickly combusted. For the syngas-treated sample, where the surface is almost completely covered in carbon, about one third of the deposited carbon is removed already after one minute. After 10 minutes the carbon-level is back at what it was before deposition. For the experiments where samples were repeatedly exposed to cycles of O_2 followed by CO, no build-up of carbon is observed showing that the carbon deposited during CO exposure is rapidly and completely combusted by the subsequent oxidation step.

3.4.3 *Magnesium*

The small quantities of MgO in the material, observed with XRD (Fig. 3.2 and Fig. 3.3), stem either from natural impurities in the mineral or from the high-temperature pre-treatment. At the temperature used in this study, no MgO formation is expected. However, the samples that were not exposed to any gases at all (except for air at room temperature) or that were exposed to water containing gas at 750 °C, contain the smallest amounts of MgO. This could be due to the formation/decomposition of a magnesium hydroxide or oxalate in the presence/absence of water [33]. This observation was not pursued further, but is pointed out as a possible interesting follow-up of this work. Especially since presence of MgO is usually not discussed in the context of olivine, although it is also present in dolomite, another mineral frequently applied as a tar cracking catalyst in biomass gasification [7, 34].

It should also be mentioned that the Mg-content at the surface, as measured by XPS, is consistently underestimated compared to the bulk composition. This appears to be due to an inconsistency in the Wagner sensitivity-factors, rather than due to any real effect. However, it does not

influence the observed trends, merely the absolute content of the element on the surface.

3.5 CONCLUDING REMARKS

There are several important consequences of these observations for the performance of olivine as a catalyst in biomass gasification. The discussion below will predominantly concern dual fluidized-bed reactors, where the bed material/catalyst is continuously circulated from a combustor to a gasifier and back again. The residence time in the combustor and gasifier is typically on the time scales from a few seconds to several tens of minutes.

Supported FeO_x-catalyst: Olivine is not a stable material during conditions typically applied in biomass gasification. It decomposes during high temperature treatment, forming a mixture of olivine and free FeO_x-phases. The material is thus better regarded as a FeO_x-catalyst, supported on Mg_2SiO_4 and amorphous SiO_2, than as a homogeneous material.

Oxygen transport: The presence of significant amounts of free Fe-oxide phases allows for oxygen transport from the combustor into the gasifier, thereby facilitating partial combustion of the biomass and/or product gases. These experiments have showed that the Fe_2O_3 and Fe_3O_4 phases can be completely reduced within one hour. An upper limit to the oxygen transport can thus be estimated as follows: With the material composition corresponding to $(Mg_{0.93}, Fe_{0.07})_2SiO_4$, as calculated from elemental analysis [9], the molar fraction of Fe is 2%. If half of this Fe is present as free, reducible material and if all of it is reduced from Fe_2O_3 to metallic Fe this would correspond to oxygen transport on the order of 1.5 molar% of the bed material or about 1 weight%. With bed material and biomass feeds of 6300 (kg/h) and 160 (kg/h) respectively, as reported in [2], this gives a contribution of 63 kg oxygen per 160 kg biomass in the gasifier. However, the oxygen transport can be limited by conditioning the gas in the gasifier and/or in the combustor or by controlling the residence time in the two chambers, thereby avoiding complete oxidation and reduction. Chapter 4 will deal with oxygen transport in more detail.

Fe-phases and catalytic activity: Several studies point to Fe as the catalytically active element in olivine [3, 13]. However, different Fe-phases catalyze different reactions. Fe_2O_3 is reported to catalyze soot and NO_x conversion [35], Fe_3O_4 is known as a good water-gas shift catalyst [32], FeC_x is suggested as the active component in Fischer-Tropsch catalysis [36, 37] and metallic Fe is known to catalyze the Boudouard reaction and tar decomposition [13, 32]. Therefore, the fast change in the oxidation state of the surface Fe will dramatically influence the catalytic properties of the material. The measurements described in this chapter demonstrate that when an olivine catalyst leaves the combustor, the surface-Fe is present as Fe_2O_3. Upon entering the gasification zone it quickly adapts to the new gas environment. The chemical state of the surface-Fe in a practical situation will critically depend on the gas composition and temperature in the gasifier (thermodynamics). Hence, during the presence in the gasifier the catalytic properties of the catalyst will change accordingly. Whether the material reaches thermodynamic equilibrium, or is kinetically hindered to do so, depends on the temperature and residence time in the gasifier. Therefore, by conditioning the gas mixtures both in the combustor and in the gasifier, the catalytic activity could be vastly changed. In addition, steady state measurements of the activity of an olivine catalyst for tar cracking may be quite misleading if the results are applied to dual fluidized-bed reactors, were the residence time in the gasifier is short.

Carbon build-up: At the extreme end of catalyst reduction, carbon build-up on the surface is observed. In this state, the catalyst actually contributes to the destruction of the product gases. Furthermore, build-up of graphitic carbon on the surface can deactivate the catalyst for tar cracking by covering the active Fe. This once again points to the importance of properly conditioning the gas composition in the gasifier. However, even if graphitic carbon is formed during gasification, this is quickly combusted in air and regeneration of the catalyst is not a problem.

REFERENCES

[1] F. Kirnbauer and H. Hofbauer, Energy & Fuels 25 (2011) 3793–3798.

[2] C. M. van der Meijden, H. J. Veringa, B. J. Vreugdenhil and B. van der Drift, International Journal of Chemical Reactor Engineering 7 (2009) A53.

[3] S. Rapagna , M. Virginie, K. Gallucci, C. Courson, M. D. Marcello, A. Kiennemann and P. U. Foscolo, Catalysis Today 176 (2011) 163–168.

[4] L. Devi, K. J. Ptasinski and F. J. J. G. Janssen, Industrial & Engineering Chemistry Research 44 (2005) 9096–9104.

[5] S. Koppatz, C. Pfeifer and H. Hofbauer, Chemical Engineering Journal 175 (2011) 468–483.

[6] J. Han and H. Kim, Renewable and Sustainable Energy Reviews 12 (2008) 397–416.

[7] L. Devi, K. J. Ptasinski, F. J. J. G. Janssen, S. V. van Paasen, P. C. A. Bergman and J. H. A. Kiel, Renewable Energy 30 (2005) 565–587.

[8] J. N. Kuhn, Z. Zhao, L. G. Felix, R. B. Slimane, C. W. Choi and U. S. Ozkan, Applied Catalysis B: Environmental 81 (2008) 14–26.

[9] D. Swierczynski, C. Courson, L. Bedel, A. Kiennemann and S. Vilminot, Chemistry of Materials 18 (2006) 897–905.

[10] M. Virginie, C. Courson, D. Niznansky, N. Chaoui and A. Kiennemann, Applied Catalysis B: Environmental 101 (2010) 90–100.

[11] J. Pecho, T. J. Schildhauer, M. Sturzenegger, S. Biollaz and A. Wokaun, Chemical Engineering Science 63 (2008) 2465–2476.

[12] L. Devi, M. Craje, P. Thüne, K. J. Ptasinski and F. J. J. G. Janssen, Applied Catalysis A: General 294 (2005) 68–79.

[13] T. Nordgreen, V. Nemanova, K. Engvall and K. Sjöström, Fuel 95 (2012) 71–78.

[14] U. Nitsan, J. Geophys. Res. 79 (1974) 706–711.

[15] C. D. Wagner, Journal of Electron Spectroscopy and Related Phenomena 32 (1983) 99–102.

[16] H. Seyama and M. Soma, J. Chem. Soc., Faraday Trans. 1 81 (1985) 485–495.

[17] P. Thüne, P. Moodley, F. Scheijen, H. Fredriksson, R. Lancee, J. Kropf, J. Miller and J. W. Niemantsverdriet, The Journal of Physical Chemistry C 116 (2012) 7367–7373.

[18] T. Yamashita and P. Hayes, Applied Surface Science 254 (2008) 2441–2449.

[19] A. P. Grosvenor, B. A. Kobe, M. C. Biesinger and N. S. McIntyre, Surface and Interface Analysis 36 (2004) 1564–1574.

[20] C. S. Kuivila, J. B. Butt and P. C. Stair, Applied Surface Science 32 (1988) 99–121.

[21] F. Bonnet, F. Ropital, Y. Berthier and P. Marcus, Materials and Corrosion 54 (2003) 870–880.

[22] J. N. Kuhn, Z. Zhao, A. Senefeld-Naber, L. G. Felix, R. B. Slimane, C. W. Choi and U. S. Ozkan, Applied Catalysis A: General 341 (2008) 43–49.

[23] R. Dohmen, H.-W. Becker, E. Meiß ner, T. Etzel and S. Chakraborty, European Journal of Mineralogy 14 (2002) 1155–1168.

[24] R. Dohmen, H.-W. Becker and S. Chakraborty, Physics and Chemistry of Minerals 34 (2007) 389–407.

[25] D. L. Kohlstedt and J. B. Vander Sande, Contributions to Mineralogy and Petrology 53 (1975) 13–24.

[26] L. E. Mayhew, S. M. Webb and A. S. Templeton, Environmental Science & Technology 45 (2011) 4468–4474.

[27] H. Nagahara, I. Kushiro and B. O. Mysen, Geochimica et Cosmochimica Acta 58 (1994) 1951–1963.

[28] I. Gaballah, S. E. Raghy and C. Gleitzer, Journal of Materials Science 13 (1978) 1971–1976.

[29] L. Lemelle, F. Guyot, M. Fialin and J. Pargamin, Geochimica et Cosmochimica Acta 64 (2000) 3237–3249.

[30] S. Massouh, A. Perez and J. Serughetti, Phys. Rev. B 33 (1986) 3083–3089.

[31] F. W. A. H. Geurts and A. Sacco, Carbon 30 (1992) 415–418.

[32] C. Ratnasamy and J. P. Wagner, Catalysis Reviews 51 (2009) 325–440.

[33] J. A. Wang, O. Novaro, X. Bokhimi, T. Lopez, R. Gomez, J. Navarrete, M. E. Llanos and E. Lopez-Salinas, Materials Letters 35 (1998) 317–323.

[34] E. Gusta, A. K. Dalai, M. A. Uddin and E. Sasaoka, Energy & Fuels 23 (2009) 2264–2272.

[35] S. Kureti, K. Hizbullah and W. Weisweiler, Chemical Engineering & Technology 26 (2003) 1003–1006.

[36] J. Gracia, F. Prinsloo and J. W. Niemantsverdriet, Catalysis Letters 133 (2009) 257–261.

[37] J. W. Niemantsverdriet, A. M. Van der Kraan, W. L. Van Dijk and H. S. Van der Baan, The Journal of Physical Chemistry 84 (1980) 3363–3370.

Oxygen-Transport Capabilities of Olivine

ABSTRACT

This chapter describes the capability of olivine to transport oxygen, when it is used as a bed material in indirect biomass gasification. The iron in olivine can act as a catalyst for the decomposition of tars, produced during the gasification process. Moreover, iron is capable of transferring oxygen to the gasification reactor. Mössbauer spectra show that during oxidation, iron segregates out of the olivine matrix, forming free iron-oxide phases. These free iron phases form metallic iron upon subsequent reduction in hydrogen. Thermo Gravimetric Analysis (TGA) is used to quantify oxygen-transport under alternating oxidizing/reducing conditions. TGA results indicate that at least 18% of all the iron, present in olivine, is capable of transferring oxygen on the time scale of minutes. XPS combined with depth profiling provides insight in the dynamic behavior of olivine under relevant conditions. Iron enrichment at the surface is observed; oxidized olivine has an iron rich surface layer of 400 nm. The increased iron concentration is particularly pronounced at the outermost surface. Upon subsequent reduction, the iron quickly redistributes in the olivine towards the original, homogeneous distribution. This chapter shows that oxygen transport should be taken into account when olivine is evaluated as a catalyst for indirect biomass gasification. Furthermore, both oxygen transport and catalytic properties are heavily dependent on the iron phases present in the material, which in turn depend on the gas environment.

To meet the increasing demand for renewable, CO_2-neutral energy, biomass (in particular waste products) can be used for the production of such fuels as hydrogen, synthetic natural gas or Fischer-Tropsch diesel [1, 2]. Conversion of biomass to fuels can be performed using the gasification process as an initial step in the conversion [3, 4]. The resulting primary products CO, H_2, CO_2 and CH_4 can easily be used in the present infrastructure. Moreover, technology for converting CO and H_2 into conventional fuels, such as diesel, is already at hand [5]. The endothermic gasification process is sustained by allowing partial combustion of the biomass, usually using air. If the heat required for the endothermic gasification is not supplied by partial combustion in the gasifier section, but instead comes from a separate combustion step, which may be integrated in the gasification system, one speaks of indirect gasification. The main advantages of indirect gasification are the higher heating value of the produced gas, no N_2 contamination of the product gas and that a major part of the CO_2 produced in the process is separated from the product gases, allowing for sequestration.

In a typical indirect gasification system, a bed material is circulated between an oxidation reactor and a gasification reactor, coupled together. In the latter, biomass reacts with steam and is converted to a gas mixture consisting mainly of methane, synthesis gas and CO_2. The bed material, together with the unconverted biomass fractions, tar and char, are fed into the oxidation reactor, to heat up the bed material. The hot bed material subsequently enters into the gasification zone to provide the heat, necessary for gasification. In addition to the main product gases, the gasification process always results in tar formation due to incomplete decomposition of the biomass. Tars decrease process efficiency and can cause fouling of downstream equipment. This constitutes a major obstacle in the way to large scale commercialization of the technique.

Tar in the product gas can be decreased by using a reactive bed material [6, 7, 8, 9, 10]. A widely used and investigated bed material is the naturally occurring mineral olivine $((Mg,Fe)_2SiO_4)$ [11, 12, 13, 14], in which iron is the catalytically active component for tar conversion [15, 16, 17, 18,

19]. Olivine is, however, not a stable material under process conditions, relevant for biomass gasification [14, 20]. It has been shown that iron in olivine is highly mobile under alternating oxidizing and reducing environments [12]; iron enrichment at the surface is observed upon oxidation, whereas a decreased content is seen upon reduction [21]. Furthermore, the iron in olivine is oxidized in the oxidation zone and reduced in the gasification zone, and is thereby able to transport oxygen to the gasification zone. Oxygen-transport lowers the necessary amount of steam for the gasification and increases tar degradation and fuel conversion [16, 22], but it also (unwantedly) increases the CO_2 content in the gasification zone.

This chapter focuses on the role of iron in the chemical looping process. When olivine is used as a circulating bed material, it is sequentially exposed to different gas environments on time scales from a few seconds to several minutes. Changes in the gas environment influence the phase composition of olivine in general, and the surface concentration and oxidation state of iron in particular. The dynamics of these effects have not been well documented yet. The aim of this chapter is to clarify the time dependent changes in olivine, (and especially the Fe-components contained therein) in rapidly changing, yet well-defined, chemical environments.

Mössbauer spectroscopy was used to determine the distribution of different iron species in olivine after oxidation and reduction treatments. Furthermore, Thermo Gravimetric Analysis (TGA) is used as a valuable characterization tool to quantify oxygen transport of olivine. To obtain detailed information on the dynamic behavior of iron at the surface and in the sub-surface layers under oxidizing and reducing conditions, X-ray Photoelectron Spectroscopy (XPS) was used in combination with depth profiling.

4.2 EXPERIMENTAL

4.2.1 *Catalyst Material and Treatments*

For all experiments, natural olivine from Magnolithe GmbH was used. A 3 h, 1600 °C calcination in air was performed by the mineral supplier

to improve its mechanical properties. The grain size during this pre-calcination was on the order of 10 mm. The composition of this olivine is well-known and extensively documented [7, 12, 13]. The iron content of the olivine sample used in this study was determined by ICP-AES to be 6.3 wt.%.

Prior to experiments, the olivine was grinded to a powder with grain sizes of several micrometers, as estimated from scanning electron microscopy (SEM) images. The olivine powder has a specific surface area of 0.53 m^2/g [23]. This grinded olivine will be denoted as "untreated" in this chapter.

The grinded olivine powders were treated in a quartz tube flow reactor. Oxidation (20 vol.% O_2 in Ar) and reduction (pure H_2) treatments were applied at 750 °C. Total gas flows were set to 200 mL/min. In all experiments, the samples were first heated to 750 °C under pure Ar flow. At this temperature, the gas flow was switched to the reactive gas mixtures for a specified time. After treatment, the gas mixture was switched back to Ar and the reactor was quickly cooled to room temperature.

4.2.2 *Mössbauer Spectroscopy*

Transmission ^{57}Fe Mössbauer spectra were collected at room temperature with a conventional constant-acceleration spectrometer using a ^{57}Co(Rh) source. Velocity calibration was carried out using an α-Fe foil. The Mössbauer spectra were fitted using the Mosswinn 3.0i program [24].

4.2.3 *Thermogravimetric Analysis*

Thermogravimetric Analysis (TGA) is a commonly used technique for studying reactive gas-solid systems. For measurements, the grinded, untreated olivine sample (200 mg) was placed in a porous quartz glass sample holder, connected by a platinum wire to a Sartorius 4406 balance, which measured the mass change of the sample during treatment. Gas treatments (oxidation (air, 8 mL/min) and reduction (30% H_2/N_2, 8 mL/min)) were applied at 750 °C in a home-built set-up, which is described in more detail elsewhere [25]. In between the oxidation and

reduction treatment, the system was flushed with N_2 for one minute to prevent direct contact between H_2 and O_2.

4.2.4 *X-ray Photoelectron Spectroscopy*

In this chapter, X-ray Photoelectron Spectroscopy (XPS) was combined with depth profiling. An ion gun was used to etch the sample's surface for a period of time before being turned off while XPS spectra were measured. Each etch step exposes a new surface and, by evaluating the measured XPS spectra, the elemental concentrations at that specific surface could be determined. The objective of these experiments was to investigate the trend in the atomic concentration values as a function of etch-time, or sample depth.

Olivine powder samples were supported on conductive carbon tape. XPS spectra were recorded using a Thermo Scientific K-Alpha spectrometer equipped with a monochromatic small-spot X-ray source and a $180\,^\circ$ double focusing hemispherical analyzer with a 128-channel detector. Spectra were obtained using an aluminum anode (Al Kα, 1486.6 eV) operating at 72 W and a spot size of 400 µm.

Region scans were measured at a constant pass energy of 50 eV. The background pressure was 2×10^{-8} mbar and during measurement 3×10^{-7} mbar argon, because of the charge compensation dual beam source.

Sputtering for depth profiling was done with an Ar^+ ion beam energy of 2000 eV at medium current (12 µA). The ion gun was used for 120 s for each etch step, corresponding to a total depth per etch level of 37.2 nm for a Ta_2O_5 reference.

All spectral positions were adjusted to the Si 2s peak of olivine at 153 eV [26] and analysis and quantification of the measurements were performed using the CasaXPS software, using the Fe 3p, Mg 2p, Si 2p, C 1s and O 1s regions.

4.3.1   *Mössbauer Spectroscopy*

Mössbauer spectroscopy was used to quantify the changes in the iron (oxidation) state of the olivine upon oxidizing and reducing treatments. The spectra are presented in figure 4.1. The detailed fitting parameters and spectral contribution of the different iron species are presented in table 4.1.
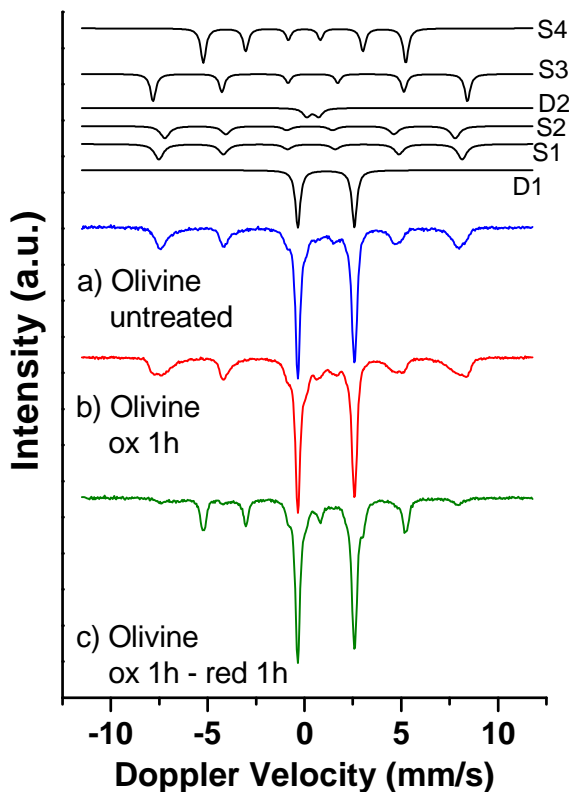
Figure 4.1: [57]Fe Mössbauer spectra of the as received, untreated olivine (a), olivine which has been oxidized for 1 h (b) and olivine which has first been oxidized for 1 h and then reduced for 1 h (c). Subspectra of different components are indicated at the top and the nomenclature is explained in table 4.1

Table 4.1: Mössbauer parameters of the olivine samples, obtained by fitting

	IS (mm/s)	QS (mm/s)	Hyperfine field (T)	Γ (mm/s)	Phase	Spectral contribution
Olivine untreated	1.12	2.92	–	0.30	Fe^{2+} (Olivine)	56% (D1)
	0.33	0	48.6	0.56	Fe^{3+} (Oct-$MgFe_2O_4$)	22% (S1)
	0.28	0	46.5	0.56	Fe^{3+} (Tet-$MgFe_2O_4$)	17% (S2)
	0.42	0.62	–	0.48	Fe^{3+} (γ-Fe_2O_3)	5% (D2)
Olivine ox 1h	1.12	2.92	–	0.30	Fe^{2+} (Olivine)	49% (D1)
	0.34	0	47.8	0.61	Fe^{3+} (Oct-$MgFe_2O_4$)	20% (S1)
	0.29	0	44.7	0.61	Fe^{3+} (Tet-$MgFe_2O_4$)	12% (S2)
	0.42	0.66	–	0.51	Fe^{3+} (γ-Fe_2O_3)	9% (D2)
	0.37	-0.14	50.4	0.35	Fe^{3+} (α-Fe_2O_3)	10% (S3)
Olivine ox 1h - red 1h	1.12	2.93	–	0.30	Fe^{2+} (Olivine)	56% (D1)
	0.46	0.70	–	0.43	Fe^{3+} (γ-Fe_2O_3)	5% (D2)
	0.37	-0.12	47.2	0.90	Fe^{3+} (α-Fe_2O_3)	12% (S3)
	0	0	32.4	0.33	Fe^{0} (metallic)	27% (S4)

IS: Isomer shift, QS: Quadropole splitting, Γ: Linewidth, S: Sextuplet and D: Doublet

Fitting of the spectra in Fig. 4.1 required the use of two doublets and four sextuplets. The two doublets are attributed to Fe^{2+} in the olivine phase (D1) and Fe^{3+} in superparamagnetic hematite (D2), respectively [20]. Of the four sextuplets, the first two (S1 and S2) are identified as belonging to Fe^{3+} in octahedral and tetrahedral sites of the spinel structure of magnesioferrite ($MgFe_2O_4$) [12, 27]. Sextuplet 3 can be attributed to hematite and the fourth sextuplet corresponds to metallic Fe.

The dominant contribution (56%) in the spectrum of the untreated olivine sample is a doublet with an isomer shift (IS) of 1.12 mm/s and a quadrupole splitting (QS) of 2.92 mm/s, attributed to Fe^{2+} in the olivine structure [13]. About 40% of the Fe atoms are present as two magnetic sextuplets (S1 and S2) that can be attributed to Fe^{3+} in octahedral and tetrahedral sites of the spinel structure of magnesioferrite ($MgFe_2O_4$) or Fe_3O_4 [12, 27]. A small contribution (5%) of a doublet with IS = 0.42 mm/s, assigned to superparamagnetic maghemite (γ-Fe_2O_3), is also observed. This Fe^{3+}-phase is known to form from the olivine structure, when olivine is oxidized in air in the range of 600–900 °C [20].

After the oxidation treatment at 750 °C for 1 h (Fig. 4.1b), more than half (51%) of the iron, is present in the form of free iron-oxides. 10% of the Fe atoms are present as a sextuplet with IS = 0.37 mm/s, QS = –0.14 mm/s and H (Hyperfine field) = 50.4 T, values corresponding well with those reported for Fe^{3+} in hematite (α-Fe_2O_3) [10]. The spectral contribution of the doublet, originating from paramagnetic hematite increases slightly.

After subsequent reduction (Fig. 4.1c), the dominating change is that 27% of the Fe is reduced to metallic Fe^0. It is also evident that parts of the Fe^{3+} species are reintegrated in the olivine structure as Fe^{2+}, the initial olivine spectrum being recovered. The two sextuplets, originating from the magnesioferrite, have disappeared. The remaining Fe^{3+} magnetic contribution can at least partially be assigned to hematite, while the presence of remnant magnesioferrite structures cannot be ruled out.
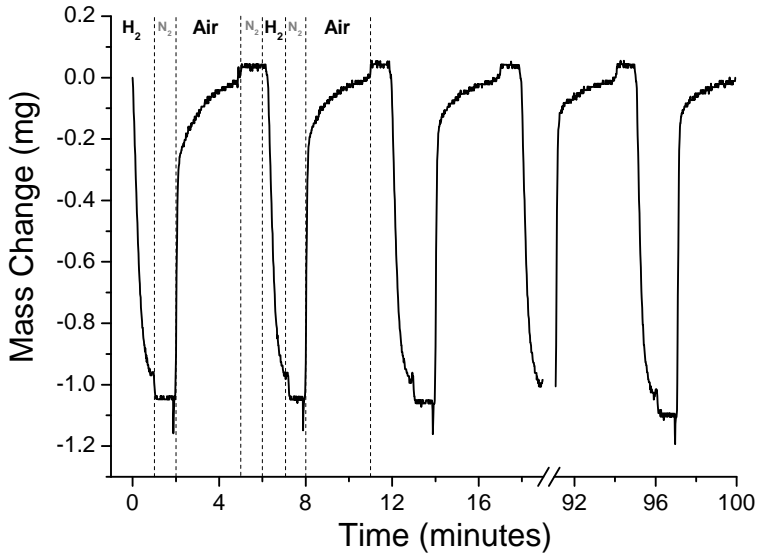
Figure 4.2: Mass change of an 1 h pre-oxidized olivine sample (200 mg) during continous oxidation (Air, 180 s) and reduction (30% H_2/He, 60 s) cycles at 750 °C, with intermediate N_2 flush

4.3.2 *Thermogravimetric Analysis*

Figure 4.2 shows the results of the Thermogravimetric Analysis (TGA) of an olivine sample under conditions simulating circulation between a gasification zone (reducing conditions) and an oxidation zone (oxidizing conditions) of an indirect gasification reactor. Oxidation and reduction times were chosen as 180 s and 60 s, respectively, to represent the conditions in an indirect gasifier with a riser reactor as the gasification zone and a bubbling fluidized bed as the oxidation zone, as applied in the ECN MILENA process [28].

At time t=0 min, the olivine was already oxidized in-situ for 1 h at 750 °C. When the gas-environment was switched from oxidizing to reducing conditions, the mass of the sample decreased with 1 mg. After 60 s, the gas environment was switched back to oxidizing conditions and the mass of the sample reached its initial value after 180 s. In total 20 oxidation/reduction cycles were done, and the weight loss showed less

than 2% difference during these 20 cycles. The apparent change in weight during the N_2 flush is a result of fluctuations in the gas flow-rate and density and does thus not correspond to any real change in weight of the sample material. The spikes just before and after flushing are also due to the switching of gas flows. This part of the experimental cycle is therefore not considered in the analysis.

The mass change during each cycle is a measure for oxygen-transport. Since this change is 1.0 mg in each cycle and the amount of sample is 200 mg, the oxygen transport under these conditions amounts to 0.5 wt.% of the bed material.

The mass changes during oxidation and reduction can be divided into two separate processes; 1) a very fast process, where 80% of the total mass change during the treatment is realized in just 5 seconds and 2) a slower, converging change of the mass with time, until the respective treatment is ended.

4.3.3   *X-ray Photoelectron Spectroscopy*

To study the composition of the outermost layers of olivine, XPS has been used in combination with depth profiling. Although XPS is a surface sensitive technique, which probes the first few nanometers of the sample, a depth profile can be obtained by combining a sequence of ion gun etch cycles with intermediate XPS analysis of the current surface.

Fig. 4.3 shows the depth profile of the untreated olivine sample. Apart from the elements present in olivine, Fe, Mg, Si and O, a significant amount of carbon is detected at the outer surface (etch level = 0). This is due to carbonaceous contaminations, deposited on the sample during sample transfer under ambient conditions, which are frequently measured by XPS. The surface carbon is largely removed during the first ion gun etch. This results in an increase of the concentration of all other elements, indicating that the carbon was homogeneously distributed on the surface of the olivine. After further etching, the concentrations do not change significantly, which shows that the elemental composition of the untreated olivine is homogeneous as a function of sample depth.
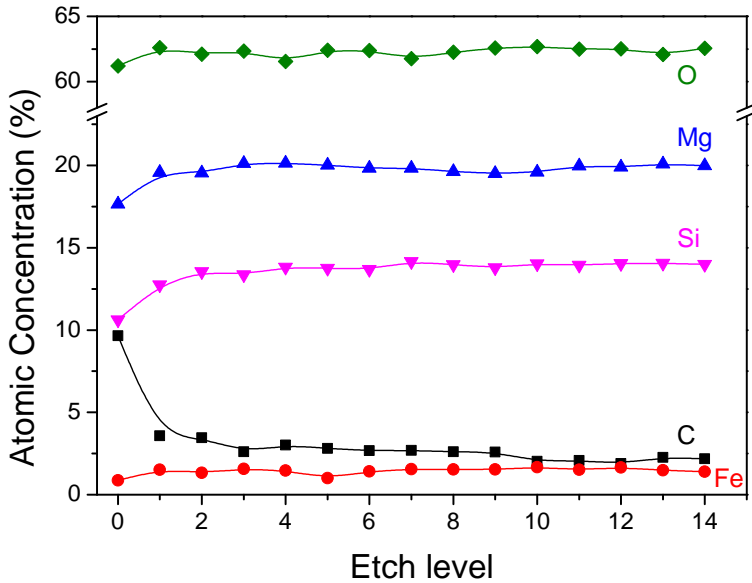
Figure 4.3: Atomic concentration of the elements present in untreated olivine, as a function of sample depth. Each etch level corresponds to approximately 35 nm sample depth

Figure 4.4 shows the depth profiles of oxidized and oxidized-reduced olivine. The concentration of the elements, present in olivine, is shown as a function of the etch level. When olivine is oxidized, the iron concentration at the surface (etch level = 0) increases significantly. When olivine is subsequently reduced, the iron concentration decreases again, to similar values as in the untreated olivine. XPS depth profiling yields valuable information on the dynamics of these surface layers.

After oxidation treatments, the concentration of iron decreases with increasing etch time. This shows that the iron is not homogeneously distributed throughout the sample, but that the surface of the particles is richer in iron than the bulk. This iron enrichment is observed at two time scales; both for 1 min and 1 h of oxidation treatment. After oxidation for 1 hour (solid red lines), the concentration of iron at the outermost surface is increased to 5.8%. During several etching steps, the iron concentration decreases exponentially to a value of 2%. This corresponds to an iron rich
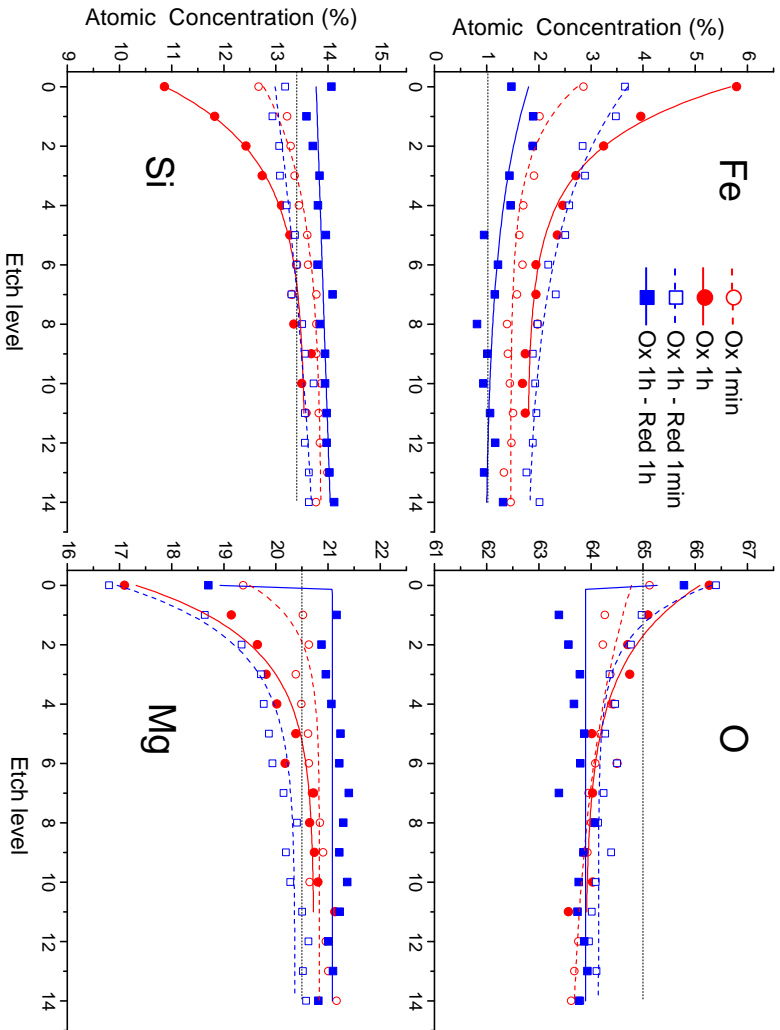
Figure 4.4: Depth profiles of the treated olivine samples. The concentration of the different elements is plotted as a function of sample depth. Treatments are as follows: 1 min oxidation, 1 h oxidation, 1 h oxidation, followed by reduction for 1 min and 1 h oxidation, followed by reduction for 1 h. The colored lines are exponential fits as a guide to the eye and the dotted lines denote the bulk concentration of the respective elements in untreated olivine. Each etch level corresponds to approximately 35 nm sample depth

layer of approximately 400 nm, where the iron concentration is twice as high as in the untreated olivine, using the etch-rates for a Ta_2O_5 reference to convert the sputtering time to distance.

When the oxidized olivine is reduced for 1 minute (dashed blue lines), the iron concentration at the surface decreases immediately to 3.6%. The depth profile shows that only the iron concentration close to the particle surface is affected by this short reduction. After three etching steps, the concentration resembles the respective iron concentration of the 1 h oxidized olivine. Longer reduction time (solid blue lines) results in a lower iron concentration, which is homogeneously distributed with respect to the sample depth. The amount of iron in these surface layers closely resembles the iron concentration at the surface of the untreated olivine.

Whereas the iron concentration at the surface increases upon oxidation, decreasing concentrations of Mg and Si are observed. The depth profiles show increasing concentrations of the latter two elements with prolonged etching. At increased sample depth, the Mg and Si concentrations are slightly larger compared to their bulk concentrations in the untreated olivine, indicated by the black dashed lines. An interesting observation is that the concentrations of Fe and Si in the depth profiles appear to be each other's mirror image. This holds true, to a lesser extent, for the Mg and O concentrations as well.

Another observation is the difference between Mg and Si concentrations in the pre-oxidized, 1 min reduced sample (dashed blue lines), compared to the 1 h oxidized sample (solid red lines). The depth profiles of both samples have similar Mg concentrations with respect to sample depth. On the other hand, the silicon depth profile for the one minute reduced sample looks markedly different from the 1 h oxidized one. After reduction of the pre-oxidized olivine for 1 min, the Si concentration at the surface is significantly higher than before this short reduction.

In other words, on the short time scale, Si is exchanged with Fe at the surface in the first stages of olivine reduction. In the longer run, Fe exchanges with Mg as well. The depth profiles of the pre-oxidized, 1 h reduced sample show a significantly decreased surface concentration of
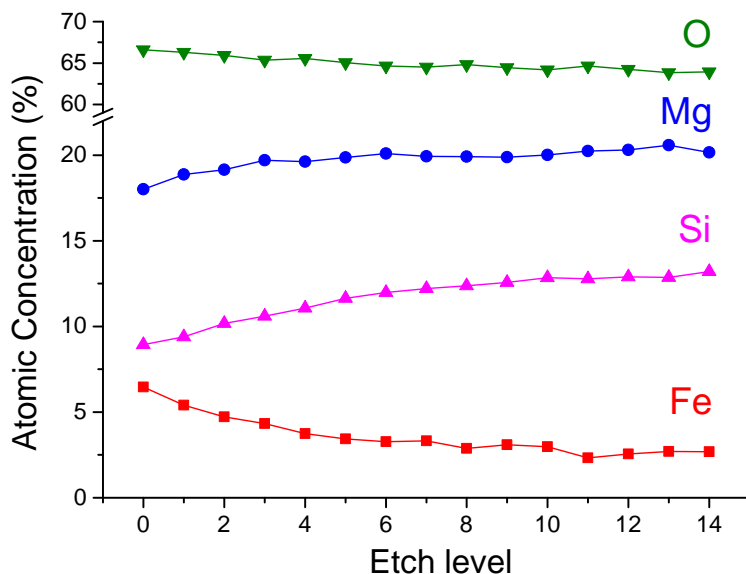
Figure 4.5: Atomic concentration of the elements present in olivine, as a function of sample depth. The sample has been oxidized for 1h and subsequently exposed to oxidation (180 s) and reduction (60 s) treatments in the TGA at 750 °C (20 cycles in total). Each etch level corresponds to approximately 35 nm sample depth

Mg and an increased concentration of O, compared to the concentrations at increased etching time.

An additional XPS depth profile study was carried out (Fig. 4.5) for a 1h pre-oxidized olivine sample, after 20 oxidation-reduction cycles in the TGA, to check if the trends, presented in Fig. 4.4, are influenced by the oxidation-reduction cycles. The sample was cooled down after the 21st oxidation treatment. The iron surface concentration was only marginally higher (6.5%), compared to the 1 h oxidized olivine (5.8%). All other elements also showed comparable distributions. This demonstrates that, although the sample which has undergone repeated redox cycles was exposed to air for an additional hour during the TGA measurement, the trends for the 1h oxidized olivine, shown in Figure 4.4, are also present when olivine has undergone repeated redox cycles.

4.4 DISCUSSION

The results presented in this chapter provide a great deal of information about changes in the phase composition of olivine, treated in different gas environments. The combination of these three techniques, Mössbauer spectroscopy, TGA and XPS depth profiling gives unique insight into phase changes, both in space and time. In particular, the former two techniques give quantitative insight into the phase changes, whereas the latter provides information about sample homogeneity and spatial distribution of the elements.

4.4.1 *Oxygen-Transport*

The TGA measurement (Fig. 4.2) can be used to determine the fraction of iron, actively participating in oxidation and reduction upon exposure to different gases. This determines the materials capability of transferring oxygen from the oxidation zone to the reduction zone. It is assumed that the near surface iron species, participating in these reactions, are Fe_2O_3 and Fe^0. The assumption is based both on the results presented here, the results of chapter 3 and on previously reported XPS, XRD and Mössbauer analysis [10, 12, 23]. Although it is clear that full conversion of Fe_2O_3 to Fe^0 is not expected in a real system, using this assumption, a lower limit to the fraction of Fe that participates in the redox reactions can be determined. Moreover, it is realized that pure H_2 does not represent an industrial gas environment. However, the product gas of industrial scale indirect gasifiers consists of 40% H_2 and 25% CO [14], which has a very high reducing power as well. H_2 was chosen for this model study, because reduction by gases containing carbon gives unwanted side-effects, e.g. carbon deposition.

The total mass change in each reduction/oxidation step is 1.0 mg. Since the used gases are free of contaminants, it is assumed that only addition or removal of oxygen causes this mass change. For the Fe_2O_3/Fe^0 redox couple, 1.5 moles of atomic oxygen react with each mole of free Fe, or using the respective molar masses, 2.33 mg Fe for 1.0 mg of O. The absolute amount of iron in the sample is 12.6 mg (200 mg sample with

6.3 wt.% Fe). With these numbers, it can be calculated that, under these conditions, 18.5% of all the iron present in olivine is participating is this redox process.

4.4.2   *Reversibility of Phase Changes*

Results obtained by Mössbauer spectroscopy (Fig. 4.1, Table 4.1) show that almost half (44%) of the iron in the (in this study) untreated olivine is already driven out of the olivine matrix, through the pre-treatment applied by the mineral supplier. This free iron phase exists predominantly as the Fe^{3+} spinel structure of $MgFe_2O_4$. Despite the relatively low oxidation temperature of 750 °C, applied in this study, another 7% of Fe is extracted from the olivine matrix during oxidation treatment. A decreased spectral contribution of the spinel phase after oxidation is also observed. A simultaneous increase in the hematite phase indicates a conversion of the olivine and spinel phases to hematite.

Previous research [12] shows that exclusion of Fe from olivine is significant at temperatures above 1100 °C. Taken into account that the mineral supplier already treated this olivine at 1600 °C for several hours, it may seem counter intuitive that additional Fe exclusion is observed at 750 °C. The 1600 °C pre-treatment was however done prior to grinding. During grinding, grain boundaries break up and fresh surfaces are created. These new surfaces are in direct contact with the surrounding gas environment. The observed phenomenon can thus be thought of as a surface effect.

Another important observation is that the extraction of iron out of the olivine matrix during oxidation is a reversible process; after reduction, the spectral contribution of the olivine phase is the same, 56%, as it was in the untreated material. However, the hematite phases and a significant amount of the iron present as spinel phase are converted into metallic Fe^0 during reduction. This shows that there is only a partial reversibility of the phase composition upon reduction and that the material does not return to the original, untreated state.

4.4.3   Sample Homogeneity

The elemental concentrations in the untreated olivine, as a function of sample depth, as observed in XPS depth profiling (Fig. 4.3), show a homogeneous distribution of the constituting elements. This implies that the relative fraction of olivine and magnesioferrite is the same, throughout the bulk of the sample. Hence, the complete disappearance of the magnesioferrite upon reduction, as observed in Mössbauer spectroscopy, suggests that the phase changes are significant. The changes are not only happening at the surface, but also in the bulk of the material.

The observation that the untreated material is homogeneous, might at first glance seem to be in contradiction with chapter 3, showing that the olivine is better regarded as a FeOx-catalyst, supported on Mg_2SiO_4 and amorphous SiO_2, than as a homogeneous material. Different domains in olivine should indeed show different elemental concentrations up to the meso scale (1–100 μm). However, the XPS measurements are performed with a circular analysis area with a diameter of 400 μm. All elemental concentrations are averaged out over this area, resulting in homogeneous concentrations of the elements on this macro scale. However, after oxidation and reduction treatments, homogeneity is no longer observed in the direction perpendicular to the surface. It should be noted that in this direction the spatial resolution is not limited by the spot size but by the Ar-etching process. In the experiments presented here, each etch step is approximately 35 nm.

4.4.4   Redox Kinetics and Diffusion

From the TGA data, it is evident that the mass changes during oxidation and reduction can be divided into two separate processes; one fast, on the timescale of a few seconds and a slower, continuous process, on the timescale of several minutes. The results from XPS-depth profiling (Fig. 4.4) show a similar division into a fast and a slow process. The change in elemental composition of the surface layers, as a response to oxidizing and reducing gas treatments at 750 °C, differs both quantitatively and qualitatively for 1 min and 1 h treatments.

Short Term

The most obvious effect of the shorter treatments is a surface enrichment and depletion of Fe. After the oxidizing treatment, more Fe is observed at the surface, whereas a subsequent reduction quickly reduces the amount of surface Fe. After the 1 min treatments, only the upper surface layer of the material is affected, whereas changes in the bulk are insignificant. Fe increases/decreases predominantly at the expense of Si. It is also observed that Fe species at the surface change oxidation state, from fully oxidized Fe^{3+} to largely reduced Fe^{2+}/Fe^0 state already after 1 min of reduction, in agreement with chapter 3.

These observations, together with the fast mass changes observed with TGA, suggest oxidation/reduction of surface iron, excluded from Si-rich areas in the olivine. Iron oxide particles, present at the surface of the material, are in direct contact with the gas atmosphere and can therefore respond quickly to changes in the gas environment. The formation of iron oxide crystallites, supported on a Si-rich background, would show as increased presence of Fe at the expense of Si. When these iron oxide crystallites are reduced, their size will quickly decrease, thereby re-exposing Si at the surface.

Although the gas composition in a real gasification system will be less reducing than the gas used in the TGA measurements, these results show that olivine, and especially iron, is a very dynamic material on the time scale of seconds. With the changing oxidation state of iron, its catalytic properties change as well. Therefore, different reactions will be catalyzed, depending on the catalysts residence time in the gasification zone. In particular, fast reduction of iron to its metallic state is beneficial for the removal of tars from the producer gas, since metallic iron catalyzes tar-cracking at process conditions, relevant for biomass gasification [15, 18].

Furthermore, the fast iron enrichment at fresh surfaces is an important observation in view of the use of olivine in fluidized-bed reactors. During use, the grain sizes will decrease, as a result of attrition, and new, fresh surfaces will be exposed to the gas environment. This attrition could actually result in a more active olivine, since more iron is quickly extracted from the olivine matrix to the surface when smaller particles are formed. The catalytically active surface area is hereby increased. Indeed, Rapagna

et al. reported an increasing H_2-concentration in the product-gas as a function of time on stream, when untreated olivine was used as bed material [6], although it was not clear from their study whether this increase could be attributed to increasing iron surface area.

Long Term

The XPS depth profiles show that changes in composition are largest at the surface, both in the long term and in the short term perspective. However, the long term treatments influence the elemental composition in the entire probed depth of almost ~400 nm. After oxidation for 1 h, the iron concentration increases exponentially from the bulk to the surface of the particle. When the 1 h oxidized olivine is subsequently reduced, the iron concentration in the upper layer decreases. This results in a homogeneous iron concentration in the upper layers after 1 h of reduction, in line with the bulk concentration of the untreated olivine. In the long term, Fe increases/decreases at the expense of both Si and Mg. In addition, an increase/decrease in subsurface oxygen can be observed, inversely correlated to the Mg content.

Olivine is considered to be a non-porous material [7, 12, 21]. Therefore, reduction or oxidation of material inside the particles is likely to be diffusion limited, since gases cannot easily penetrate the solid particles. However, the complete conversion of the spinel $MgFe_2O_4$ upon reduction in H_2, together with the homogeneity of the untreated material, as observed with Mössbauer spectroscopy and XPS, respectively, suggest that the bulk of the material is affected as well as the surface. It is therefore likely that the slower changes, observed both in TGA and XPS, are due to diffusion limited reduction and oxidation reactions in the bulk of the material.

A plausible explanation for the ongoing bulk phase changes, in spite of the non-porous nature of olivine, is the formation of cracks, caused by rapid morphological changes. Swierczynski et al. have observed that long, rodlike iron oxide precipitates are formed inside the olivine particles upon oxidation [12]. When this iron oxide reduces, it creates a hollow pore, or crack, inside the particle. These cracks have diameters up to several micrometers and make it possible for gases to migrate in and out

of the particles. Moreover, Bleeker et al. have reported substantial internal self diffusion in iron oxide during continuous redox cycles, which seemed to speed up densification and internal sintering, causing cracks in the material [29].

The increase of Fe in the subsurface layer suggests a net migration of Fe towards the surface from the bulk of the material, presumably through defects in the crystal structure and/or at the surfaces of cracks and imperfections in the material, as discussed above. The simultaneous decrease in both Mg and Si content suggests that on the long term, Fe migrates through both Fe- and Mg-rich domains of the material.

A tentative explanation of the higher surface content of iron observed during oxidizing than during reducing conditions can be found by considering the thermodynamics of the system. Calculations show that Fe_3O_4, SiO_2, pyroxene and olivine are expected after treatment in oxidizing environments [30]. The same phases are expected under reducing conditions, with the exception that metallic Fe is expected instead of Fe_3O_4. Furthermore, the surface free energy of iron oxide is lower than that of metallic Fe [31, 32]. Therefore, a larger energy gain is associated with bringing Fe to the surface during oxidizing conditions (as iron oxide) than during reduction (as metallic Fe). More Fe is thus expected at the surface under oxidizing conditions, as observed.

An inverse correlation between O and Mg-content is also noted, especially at the outermost surface layer. This may be due to preferential oxidation/hydroxylation of Mg-rich domains in the material. Such an effect would help explaining the surprisingly low Mg surface content observed, both here and in chapter 3.

4.4.5   *Surface Oxide Formation*

Finally, it should be noted that all measurements presented in this chapter were done ex-situ. The samples were exposed to air upon transfer from the reaction chamber to each of the used analysis instruments. This is particularly important for the reduced samples. Even if these were completely reduced to Fe^0 after the treatment, surface re-oxidation is to be expected in air at room temperature. It is therefore likely that, at least

part of the Fe^{3+}, observed in the Mössbauer spectrum of the reduced sample, is due to an amorphous surface oxide. A surface oxide is indeed observed in the XPS-spectra of iron, even for the reduced samples. The iron in the depth profiles of the reduced samples shows an oxide at the outer surface layer, but the iron in the inner layers is largely metallic. Surface oxides can also be seen from the sharp increase in the oxygen concentration at the surface. The excess oxygen is removed after one etching step, indicating that the surface oxide layer is thinner than 35 nm.

Analysis of the oxidation state of Fe-compounds from the depth profiles indicates sub-surface reduction of Fe_2O_3 to Fe_3O_4 and even metallic Fe, which, for the oxidized samples, is in contradiction with the Mössbauer measurements. However, it is known that, during sputtering experiments, the oxidation state of iron decreases with increasing etching time [33, 34], due to preferential sputtering of the oxygen atoms. Therefore, analysis of the Fe oxidation states from these measurements is not discussed in this chapter.

4.5 CONCLUSION

Various characterization tools were used in order to investigate the capability of Austrian olivine to transport oxygen. This material is frequently used as a reactive bed material in indirect biomass gasification.

Mössbauer spectroscopy confirmed that in the investigated Austrian olivine almost half of the iron exists in the form of free iron oxides. Oxidation at 750 °C increases the content of free iron oxide phases from 44 to 51%. Part of the iron oxide phases reduce to metallic iron upon reduction, but a small fraction is reintegrated back into the Fe^{2+} phase of olivine.

TGA showed that olivine can transport 0.5 wt.% of oxygen and that the material is oxidized and reduced on two distinctly different time scales. The fast process is responsible for 80% of the mass changes and is attributed to surface oxidation/reduction. It was estimated that 18.5% of all the iron present in olivine contributes to the oxygen transport on time scales of one to several minutes.

XPS depth profiling showed that upon oxidation, an iron rich surface layer of at least ~400 nm thick is formed. This iron enrichment is a reversible process; when oxidized olivine is reduced, the iron surface concentration decreases to similar values, as in the untreated olivine. In similarity with the TGA results, elemental changes in the near surface region occur on two time scales. The fast process of Fe enrichment at the expense of Si is attributed to the oxidation of near surface Fe. The slower, sub-surface process of Fe enrichment at the expense of Si and Mg is attributed to migration of iron through the sample.

Based on these results, it can be concluded that olivine transports a significant amount of oxygen on times scales, relevant for industrial processes. Changing process conditions influence the iron concentration at the surface and sub-surface layers. Hence, the oxygen transport capability, as well as the catalytic properties of olivine are heavily dependent on the process conditions, as these conditions determine the composition of olivine, especially in the near surface region.

REFERENCES

[1] G. W. Huber, S. Iborra and A. Corma, Chemical Reviews 106 (2006) 4044–4098.

[2] A. V. Bridgwater, Biomass and Bioenergy 38 (2012) 68–94.

[3] D. A. Bulushev and J. R. H. Ross, Catalysis Today 171 (2011) 1–13.

[4] N. L. Panwar, R. Kothari and V. V. Tyagi, Renewable and Sustainable Energy Reviews 16 (2012) 1801–1816.

[5] T. Damartzis and A. Zabaniotou, Renewable and Sustainable Energy Reviews 15 (2011) 366–378.

[6] S. Rapagna, N. Jand, A. Kiennemann and P. U. Foscolo, Biomass and Bioenergy 19 (2000) 187–197.

[7] J. N. Kuhn, Z. Zhao, L. G. Felix, R. B. Slimane, C. W. Choi and U. S. Ozkan, Applied Catalysis B: Environmental 81 (2008) 14–26.

[8] F. Miccio, B. Piriou, G. Ruoppolo and R. Chirone, Chemical Engineering Journal 154 (2009) 369–374.

[9] S. Koppatz, C. Pfeifer and H. Hofbauer, Chemical Engineering Journal 175 (2011) 468–483.

[10] M. Virginie, J. Adanez, C. Courson, L. F. de Diego, F. Garcia-Labiano, D. Niznansky, A. Kiennemann, P. Gayan and A. Abad, Applied Catalysis B: Environmental 121-122 (2012) 214–222.

[11] D. Sutton, B. Kelleher and J. R. H. Ross, Fuel Processing Technology 73 (2001) 155–173.

[12] D. Swierczynski, C. Courson, L. Bedel, A. Kiennemann and S. Vilminot, Chemistry of Materials 18 (2006) 897–905.

[13] M. Virginie, C. Courson, D. Niznansky, N. Chaoui and A. Kiennemann, Applied Catalysis B: Environmental 101 (2010) 90–100.

[14] F. Kirnbauer, V. Wilk, H. Kitzler, S. Kern and H. Hofbauer, Fuel 95 (2012) 553–562.

[15] T. Nordgreen, T. Liliedahl and K. Sjöström, Fuel 85 (2006) 689–694.

[16] J. Pecho, T. J. Schildhauer, M. Sturzenegger, S. Biollaz and A. Wokaun, Chemical Engineering Science 63 (2008) 2465–2476.

[17] S. Rapagna , M. Virginie, K. Gallucci, C. Courson, M. D. Marcello, A. Kiennemann and P. U. Foscolo, Catalysis Today 176 (2011) 163–168.

[18] T. Nordgreen, V. Nemanova, K. Engvall and K. Sjöström, Fuel 95 (2012) 71–78.

[19] A. Sarvaramini and F. Larachi, Fuel 97 (2012) 741–750.

[20] K. Barcova, M. Mashlan, R. Zboril and P. Martinec, Journal of Radioanalytical and Nuclear Chemistry 255 (2003) 529–533.

[21] L. Devi, M. Craje, P. Thüne, K. J. Ptasinski and F. J. J. G. Janssen, Applied Catalysis A: General 294 (2005) 68–79.

[22] T. Pröll, K. Mayer, J. Bolhar-Nordenkampf, P. Kolbitsch, T. Mattisson, A. Lyngfelt and H. Hofbauer, Energy Procedia 1 (2009) 27–34.

[23] H. O. A. Fredriksson, R. J. Lancee, P. C. Thüne, H. J. Veringa and J. W. Niemantsverdriet, Applied Catalysis B: Environmental 130-131 (2013) 168–177.

[24] Z. Klencsár, Nuclear Instruments and Methods in Physics Research Section B: Beam Interactions with Materials and Atoms 129 (1997) 527–533.

[25] S. Noorman, F. Gallucci, M. van Sint Annaland and H. J. A. M. Kuipers, Industrial & Engineering Chemistry Research 49 (2010) 9720–9728.

[26] H. Seyama and M. Soma, J. Chem. Soc., Faraday Trans. 1 81 (1985) 485–495.

[27] G. Bond, K. C. Molloy and F. S. Stone, Solid State Ionics 101 (1997) 697–705.

[28] C. M. van der Meijden, *Development of the MILENA gasification technology for the production of Bio-SNG*, PhD Thesis, Eindhoven University of Technology, 2010.

[29] M. F. Bleeker, S. R. A. Kersten and H. J. Veringa, Catalysis Today 127 (2007) 278–290.

[30] U. Nitsan, J. Geophys. Res. 79 (1974) 706–711.

[31] X.-G. Wang, W. Weiss, S. K. Shaikhutdinov, M. Ritter, M. Petersen, F. Wagner, R. Schlögl and M. Scheffler, Phys. Rev. Lett. 81 (1998) 1038–1041.

[32] S. Hong, Current Applied Physics 3 (2003) 457–460.

[33] T. Yamashita and P. Hayes, Applied Surface Science 254 (2008) 2441–2449.

[34] D. S. Petrovic and D. Mandrino, Materials Characterization 62 (2011) 503–508.

5

Coating Formation and Influence on Reactivity

ABSTRACT

Formation of a coating layer on olivine, due to interaction of bed material with biomass ash, has been observed during biomass gasification in dual fluidized-bed gasifiers. This Ca-rich layer builds-up in time, increases tar conversion and enhances hydrogen production. The research described is this chapter focusses on the nature of this bed material coating and the influence of the coating on the reactivity of bed material is investigated.

Olivine, which was coated by calcium during continuous use as bed material in an indirect gasification system, was extensively characterized by SEM-EDS and XPS, and the WGS activity was tested in a fixed-bed reactor. SEM-EDS analysis showed that already after 30 h of biomass gasification, a surface layer, containing calcium and potassium, is formed on olivine. XPS depth profiling showed that this Ca-rich surface layer also contained carbonate species and is at least 0.5 micrometer thick.

A mechanism for the coating of the bed material is proposed, involving iron segregation to the surface during the first stages of use of olivine as a bed material. Ash compounds are incorporated in this surface layer, in which Fe is still mobile and K is able to penetrate deep into the particles, because of its volatility.

The WGS-activity of the coated material is almost a factor 5 higher than that of uncoated olivine. Biomass ash compounds were also found to be WGS active and are known to be active towards tar reduction as well.

5.1   INTRODUCTION

Biomass has received more and more attention over the recent years as a source of renewable, CO_2 neutral energy. Biomass can be converted to a broad range of fuels and chemicals in several different ways: biochemically via digestion or fermentation or thermochemically via torrefaction, pyrolysis or gasification [1]. Since gasification is an efficient technology for large-scale biomass conversion [2], it is often the technology of choice for the production of synthetic natural gas (SNG) or synthesis gas [3].

Because of the fuel flexibility for different kinds of biomass, fluidized-bed gasification is preferred for biomass [4, 5]. However, a major disadvantage of conventional biomass gasification is the high concentration of N_2 in the product gas, resulting from the partial combustion of biomass with air to produce heat, or the high cost of an air separation unit, when pure O_2 is used for the combustion. This can be avoided by using indirect fluidized-bed gasification [6]. ECN has developed the MILENA indirect gasification process, where gasification and combustion take place in separate chambers in the same reactor [7]. A circulating bed material is used to transport the heat from the combustion zone to the gasification zone. Although this approach avoids the problems associated with N_2, one of the main problems associated with biomass gasification still remains, namely the formation of tars.

To prevent problems caused by tar-formation during gasification, several active bed materials for tar reforming have been proposed, including the minerals dolomite (CaO-MgO) and olivine ($(Mg,Fe)_2SiO_4$) [8]. Although dolomite is generally considered to be more active towards tar reduction [9], it is soft and suffers from severe attrition during circulation between the combustion and gasification chambers. Olivine, which is less active, but much harder, is therefore a widely used bed material for catalytic cracking of tars in dual fluidized bed reactors [7, 10]. However, both process conditions and mineral properties are important for the performance of olivine in the gasification process. Both the elemental composition, addition of Fe and high temperature treatments influence the catalytic properties of this mineral [11, 12]. Moreover, olivine is not a

stable material under process conditions relevant for biomass gasification [13, 14, 15].

After extensive use of olivine in indirect biomass gasification reactors, Ca-rich coating formation has been observed [16, 17, 18], due to interaction of the bed material with biomass ash. It has been reported that this bed material coating increases tar conversion and enhances hydrogen production [19].

Furthermore, is has been shown that CaO itself can act as a catalyst during gasification of biomass as well [20]. Several studies have shown a catalytic effect of CaO towards tar reforming in fluidized-bed gasifiers [21, 22, 23].

If calcium-coated olivine is used as the bed material in indirect biomass gasification, the hydrogen concentration in product gas increases and the concentration of tars decreases [24, 19]. Moreover, Kern et al. showed that spent olivine with a coating layer containing calcium, was able to increase the CO conversion in the WGS reaction to around 38%, compared to only 2% for fresh olivine [25]. The similar activity of used olivine and CaO (despite a difference in CaO content) was attributed to the presence of potassium in the coating.

Potassium and other alkaline and alkaline earth metal compounds are regularly investigated as catalysts for biomass conversion [26, 27, 28] and show activity towards hydrogen production and tar reduction.

Calcium can be present both as CaO or as $CaCO_3$ and the former can react with CO_2 to form the latter via:

$$CaO(s) + CO_2(g) \rightleftarrows CaCO_3(s) \tag{5.1}$$

This CO_2 uptake can be utilized for the production of extra hydrogen via the water-gas shift (WGS) reaction:

$$CO + H_2O \rightleftarrows H_2 + CO_2 \tag{5.2}$$

The removal of CO_2 by CaO shifts the WGS equilibrium to the hydrogen side according Le Chatelier's principle. These properties of calcium oxide can be used for both CO_2 capture [29] and enhanced hydrogen production from biomass [30]. In a chemical looping process, CaO can be

regenerated by calcination of $CaCO_3$ in a different reactor. This calcium-based chemical looping can be applied to the indirect biomass gasification process, as described by Koppatz et al. [31] and Udomsirichakorn and Salam [32].

The aim of the research described in this chapter is to investigate the chemical composition of the coating layer, deposited on olivine during indirect biomass gasification, and the influence of the coating on the reactivity of the bed material with respect to enhanced hydrogen production via the WGS reaction. The chemical composition of the coating was studied by Scanning Electron Microscopy in combination with elemental mapping and X-ray Photoelectron Spectroscopy in combination with depth profiling. The activity of the coating towards the WGS reaction was tested in a fixed-bed reactor and the results were compared with olivine, which was not previously used during biomass gasification, and a sample of pure calcite (CaO). Since the coating is deposited on the bed material by interaction with ash from the biomass, a sample of ash from beechwood was tested for its WGS activity as well.

5.2   EXPERIMENTAL

5.2.1   *Materials*

Natural olivine from Magnolithe GmbH was used for all experiments. Untreated olivine refers to this olivine after a 3 h, 1600 °C calcination in air, which was performed by the mineral supplier to improve its mechanical properties. Subsequently, it was grinded down to a powder with particle diameters typically between 100 and 500 micrometer and a BET surface area of 0.18 m^2/g. The composition of this olivine is well-known and extensively documented [13, 15, 33].

Used olivine in this chapter refers to untreated Austrian olivine, which has been used for 30 h in a pilot plant by ECN [18]. The particle size of this sample had a broad distribution between 200 - 1000 micrometer and the BET surface area was 0.31 m^2/g.

Biomass ash is defined here as the residue after treatment of a beechwood sample (Rettenmaier) for 6 h in an H_2O/Ar (3 vol.%) flow at

800 °C. The ash content of this beechwood is 1.0 wt.% on dry basis [7]. The ash particles had a porous structure with sizes ranging from 1 to 50 micrometer.

CaO powder from Sigma Aldrich with particle diameters ranging from 10 - 50 micrometer was used without further modification.

5.2.2 *Characterization*

For X-ray Photoelectron Spectroscopy (XPS), samples were supported on conductive carbon tape and spectra were recorded using a Thermo Scientific K-Alpha spectrometer equipped with a monochromatic small-spot X-ray source and a 180° double focusing hemispherical analyzer with a 128-channel detector. Spectra were obtained using an aluminum anode (Al Kα, 1486.6 eV) operating at 72 W.

Survey scans were measured at a pass energy of 200 eV and region scans at a pass energy of 50 eV. The background pressure was 2 x 10^{-8} mbar and during measurement 3 x 10^{-7} mbar argon, because of the charge compensating dual beam source.

Etching for depth profiling was done with an Ar^+ ion beam energy of 2000 eV at medium current (12 μA). The ion gun was used for 120 s for each etch step, corresponding to a total depth per etch level of 37.2 nm for a Ta_2O_5 reference.

Analysis and quantification of the spectra were performed using the CasaXPS software version 2.3.16, using the Fe 3p, Mg 2p, Si 2p, C 1s, K 2p, Ca 2p, O 1s and Mn 2p regions.

For SEM-EDS analysis, the sample was embedded in a two-component resin (Struers EpoFix) and subsequently sanded and polished in the absence of water. The pictures were taken on a Hitachi SU-70 Field Emission SEM. The accelerating voltage was 15 kV and the working distance 15 mm. EDS analysis was done using an Oxford Instruments Type X-Max detector.

The SEM picture of the used olivine particles (Fig. 5.2) was taken using a FEI Quanta 3D FEG dual beam.

5.2.3   *Water-gas Shift Activity Measurements*

Water-gas shift (WGS) activity measurements were carried out in quartz tubular fixed-bed reactor with an 6 mm inner diameter. The sample (25 mg for each experiment) was kept in the middle of the reactor by quartz wool at both sides of the sample, resulting in a bed height of 2 - 4 mm. The sample temperature was controlled using a thermocouple close to the catalyst bed.

The reactor was heated to 500 °C (10 °C/min) in Ar (200 mL/min) and after the temperature of the bed reached 500 °C, the feed was switched to a 3/3/94 vol.% $CO/H_2O/Ar$ mixture (200 mL/min). The H_2O was added by passing the CO/Ar stream through a bubbler, containing deionized water and the water concentration was measured using a Mitchell instruments, MDM300 advanced dewpoint hygrometer.

The outlet gas composition was measured on-line using a Pfeiffer Vacuum THERMO^{Star} GSD 320 mass spectrometer. After 10 minutes, the activity was constant and the hydrogen production was determined as mass 2 divided by mass 40 (Ar) in the outlet gas stream, averaged over 20 measurement points in 10 s. Then, the temperature was increased by 100 °C (10 °C/min) and the activity was measured at 600, 700 and 800 °C in the same way.

5.3   RESULTS

5.3.1   *Nature of Bed Material Coating*

Figure 5.1 shows a backscatter SEM image of a cross-section of an olivine particle after 30 h of use as a bed material during biomass gasification. At the outer surface of the particle, a porous layer with a thickness of a few μm is visible, as well as cracks and inclusions inside the particle. This has been observed in previous studies and is attributed to the formation of a bed material coating due to the interaction of olivine with biomass ash particles [16, 17, 25].

Figure 5.2 shows a SEM picture of used olivine particles, where two types of surfaces are seen. On the left, one side of the particle has a
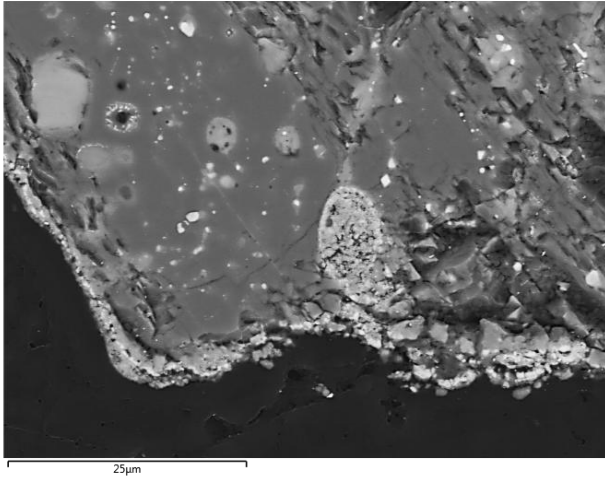
Figure 5.1: SEM image of the cross-section of an olivine particle, used for 30 h during indirect biomass gasification

smooth surface, whereas the surface at the top of the picture is covered with deposits, which have a porous structure. These deposits also appear at the surface of the particle at bottom right of the picture.
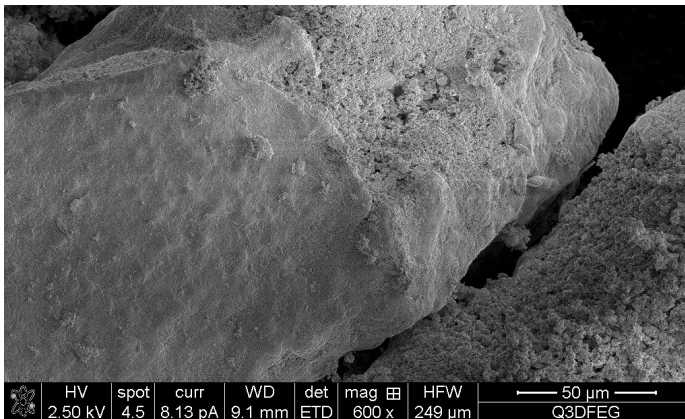
Figure 5.2: SEM image of used olivine particles
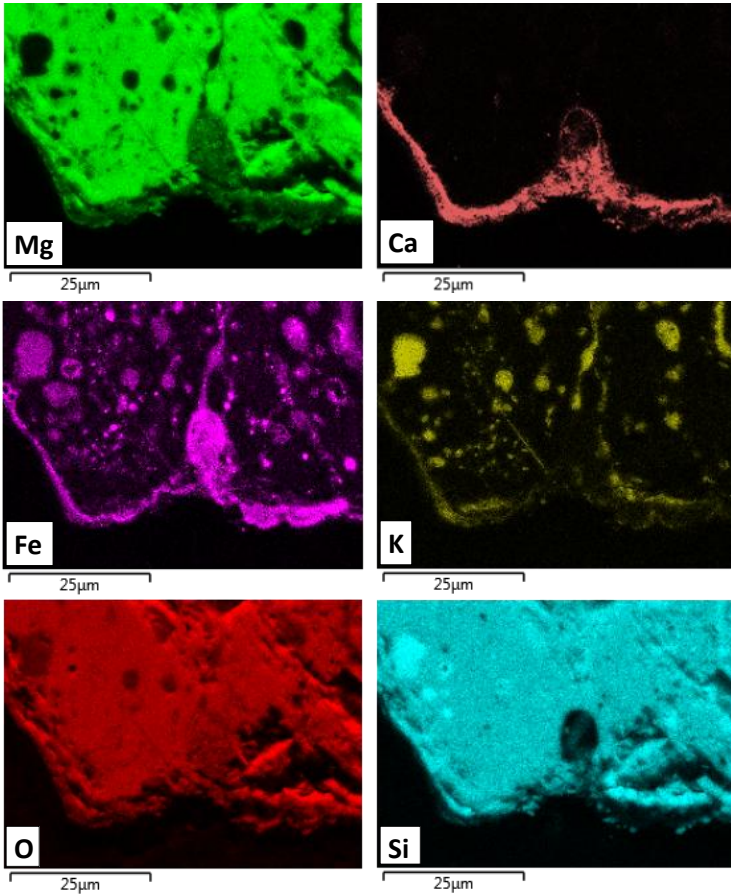
Figure 5.3: Elemental mapping of an used olivine particle by SEM-EDS

A more detailed analysis of the particle is presented in figure 5.3, which shows the elemental mapping of the same particle for the elements Mg, Fe, Ca, K, O and Si by energy filtered EDS analysis.

Magnesium and iron, two of the main constituents of olivine, are not homogeneously distributed in the particle, but are present in distinctively different domains. On the other hand, oxygen and silicon show a homogeneous distribution inside the particle. The iron-rich domains

correspond to the brighter fields in Fig. 5.1 as well, since Fe is a heavier element compared to Mg. Moreover, surface enrichment of iron can be observed in Fig. 5.3, in agreement with previous research [13, 14, 18, 34].

Furthermore, clearly a free iron phase, as described in chapter 4, can be seen in the middle bottom, where Fe and O are present, but Mg and Si to a much lesser extent. This indicates an Fe-oxide or $MgFe_2O_4$ phase, able to participate in i.e. oxygen transport [14].

Calcium is only present at the outer surface of the particle and is thus a major constituent of the porous coating of the particle. Potassium is the only other element that could be detected by EDS which does not originate from olivine ($(Mg,Fe)_2SiO_4$) itself. It is mostly present in iron-rich areas inside the particle and at the outermost surface.

To study the chemical composition of the coating layer, XPS has been used in combination with depth profiling. Figure 5.4 shows an XPS depth profile of a used olivine particle, where the atomic concentrations of the main elements found are plotted as a function of etch time, which
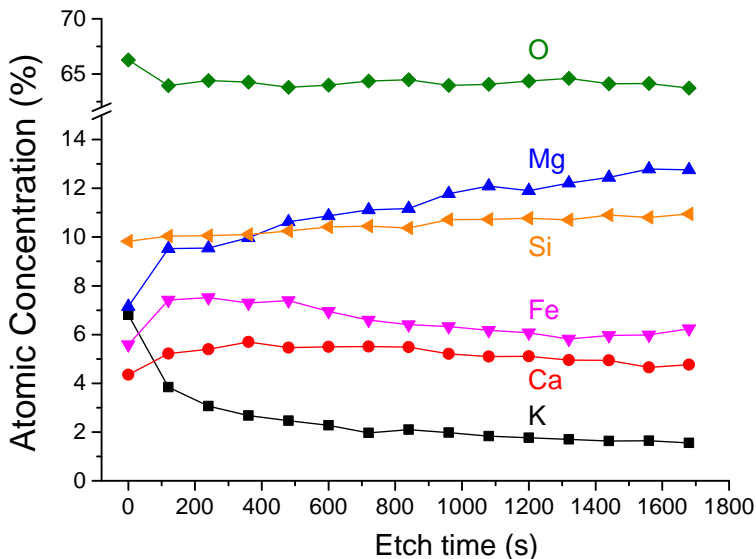

Figure 5.4: Atomic concentrations of elements present in a particle of used olivine, as a function of sample depth. Each measurement point (120 s etching) corresponds to approximately 35 nm sample depth

corresponds to the sample depth. The calcium concentration does not change significantly as a function of analyzed sample depth, indicating that the Ca-rich surface layer is uniform and has a thickness of at least 0.5 μm.

The potassium concentration, on the other hand, is not uniformly distributed in the surface layer of the coating; the relative amount of K present decreases exponentially from 7 atom % at the outer surface of the particles to about 2% already after a few hundred nanometers into the surface layer.

The atomic surface concentrations of silicon and oxygen do not vary much with increasing etching, indicating that Si and O are homogeneously distributed throughout the sample, in agreement with the observations in the SEM-EDS images. The iron concentration at the surface (etch time = 0) is significantly higher compared to fresh olivine [14] and the iron concentration in the subsurface layers (etch time $\geqslant$ 120 s) does not decrease exponentially, pointing to a homogeneous iron enriched surface layer with a thickness of at least 0.5 μm, in agreement with the SEM-EDS analysis.

An interesting observation is that, after 120 s etch time, Fe and Mg appear to be each other's mirror images. The deviation from this trend at the outer surface can be explained by the high potassium concentration at the outermost surface, which is largely removed during the first etching step. As a result of this, all other elements, except oxygen, increase in relative concentration.

5.3.2 *Influence of the Coating on the Reactivity of the Bed Material*

The samples used for the activity measurements have been characterized with XPS to study their chemical composition, as shown in figure 5.5, and the atomic concentrations derived from these spectra are presented in table 5.1. The spectra identify the elements present from approximately 0.5 atom%. The main peak for each element found is indicated at the top.

Fresh olivine shows only peaks from elements present in $(Mg,Fe)_2SiO_4$. These peaks can be found in the spectrum of used olivine as well, but furthermore, a K 2p peak can be seen around 295 eV and to a lesser
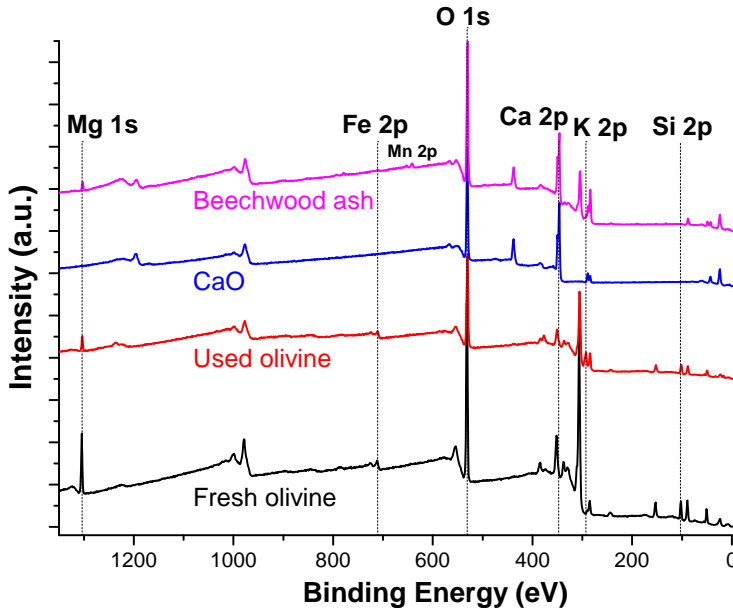
Figure 5.5: XPS wide scans of the samples which were used for WGS-activity measurements

extent, a small Ca 2s peak at 438 eV and a Ca 2p peak at 350 eV, which overlaps largely with a magnesium KLL Auger line.

The CaO sample only shows peaks for calcium, oxygen and carbon, both as adventitious carbon and as carbonate. This carbonate was also

Table 5.1: Atomic concentrations in % of the samples, used for WGS-activity measurements

	Fe	Mg	Si	O	Ca	K	C*	Mn
Fresh olivine	1.0	20.5	13.4	65.0	-	-	-	-
Oxidized olivine	5.8	17.1	10.9	66.3	-	-	-	-
Used olivine	5.4	7.0	9.6	64.4	4.2	6.6	2.8	-
CaO	-	-	-	65.0	24.5	-	10.5	-
Beechwood ash	~0.5	11.1	-	55.8	18.0	1.1	12.6	~0.8

* Only C from carbonate ions included

observed in the used olivine and beechwood ash samples. The spectrum for the beechwood ash showed mostly alkaline and alkaline earth metal oxides and carbonates, with main compounds being Ca- and Mg-oxides or carbonates. The only d-metal(oxide) that can clearly be observed is manganese in the MnO form. Manganese has previously been reported to be the most abundant d-metal present in woody biomass ash [16].

Both the oxidized and used olivine have an iron surface concentration which is 5 times higher compared to fresh olivine, whereas the beechwood ash only contains 0.5 at.% iron. Another observation worth pointing out is that used olivine, CaO and beechwood ash contain carbonates. This means that a fraction of calcium, magnesium and/or potassium in these samples are present as carbonate at the surface.

As a measure for water-gas shift (WGS) activity, the hydrogen production as a function of temperature of three olivine samples is presented in figure 5.6. The feed gas of CO/H_2O (1/1) was diluted with Ar as an internal standard and the hydrogen production was determined by on-line mass spectrometry and displayed as mass 2 (H_2) divided by mass 40 (Ar).

Unused fresh olivine has a low WGS activity, similar to the empty reactor, and does show very little temperature dependence up to 800 °C.

Similar to the fresh olivine, the olivine which has been oxidized for 1 h (olivine ox (1h)) does not show a temperature dependence in the WGS activity, although the oxidized olivine has 5 times more iron at the surface than fresh olivine [13, 14].

In contrast, used olivine exhibits significant WGS activity at temperatures above 600 °C. This can be attributed to the coating of the material,

Table 5.2: WGS activity of olivine (fresh and used) and reference samples at 800 °C

	Hydrogen production at 800 °C Ion current 2/40 [mA]
Fresh Olivine	1.4
Used Olivine	6.7
Calcite (CaO)	7.4
Beechwood ash	14.0
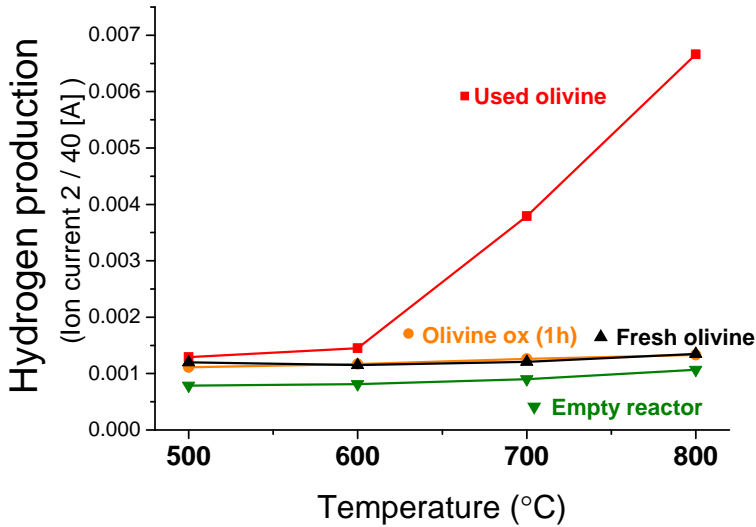
Figure 5.6: WGS activity of fresh olivine, oxidized olivine and used olivine as a function of temperature

since the particle size is similar to the unused and oxidized olivine. Because used olivine has a comparable iron surface concentration as the oxidized olivine, but a much higher WGS activity, the increased Fe surface concentration does not seem to play a role in catalyzing the WGS reaction. It should be noted that the BET surface area is about 1.7 times larger for the used olivine but the hydrogen production at 800 °C is 5 times larger. This suggests that it is the surface chemistry of the coating layer that is the main reason behind the observed increase in activity.

Because the bed material coating consists mainly of calcium oxide or carbonate, a sample of pure CaO (calcite) has been tested as well and showed similar WGS activity compared to the used olivine sample, see table 5.2. The highest hydrogen production could be observed for the biomass ash sample. For all the samples, the hydrogen production increases with increasing temperatures.

5.4   DISCUSSION

The results presented in this chapter provide insight into the nature of bed material coating, built up during indirect biomass gasification. The research can be divided into two parts: in the first part, the chemical composition of the bed material coating and the biomass ash were investigated and in the second part, the influence of the coating on the reactivity of the bed material was evaluated by means of the enhanced hydrogen production by the WGS reaction.

5.4.1   *Formation and Composition of the Coating*

Coating-formation on bed material particles during continuous use in indirect or dual fluidized-bed biomass gasification is a common phenomenon and caused by interaction of the bed material with the biomass fuel, in particular the ash residue [17].

The SEM picture (Fig. 5.1) of the cross section of an used olivine particle showed a porous surface layer and the energy filtered EDS analysis (Fig. 5.3) showed the presence of calcium in this layer. Moreover, K was found to be present both at the surface of the particle and in the bulk, in contrast with Ca, which was only found at the outer surface. Apart from Ca and K, enrichment of iron at the surface could be observed.

These findings are in agreement with the XPS depth profile of a used olivine particle, which showed an increased Ca concentration throughout the measured surface layer of 0.5 μm. Potassium was found to be present in highest concentration at the very outermost surface, but is also present throughout the entire investigated surface layer, in agreement with SEM observations. Moreover, the iron concentration in the coating layer was much higher (6 atom% average throughout the layer), compared to the iron surface concentration of unused olivine, which is 1 atom%. Upon etching, the relative ratio of Mg/Fe increases, as observed previously in an oxidized olivine sample [14].

Since the coating is formed by interaction with the biomass ash, the ash of beech wood was characterized and used in WGS experiments. The XPS spectrum showed that the ash sample consisted mainly of Ca and Mg

oxides or carbonates. This is in agreement with other characterizations of woody biomass ash, taken from gasifiers, by XRF [16] and ICP [35]. The presence of all elements of olivine in the coating layer could indicate that the Ca-rich coating is not a solid, non-porous surface layer, but that a large fraction of the coating still consists of elements, which are present in olivine. However, both these studies report that a large amount of K is present in woody biomass ash as well, whereas only 1% was observed in the XPS spectrum of the beechwood ash.

This could be explained by either the low content of K in the beechwood sample or by the volatility of K already at 800 °C [36]. This can result in removal of K from the beechwood sample with the gas stream used in our experiment.

The absence of Si in the beechwood ash sample is hard to explain by the results presented here, since it is also a major constituent of woody biomass ash [17]. The different types of biomass that were used for characterization can play a role.

Although earlier studies describe coating formation on bed materials during fluidized-bed combustion of biomass, Öhman et al. were the first to study in detail the formation of coatings on bed material during gasification of biomass [37]. They showed that different coatings are formed on quartz, depending on the kind of biomass used. Moreover, the coating was found to consist of two distinct layers; a thin porous outer layer, consisting mostly of particles and a thicker homogeneous inner layer. Kirnbauer et al. [17] summarized the coating formation mechanism from woody biomass in two steps: First, the K containing ash components melt and then the Ca containing compounds dissolve or diffuse into this melt, which subsequently is sintered on the outer layer of the bed material particles. K can also directly be deposited onto the surface of the particles from the aerosol- or gas phase.

During fluidized-bed biomass combustion, Grimm et al. found coatings similar to Öhman et al., consisting of two layers on both quartz and olivine [38]. Both Ca and K were found in the inner and outer layer deposited on quartz, but no K was found in the inner layer on olivine. This is in partial agreement with the finding that K is mostly present at the outer surface of used olivine, as determined by XPS depth profiling.

The SEM-EDS pictures indicated that K was present inside the particles as well, which seems to be in contrast with findings of Grimm et al., who calculated a low chemical driving force for K to be retained by olivine [38]. However, K is known to be a volatile ash component [16, 35, 36] and therefore, is able to penetrate the cracks, which are present in used olivine and caused by continuous oxidation/reduction cycles [14, 15]. In these cracks, there is close contact with the gas phase, which leads to iron segregation. This close contact can also lead to K-enrichment since this is a volatile component and could explain why there seems to be a correlation between Fe and K inside the olivine particles.

It should be noted that energy filtered SEM-EDS analysis is not used as a quantitative characterization technique in this study, so the amount of K visible inside the particles is unknown and may be low. On the other hand, Kirnbauer et al. reported a potassium concentration of 8.5 wt.% inside a used olivine particle, determined by EDX [16]. This relatively high concentration may be caused by interaction of the olivine with the biomass ash for a much longer time than the 30 h that the olivine was used in this study. Another explanation might be the characterization of an Fe-rich particle, where Fe and K correlate. This would also explain the relatively high Fe concentrations inside both unused and used olivine particles, 11.8 and 12.5 wt.%, respectively, in contrast to the average iron content of unused olivine, which is approximately 6.5 wt.%, as determined by ICP [14].

Based on the data and pictures presented in this chapter, the following mechanism is proposed for the coating of the olivine particles during indirect biomass gasification:

During the first stages of use, the iron in olivine will segregate to the surface of the particles [13]. During the contact with the biomass, ash compounds, including Ca and K, dissolve into this iron-rich surface layer. This explains the presence of Ca at all surfaces of the particle, as observed with SEM-EDS and by XPS depth profiling. Iron is still able to migrate through this surface layer, as indicated by the relatively high iron concentration throughout this surface layer. It is unlikely that the iron in the surface layer originates from the biomass ash, since iron is present in very minor amounts in the biomass ash (only 0.5 atom%).

Because K is more mobile and volatile than Ca, it can also dissolve in the cracks, present in the Fe-rich domains in the interior of the particle, explaining the presence of potassium inside the used olivine particles and the Fe - K correlation.

Upon interaction with the olivine particles, the biomass ash will also adsorb on the surface of the bed material. This can be seen in figure 5.2 and this also nearly doubled the BET surface area of the bed material particles. Since the average particle size of the used olivine was significantly larger than the fresh olivine, this indicates that these ash deposits are porous.

In this chapter, XPS in combination with depth profiling was used for characterization of the chemical composition of the bed material coating in contrast to other studies, which use SEM-EDX [16, 17, 18, 37]. The main advantage of XPS is that it can not only provide quantitative information on the elements present in the coating, but it provides qualitative information on the oxidation states. It was, however, not possible to determine local composition differences in the lateral direction, since all concentrations are averaged over an analysis area with a diameter of at least 30 micrometer.

In general, the depth profile of the used olivine particle is comparable to the results obtained by Kirnbauer et al. [16], with a thick, Ca rich layer and a surface that is richer in K than layers deeper inside the particle. From the binding energy Ca $2p_{3/2}$ peak, it is not possible to determine whether the calcium is present as CaO or as $CaCO_3$, since the binding energy for both Ca-species is similar [39]. However, the C 1s peak for the carbonate ion was found at 288.2 eV, whereas the carbonate C 1s peak of $CaCO_3$ has a binding energy of around 289.3 eV [40]. This indicates that calcium is likely to be present as CaO. The ratio potassium / carbonate in the used olivine sample is close to 2, as in K_2CO_3, so most likely, the carbonate in the used olivine is associated with the potassium.

In the CaO sample, part of the CaO has reacted with CO_2 in the air and formed $CaCO_3$, which is the thermodynamically most stable phase at room temperature [30].

5.4.2   *Influence of Coating on Reactivity*

The reactivity data of the samples showed two different behaviors; the samples which do not contain calcium or potassium show little WGS activity and no temperature dependence, whereas the samples which do contain calcium and/or potassium show increasing H_2 production at temperatures of 600 °C and above.

Since there is little iron at the surface of untreated fresh olivine, it is not surprising that the fresh olivine has little WGS activity. Moreover, more than half of the total amount of iron is present in the olivine matrix [14] and is therefore not able to act as a catalytically active metal. Similar behavior has been observed by Kern et al., who showed that fresh olivine had a similar CO conversion in WGS as an empty reactor at 800 °C [25].

The olivine which has been oxidized for one hour has significantly more iron at the surface and a significant part of the iron is present as free iron-oxide phases [14]. Although iron-oxide is known to be a good WGS catalyst, the oxidized olivine does not show more WGS activity than untreated olivine. The oxidation state of iron could explain this low WGS activity; iron in a gas environment of CO and H_2O (ratio 1/1) is not present as magnetite (Fe_3O_4), but as wüstite (FeO) at temperatures of 500 °C and above [41]. The magnetite phase is known for its WGS activity [42].

The measured samples that do contain calcium all have a higher WGS activity, so it seems straight-forward to attribute this activity to the presence of calcium alone. Indeed, pure CaO is frequently used as a catalyst material [21, 22, 31, 43, 44], or as "support" for iron catalysts [45, 46, 47] in WGS reactions or biomass steam gasification.

Li et al. report that both CaO and $CaCO_3$ can act as a WGS catalysts at temperatures of 600 °C and above [44]. On the other hand, CaO is able to react with steam, forming $Ca(OH)_2$, which has less catalytic activity in the WGS reaction [44]. Kirnbauer et al. reported a high concentration of active oxygen on the CaO surface, which promotes the WGS reaction [19].

Although the CaO sample and the used olivine have a comparable WGS activity at 800 °C, the used olivine sample contained much less

CaO than the calcite sample (the sample amount was the same in each experiment). An explanation for the similar H_2 production could be that something else is affecting the reactivity of the used olivine sample, since it consists for only a small fraction of CaO and the surface area is smaller than the CaO sample. It is possible that the increased iron or potassium concentration at the surface of the used olivine contributes to the observed WGS activity. Zamboni et al. have shown that addition of Ca to olivine increases the dispersion of iron-oxide [48]. In this view, the used olivine could be seen as a CaO-supported, K-promoted iron catalyst.

Another explanation might be the presence of calcium and magnesium at the surface. If part of the magnesium at the surface of used olivine is present as $MgCO_3$, it can, together with the CaO, be responsible for the observed WGS activity, since it promotes the WGS reaction [49].

The beechwood ash sample also consists mainly of Ca- and Mg-oxides and carbonates and exhibits the highest WGS activity at 800 °C.

This points to a combined effect of the calcium-, magnesium- , potassium and other species present in wood ash for the catalysis of the WGS reaction. These species are present both in the beechwood ash sample and at the surface of the used olivine.

5.4.3 *Implications for Large Scale Indirect Biomass Gasification*

The formation of a coating on bed material particles does not only influence the WGS reaction rate during industrial scale biomass gasification. The CaO at the surface of used olivine can also catalyze other reactions. Widyawati et al. have identified three functions of CaO during pyrolysis of various kinds of biomass [22]: i) it acts as a primary catalyst, producing H_2 directly from the biomass; ii) CaO increases the hydrogen concentration by reforming and char gasification and iii) it accelerated the tar cracking. The tar cracking capability of CaO was further investigated by Udomsirichakorn et al., who showed that CaO does not only decrease the total tar content of the product gas, but also converts heavy tar species to fewer ring structures, resulting in a decrease of the tar dewpoint by 11 °C [21].

Performing gasification at lower temperatures has the advantage that CaO can bind CO_2 to form $CaCO_3$, which is thermodynamically stable at lower temperatures [30]. This drives the WGS equilibrium to the H_2 side. Pfeifer and coworkers have compared dual fluidized-bed gasification of biomass with and without CO_2 selective transport and show an increase of the hydrogen concentration in the product gas from 40% with olivine as bed material, to 70% with CaO, on a dry basis [43]. Gasification with CaO as bed material was carried out at 645 °C, instead of 841 °C, when olivine was used. Although the gasification temperature was significantly lower, the tar content of the product gas was lower as well (3.5 vs. 1.4 g/Nm^3 for olivine and CaO, respectively).

Kirnbauer et al. showed that gasification at lower temperatures can improve the performance of fluidized-bed gasification when the bed material is coated by calcium. Besides promoting the WGS reaction, the recombination of cyclic hydrocarbons into multi-ring tar compounds is inhibited. In other words: the calcium coating prevents the formation of heavy tars and this is even more the case at lower temperatures [19].

The calcium at the surface of used olivine is also able to react with the surface iron to form $Ca_2Fe_2O_5$, which increases the hydrogen concentration in the product gas of biomass gasification [47]. Moreover, Di Felice et al. showed that both CaO and MgO, which might be present in used olivine, are active in catalytic tar reforming, and that their activity is increased by the incorporation of iron [46]. Since iron is able to transport oxygen from the oxidation zone to the gasification zone in indirect biomass gasification [14], these observations are very relevant when evaluating olivine as a primary catalyst. Iron can provide the oxygen that can be used by calcium-species to catalyze tar degradation, so it is beneficial to have both iron and calcium present at the surface of the bed material.

The presence of biomass ash itself inside gasifiers may also influence the reactions taking place. Addition of wood ash, consisting mainly of calcium, magnesium and potassium, was found to have a significant positive effect on the reaction rate of gasification of both wood and coal [50]. Several researchers have already identified these metal-species as catalysts during biomass gasification [26, 27, 51].

Delgado et al. compared MgO, CaO and dolomite (MgO-CaO) as catalysts for hot gas cleaning from fluidized-bed gasification and found dolomite to be the most active in tar elimination, followed by MgO and CaO [23]. Moreover, magnesite ($MgCO_3$) showed activity in promoting the WGS reaction, methane reforming and tar reduction during circulating fluidized-bed biomass gasification at temperatures slightly above 800 °C [49].

Constantinou et al. compared calcined olivine, calcite and dolomite in steam reforming of model tar compounds towards H_2 production. Both calcite and dolomite showed increasing hydrogen production when the temperature was increased from 650 °C to 800 °C, but opposite behavior was observed for olivine [52]. At 800 °C, dolomite had the highest activity per gram basis, followed by calcite and olivine.

The natural mineral dolomite has been previously identified as an active catalyst for tar cracking, which results in enhanced hydrogen production during biomass gasification [53]. The activity of dolomite outperforms olivine, but the main drawback is that dolomite is very brittle, which makes it unusable in fluidized-bed based indirect biomass gasification [9]. Since olivine, and thus used olivine as well, is much harder, there is much less attrition and the bed material is not blown out with the product gas.

The used olivine has Ca-oxide, Mg-species and carbonates at the surface, so it could be seen as an olivine with a dolomite-like shell with iron and potassium promoters, which is both strong enough for use in circulating fluidized-bed reactors and more active than olivine itself, both towards tar reduction and for increasing the H_2 concentration in the product gas.

5.5   CONCLUDING REMARKS

Coating layers, consisting largely of calcium oxide phases and originating from contact with biomass ash, deposit on olivine bed material, during the gasification of biomass. The composition and reactivity of these coating layers have been investigated in this chapter.

SEM-EDS analysis showed that already after 30 h of biomass gasi-fication, a surface layer, containing calcium and potassium, is formed on olivine. No calcium was observed inside the particle, in contrast to potassium, which was present in iron-rich areas inside the particles. XPS depth profiling showed that this Ca-rich surface layer also contained car-bonate species and is at least 0.5 micrometer thick. Although the average particles size of the olivine particles increases during use as bed material, the BET surface area increases as well. This shows that the bed material coating is porous.

A mechanism for the coating of the bed material is proposed, involving iron segregation to the surface during the first stages of use of olivine as a bed material. Ash compounds are incorporated in this surface layer, in which Fe is still mobile and K is able to penetrate deep into the particles, because of its volatility.

The coating is responsible for enhanced hydrogen production through its catalytic activity in the water-gas shift reaction. The presence of cal-cium, potassium and carbonate species at the surface of used olivine, calcite and in the beechwood ash increased the WGS reaction rate. The WGS-activity of the coated material is almost a factor 5 higher than that of uncoated olivine and much higher than the increase in surface area, which was increased by only a factor of 1.7.

Biomass ash compounds were also found the be WGS active and are known to be active towards tar reduction as well. Based the results, presented in this chapter, it can be concluded that the bed material coating, as observed during indirect biomass gasification, influences the reactivity of the material. Used olivine is more active towards hydrogen production than fresh olivine, because of a coating, formed by biomass ash compounds. Comparable compounds could also be used as additives, to improve the performance of the gasification process, since these ash compounds are active as well.

REFERENCES

[1] T. Damartzis and A. Zabaniotou, Renewable and Sustainable Energy Reviews 15 (2011) 366–378.

[2] A. V. Bridgwater, Chemical Engineering Journal 91 (2003) 87–102.

[3] G. W. Huber, S. Iborra and A. Corma, Chemical Reviews 106 (2006) 4044–4098.

[4] J. Pecho, T. J. Schildhauer, M. Sturzenegger, S. Biollaz and A. Wokaun, Chemical Engineering Science 63 (2008) 2465–2476.

[5] K. Zhang, J. Chang, Y. Guan, H. Chen, Y. Yang and J. Jiang, Renewable Energy 49 (2013) 175–184.

[6] K. Göransson, U. Söderlind, J. He and W. Zhang, Renewable and Sustainable Energy Reviews 15 (2011) 482–492.

[7] C. M. van der Meijden, *Development of the MILENA gasification technology for the production of Bio-SNG*, PhD Thesis, Eindhoven University of Technology, 2010.

[8] L. Devi, K. J. Ptasinski and F. J. J. G. Janssen, Biomass and Bioenergy 24 (2003) 125–140.

[9] J. Corella, J. M. Toledo and R. Padilla, Energy & Fuels 18 (2004) 713–720.

[10] H. Hofbauer, R. Rauch, K. Bosch, R. Koch and C. Aichernig, *Biomass CHP plant Güssing - A success story*, Pyrolysis and Gasification of Biomass and Waste, A. V. Bridgwater (Ed.), CPL Press, Newbury, Berks, UK, 2003.

[11] L. Devi, K. J. Ptasinski and F. J. J. G. Janssen, Fuel Processing Technology 86 (2005) 707 – 730.

[12] J. N. Kuhn, Z. Zhao, L. G. Felix, R. B. Slimane, C. W. Choi and U. S. Ozkan, Applied Catalysis B: Environmental 81 (2008) 14–26.

[13] H. O. A. Fredriksson, R. J. Lancee, P. C. Thüne, H. J. Veringa and J. W. Niemantsverdriet, Applied Catalysis B: Environmental 130-131 (2013) 168–177.

[14] R. J. Lancee, A. I. Dugulan, P. C. Thüne, H. J. Veringa, J. W. Niemantsverdriet and H. O. A. Fredriksson, Applied Catalysis B: Environmental 145 (2014) 216–222.

[15] D. Swierczynski, C. Courson, L. Bedel, A. Kiennemann and S. Vilminot, Chemistry of Materials 18 (2006) 897–905.

[16] F. Kirnbauer and H. Hofbauer, Energy & Fuels 25 (2011) 3793–3798.

[17] F. Kirnbauer and H. Hofbauer, Powder Technology 245 (2013) 94–104.

[18] A. J. Grootjes, C. M. van der Meijden, H. J. M. Visser and A. van der Drift, *Improved Gasifier Availability with Bed Material and Additives*, Proceedings of the 21st European Biomass Conference and Exhibition, 2013.

[19] F. Kirnbauer, V. Wilk and H. Hofbauer, Fuel 108 (2013) 534–542.

[20] G. Xu, T. Murakami, T. Suda, S. Kusama and T. Fujimori, Industrial & Engineering Chemistry Research 44 (2005) 5864–5868.

[21] J. Udomsirichakorn, P. Basu, P. A. Salam and B. Acharya, International Journal of Hydrogen Energy 38 (2013) 14495–14504.

[22] M. Widyawati, T. L. Church, N. H. Florin and A. T. Harris, International Journal of Hydrogen Energy 36 (2011) 4800–4813.

[23] J. Delgado, M. P. Aznar and J. Corella, Industrial & Engineering Chemistry Research 36 (1997) 1535–1543.

[24] F. Kirnbauer, V. Wilk, H. Kitzler, S. Kern and H. Hofbauer, Fuel 95 (2012) 553–562.

[25] S. Kern, C. Pfeifer and H. Hofbauer, Biomass and Bioenergy 55 (2013) 227–233.

[26] L. K. Mudge, E. G. Baker, D. H. Mitchell and M. D. Brown, Journal of Solar Energy Engineering 107 (1985) 88–92.

[27] Z. Wang, F. Wang, J. Cao and J. Wang, Fuel Processing Technology 91 (2010) 942–950.

[28] S. Anis and Z. A. Zainal, Renewable and Sustainable Energy Reviews 15 (2011) 2355–2377.

[29] J. Blamey, E. J. Anthony, J. Wang and P. S. Fennell, Progress in Energy and Combustion Science 36 (2010) 260–279.

[30] N. H. Florin and A. T. Harris, Chemical Engineering Science 63 (2008) 287–316.

[31] S. Koppatz, C. Pfeifer, R. Rauch, H. Hofbauer, T. Marquard-Moellenstedt and M. Specht, Fuel Processing Technology 90 (2009) 914–921.

[32] J. Udomsirichakorn and P. A. Salam, Renewable and Sustainable Energy Reviews 30 (2014) 565–579.

[33] M. Virginie, C. Courson, D. Niznansky, N. Chaoui and A. Kiennemann, Applied Catalysis B: Environmental 101 (2010) 90–100.

[34] L. Devi, M. Craje, P. Thüne, K. J. Ptasinski and F. J. J. G. Janssen, Applied Catalysis A: General 294 (2005) 68–79.

[35] C. Ma, F. Weiland, H. Hedman, D. Boström, R. Backman and M. Öhman, Energy & Fuels 27 (2013) 6801–6814.

[36] P. A. Tchoffor, K. O. Davidsson and H. Thunman, Energy & Fuels 27 (2013) 7510–7520.

[37] M. Öhman, L. Pommer and A. Nordin, Energy & Fuels 19 (2005) 1742–1748.

[38] A. Grimm, M. Öhman, T. Lindberg, A. Fredriksson and D. Boström, Energy & Fuels 26 (2012) 4550–4559.

[39] B. Demri and D. Muster, Journal of Materials Processing Technology 55 (1995) 311–314.

[40] M. Ni and B. D. Ratner, Surface and Interface Analysis 40 (2008) 1356–1361.

[41] Calculated with HSC Chemistry, version 7.11

[42] C. Ratnasamy and J. P. Wagner, Catalysis Reviews 51 (2009) 325–440.

[43] C. Pfeifer, B. Puchner and H. Hofbauer, Chemical Engineering Science 64 (2009) 5073–5083.

[44] Z. Li, Y. Liu and N. Cai, International Journal of Hydrogen Energy 37 (2012) 11227–11236.

[45] I. Zamboni, C. Courson and A. Kiennemann, Catalysis Today 176 (2011) 197–201.

[46] L. Di Felice, C. Courson, D. Niznansky, P. U. Foscolo and A. Kiennemann, Energy & Fuels 24 (2010) 4034–4045.

[47] B.-S. Huang, H.-Y. Chen, K.-H. Chuang, R.-X. Yang and M.-Y. Wey, International Journal of Hydrogen Energy 37 (2012) 6511–6518.

[48] I. Zamboni, C. Courson, D. Niznansky and A. Kiennemann, Applied Catalysis B: Environmental 145 (2014) 63–72.

[49] M. Siedlecki, R. Nieuwstraten, E. Simeone, W. de Jong and A. H. M. Verkooijen, Energy & Fuels 23 (2009) 5643–5654.

[50] W. B. Hauserman, International Journal of Hydrogen Energy 19 (1994) 413–419.

[51] K. Mitsuoka, S. Hayashi, H. Amano, K. Kayahara, E. Sasaoka and M. A. Uddin, Fuel Processing Technology 92 (2011) 26–31.

[52] D. A. Constantinou, J. L. G. Fierro and A. M. Efstathiou, Applied Catalysis B: Environmental 95 (2010) 255–269.

[53] D. Sutton, B. Kelleher and J. R. H. Ross, Fuel Processing Technology 73 (2001) 155–173.

6

CHAPTER

Development and Characterization of a Spherical, Non-Porous Fe/SiO$_2$ Model Catalyst

abstract

Detailed characterization of conventional porous heterogeneous catalysts is usually difficult, since the relevant structural, morphological and chemical changes take place on the active metal nanoparticles. When these particles are situated inside the pores, they cannot be studied with electron microscopy or surface sensitive characterization techniques, such as XPS. The surface science approach to model these complex porous supported catalyst is a good way to overcome these limitations. However, measuring catalytic activity of such system is not easy.

The goal of the research described in this chapter is to prepare a high surface area model catalyst, involving colloidal uniform nanoparticles on a non-porous support. This powder model catalyst is a promising compromise between the high surface area porous industrial catalysts and the planar model catalyst.

Monodisperse SiO$_2$ spheres with diameters between 850 - 900 nm have been be synthesized, which can serve as a model support for well-defined powder iron/SiO$_2$ model catalysts.

The impregnation of iron nanoparticles on these Stöber spheres resulted in a dispersed Fe/SiO$_2$ model catalyst, which can be studied with both electron microscopy and XPS on one hand and with XRD and other bulk characterization techniques on the other hand.

Conventional heterogeneous catalysts usually consist of a large number of metal nanoparticles dispersed in the pores of a larger porous support particle, as described in chapter 1. Detailed characterization of such catalysts from a mechanistic point of view is difficult, since the relevant structural, morphological and chemical changes take place on the active metal nanoparticles. These changes are hard to study with microscopic techniques as TEM and SEM, and with surface sensitive techniques, such as XPS when the metal particles are situated inside the pores. Furthermore, inside the pores, diffusion of gaseous species may limit a catalytic reaction, making it hard to distinguish the origin of changes in the catalysts activity. The surface science approach to model these complex porous supported catalysts is a good way to overcome these limitations [1].

Model systems can be designed so that they allow detailed characterization by surface science techniques, sometimes even in-situ, under realistic reaction conditions. A frequently used model system is a planar model support, impregnated with the metal nanoparticles of interest, for instance a planar SiO_2 supported iron catalyst [2]. The oxidized top layer of the Si-wafer mimics the industrial SiO_2 support and the Fe nanoparticles are anchored to the support via conventional wet impregnation, yielding a realistic model catalyst. These planar model system are suitable to be studied with XPS, TEM and even in-situ with EXAFS [3].

To study the catalytic activity related to the changes observed with the different characterization techniques is for these model systems, however, not straight forward. The absolute amount of active material, the metal nanoparticles, is very low and thus the changes in reactive mixtures that these particles induce are very small and hard to detect and quantify with analysis techniques. This is especially true for reactions that are not ran in batch mode.

A non-porous powder model catalyst could act as promising compromise between the high surface area porous industrial catalysts and the planar model catalyst [4, 5]. A non-porous, spherical model catalyst allows one to study both the morphological and chemical transformations

of the supported metal nanoparticles upon different treatments. Moreover, since the catalyst is a powder, it can be used in significant amounts for catalytic testing in e.g. a fixed-bed reactor, or in characterization studies that require significant amounts of material, such as XRD of Mössbauer Spectroscopy.

From the viewpoint of the work described in this thesis, iron is the obvious choice for the active metal. The concept can, however, easily be extended to other interesting catalyst materials. Since the iron oxide in olivine is formed from the iron silicate phase, leaving behind amorphous silica, a silica supported iron catalyst would be a good model catalyst for olivine, as described in chapter 3. Fe/SiO_2 model systems are frequently studied as Fischer-Tropsch catalysts [6], however, very few reports in literature exist on spherical iron model catalysts [7].

Spherical, non-porous silica particles can relatively easily be synthesized via the so-called Stöber synthesis [8]. Stöber and co-workers described a system of chemical reactions to grow silica particles with a uniform size. It basically involves the hydrolysis of alkyl silicates, followed by condensation of the silicic acids in alcoholic solutions, with ammonia as a structural catalyst. This work was extended by Bogush et al., who determined the range of reactant concentrations, that resulted in the precipitation of monodisperse particles [9]. Moreover, Deng et al. reported the influence of the reactants on the final particle size, which could be adjusted in a broad range to yield monodisperse particles with a standard deviation of less than 2% [10].

Escobedo and co-workers described the reaction mechanism from tetraethylorthosilicate (TEOS) to Stöber spheres in detail [11], as illustrated in Fig. 6.1.

The first step is a nucleophilic substitution of one ethoxy group by a hydroxyl group from water. The partially hydrolyzed TEOS undergoes this substitution three more times to obtain the silicic acid $Si(OH)_4$. This silicic acid subsequently undergoes condensation reactions to yield the SiO_2 product. Under the influence of the structural catalyst ammonium hydroxide, the surface tension increases. The system always strives to the lowest surface tension, which is reached when spheres are formed.
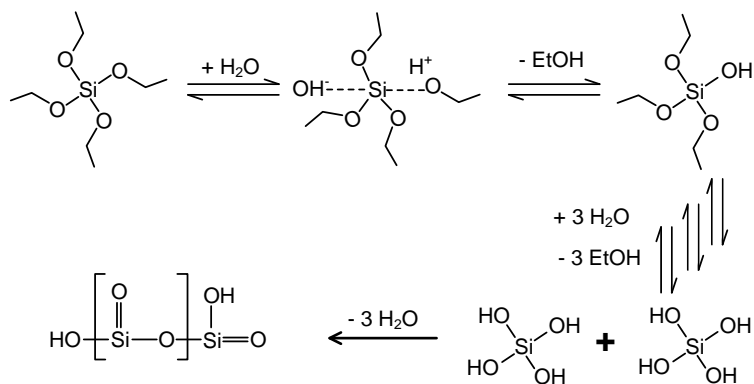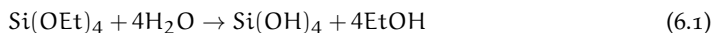
Figure 6.1: The series of reactions leading to Stöber silica

The overall reaction equations are thus:

$$Si(OEt)_4 + 4H_2O \rightarrow Si(OH)_4 + 4EtOH \qquad (6.1)$$

$$nSi(OH)_4 \rightarrow nSiO_2 + 2nH_2O \qquad (6.2)$$

Synthesis of monodisperse iron nanoparticles with a narrow size distribution can easily be performed without the need of a size-selection process [12]. Loading of metal nanoparticles on the Stöber spheres can be done by means of conventional impregnation by mixing the Stöber spheres with a nanoparticle solution. However, true impregnation is only possible in the presence of pores, but Saib et al. showed that this technique is suitable for anchoring nanoparticles on Stöber spheres [13].

The goal of this chapter is to present the first steps towards a well-defined powder iron model catalyst. Stöber spheres have been synthesized and impregnated with iron nanoparticles.

The synthesis process was followed using electron microscopy and X-ray Photoelectron Spectroscopy and X-ray Diffraction was used to show that this powder model catalyst can be used for bulk characterization techniques as well.

6.2 EXPERIMENTAL

6.2.1 *Synthesis of Stöber Spheres*

The monodisperse Stöber spheres were synthesized as follows: 71.5 mL of ethanol (Merck, Absolute, for analysis) was added to 25 mL of an ammonium hydroxide solution (28.0 - 30.0%, Merck, for synthesis). Subsequently, 12 mL of deionized water was added. After stirring for 3 minutes, 6 mL tetraethylorthosilicate (Merck, for synthesis) was added. After 5 minutes, the solution went from colorless to white, indicating the formation of solids, and the reaction was allowed to run for 3 hours. The reaction mixture was then centrifuged for 12 minutes at 8000 rpm and the solid Stöber SiO$_2$ powder was separated from the solvent. The powder was subsequently dried overnight in an oven at 110 °C and afterwards calcined at 400 °C (10 °C/min) for 4 hours in a gas flow of 20% O$_2$/Ar.

6.2.2 *Synthesis of Iron Nanoparticles*

To prepare a colloidal iron nanoparticle solution, first an iron-oleate precursor was prepared. In a typical synthesis of iron-oleate complex, 10.8 g of iron chloride (FeCl$_3$·6H$_2$O, 40 mmol, Aldrich, 98%) and 36.5 g of sodium oleate (120 mmol, TCI, 95%) were dissolved in a mixture solvent composed of 80 mL ethanol, 60 mL distilled water and 140 mL hexane. The resulting solution was heated to 70 °C and kept at that temperature for 4 h. When the reaction was completed, the upper organic layer containing the iron-oleate complex was washed three times with 30 mL of distilled water in a separation funnel. After washing, hexane was evaporated using a rotary evaporator at $1 \cdot 10^{-2}$ mbar and 100 - 150 °C for 2 h, resulting in an iron-oleate complex in a waxy solid form.

Subsequently, 1.8 g (2 mmol) of the synthesized iron-oleate complex (as described above) and 0.28 g oleic acid (1 mmol, Aldrich, 90%) were dissolved in 16 g 1-octadecene (Aldrich, 90%) at room temperature. The mixture was heated to 320 °C with a constant heating rate of 3.3 °C/min, and then kept at that temperature for 30 min. When the reaction temperature reached 320 °C, the initial transparent solution became turbid

and brownish black. The resulting solution, containing the dispersed nanoparticles, was then cooled to room temperature, and 28 mL of ethanol was added to the solution to precipitate the nanoparticles. The nanoparticles were separated after centrifugation at 10000 rpm for 12 min.

6.2.3   *Loading of Stöber Spheres with Fe Nanoparticles*

The solution of iron nanoparticles was diluted in toluene to obtain a 0.02 mmol Fe/mL solution and subsequently sonicated for 5 minutes. Then, 8.95 mL of the diluted Fe nanoparticle solution was mixed with 200 mg of calcined Stöber spheres to obtain a 5 wt.% Fe loading. This mixture was sonicated for 5 minutes and the toluene was allowed to evaporate slowly while stirring and sonicating. After all toluene was evaporated, the black solid powder product was dried overnight in an oven at 110 °C and subsequently calcined in 20% O_2/Ar at 350 °C (10 °C/min) for 5 hours to obtain the powder Fe/SiO_2 model catalyst.

6.2.4   *Characterization*

SEM pictures were taken using a FEI Quanta 3D FEG dual beam, operated in high vacuum mode with an accelerating voltage of 2.5 kV. The samples were supported on carbon tape and the working distance was 9 +/- 1 mm.

TEM measurements were carried out using a FEI Tecnai G^2 Sphera microscope with a LaB_6 filament at 200 kV and a bottom mounted 1024 x 1024 Gatan CCD camera. Samples were dispersed in ethanol and an appropriate amount of the sample was dropped onto a copper microscope grid covered with carbon windows.

For XPS, the samples were supported on conductive carbon tape and spectra were recorded using a Thermo Scientific K-Alpha spectrometer equipped with a monochromatic small-spot X-ray source and a 180 ° double focusing hemispherical analyzer with a 128-channel detector. Spectra were obtained using an aluminum anode (Al Kα, 1486.6 eV) operating at 72 W and a spot size of 400 μm.

Survey scans were measured at a pass energy of 200 eV and region scans at a pass energy of 50 eV. The background pressure was 2 x 10^{-8}

mbar and during measurement 3×10^{-7} mbar argon, because of the charge compensating dual beam source, which was used during all measurements. Analysis of the measurements was performed using Casa-XPS 2.3.16. All spectral positions were adjusted to the C 1s peak for adventitious carbon at 284.5 eV and the Si 2p, C 1s, O 1s and Fe 2p regions were used for quantification.

The X-ray Diffraction (XRD) pattern was recorded on a Bruker D2 Phaser using Cu Kα radiation (λ = 1.54 Å). Two theta angles from 20 to 70 degrees were measured with a step size of 0.008 $°$ and a time per step of 0.5 s.

6.3 RESULTS AND DISCUSSION

For the Stöber synthesis, reactant concentrations were chosen as such to achieve monodisperse particles of around 800 nm in diameter. The synthesis of the Stöber silica particles resulted in nicely shaped spheres with diameters between 850 - 900 nm. Not all the spheres were totally separated from each other, but more than 95% of all particles observed were separate spheres.
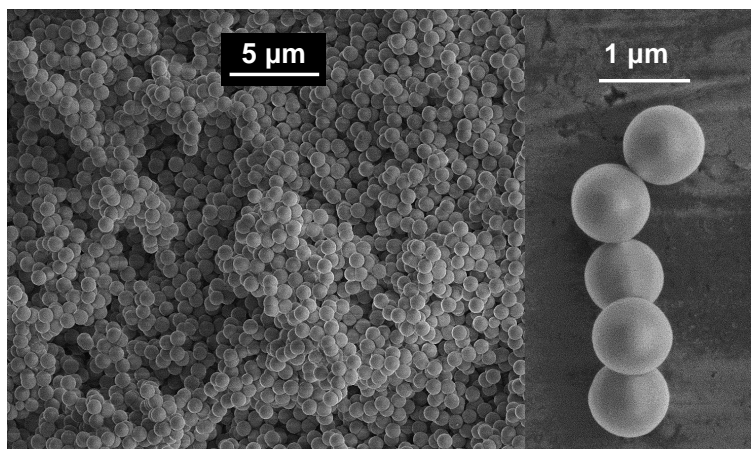

Figure 6.2: SEM images of the calcined Stöber spheres

Deng et al. showed that Stöber spheres with a very narrow distribution could be synthesized with a maximum diameter of approximately 770 nm, which is around 100 nm smaller than the particles in this work [10]. Bogush and co-workers reported that a particle size of around 800 nm would be the maximum to maintain maximum monodispersity [9]. The average particle size of the samples studied in this work is larger as is the particle size distribution . However, in their original work, Stöber and co-workers reported that relatively narrow size distributions could be achieved with average particle diameters up to 2 micrometer [8]. The size and size distribution of the particles synthesized in this work are suitable for use as a non-porous support for the spherical Fe-SiO$_2$ model catalyst.

From the TEM image of the iron nanoparticles (figure 6.3), it can be seen that the synthesis of these particles resulted in nicely shaped particles with an average diameter of around 10 nm.

Figure 6.4 shows the Stöber spheres after impregnation with the iron nanoparticle solution. The left picture shows the sample after drying at 110 °C, whereas the right picture shows the Fe-Stöber sample after
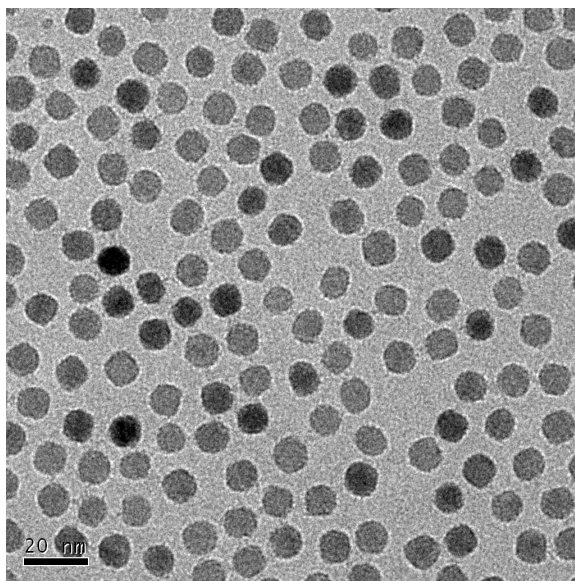

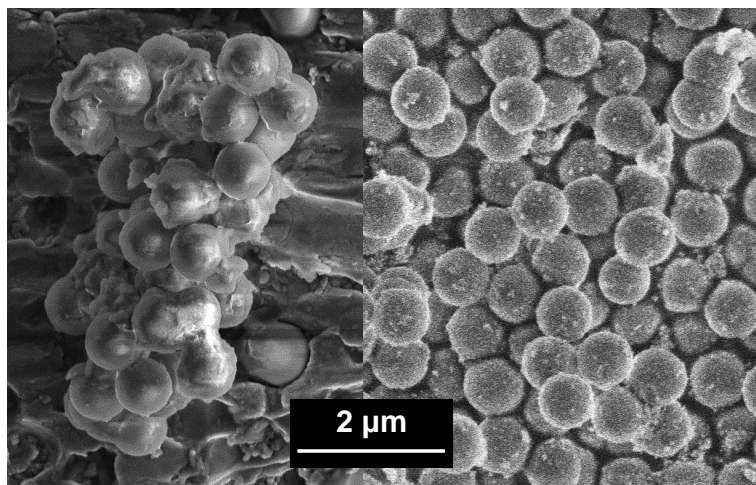**Figure 6.3:** TEM image of the iron nanoparticles

Figure 6.4: SEM images of the Fe-Stöber spheres samples, dried at 110 °C (left) and calcined in O_2/Ar at 350 °C for 5 h (right)

calcination at 350 °C. In the left picture, the particles are coagulated and no iron particles can be observed on the spheres. The oleic acid, which was used as a surfactant during the synthesis of the nanoparticles is still visible in between the Stöber spheres and causes the particles to stick together.

Calcination of the dried Fe-Stöber sample removes the oleic acid residues, which cannot be observed anymore in the right picture of the calcined sample. Several iron particles are clearly visible on top of the spheres and they are dispersed nicely. The bright edges of the calcined Fe-Stöber sample might indicate that more Fe nanoparticles are anchored to the spheres. The edges are not so smooth as in Fig. 6.2, indicating that something is present on the spheres, probably iron nanoparticles. These iron particles may be too small to be observed directly with the limited resolution in SEM.
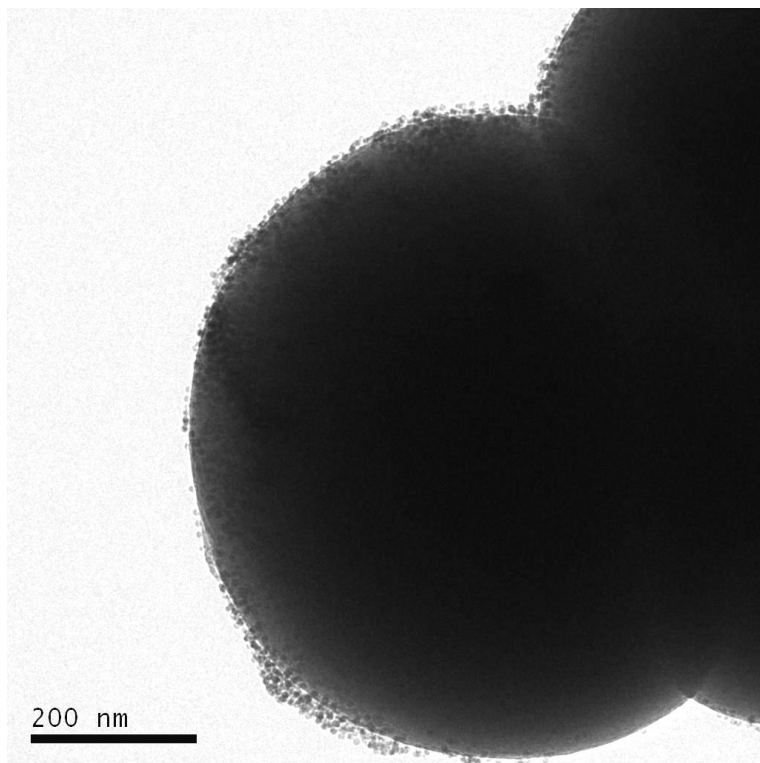
Figure 6.5: TEM image of the calcined Fe-Stöber sample

The TEM image of the calcined Fe-Stöber sample (Fig. 6.5) shows that the 10 nm iron nanoparticles are indeed present on the outer surface of the Stöber spheres. The particles were on all spheres, covering a large part of their surface. No loose iron nanoparticles could be seen, i.e. which were not anchored to a sphere. At some spheres, the nanoparticles were clustered together, forming a larger field of particles on the Stöber sphere. These iron nanoparticle clusters are probably the bright spots which could be observed with SEM. However, most particles were present as separate particles on the SiO_2 support, as shown in figure 6.5.

XPS spectra of the calcined Stöber spheres and the two Fe-Stöber samples are shown in figure 6.6. The spectrum of the calcined Stöber spheres showed only a small C 1s peak at 284.5 eV, which can be attributed
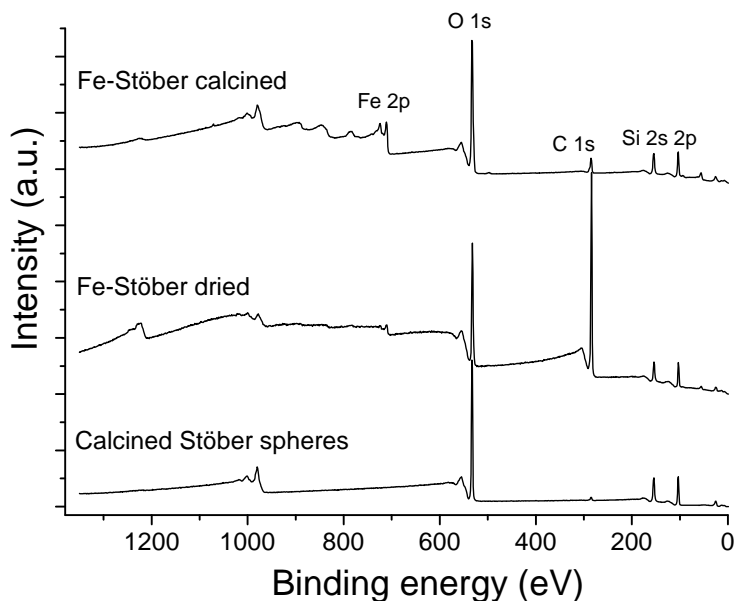
Figure 6.6: XPS spectra of the calcined Stöber spheres and the dried and calcined Fe-Stöber samples

to adventitious carbon, and peaks originating from oxygen and silicon. No nitrogen peak could be observed, indicating that no ammonium ions were present on the sample after calcination.

For the dried Fe-Stöber sample, the main observations are that the area of the carbon peak has increased tremendously and that the Fe 2p peak is visible at 710 eV. The large peak for carbon in the dried sample shows that still a significant amount of oleic acid is present at the surface of the spheres, in agreement with the SEM pictures of Fig. 6.4. The iron signal is relatively weak, which indicates that the oleic acid largely covers the iron.

After calcination at 350 °C, the carbon signal is much smaller, although it cannot be completely ruled out that there is still a minor amount of oleic acid present, since the C 1s peaks for adventitious carbon and the carbon from oleic acid will appear at the same binding energy. However, because most of the carbon has been removed, the Fe 2p peak has grown

significantly and the atomic Fe/Si ratio has more than tripled from 0.06 for the dried sample to 0.19 for the calcined Fe-Stöber sample. The spectrum of the Fe 2p region indicates that iron at the surface of spheres is present as Fe^{3+}.

For this spherical model catalyst, XPS will detect iron preferentially, since iron is only present at the outer surface of the spheres. Because XPS is surface sensitive, the concentration of iron will thus be overestimated, since a large part of SiO_2 support is not detected.

Figure 6.7 shows the XRD pattern of the calcined Fe-Stöber sample. Several diffraction peaks of iron oxide can be observed. The large broad feature around $2\theta = 24\,^{\circ}$ is attributed to the amorphous SiO_2 support (PDF #29-0085).

The diffraction lines of iron fit well with the reference pattern of maghemite (γ-Fe_2O_3), so it can be assumed that the iron particles at the surface of the spheres are maghemite nanoparticles. However, the
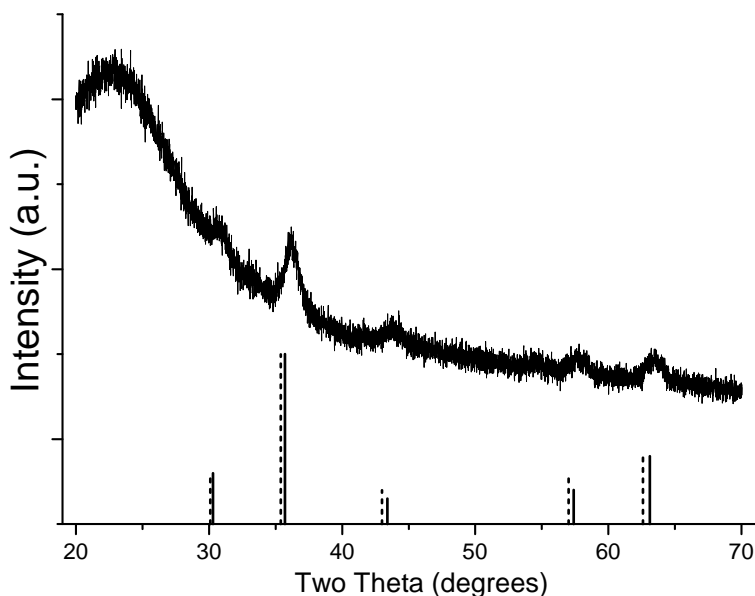

Figure 6.7: XRD pattern of the calcined Fe-Stöber sample. The reference patterns of maghemite (γ-Fe_2O_3, solid lines) and magnetite (Fe_3O_4, dashed lines) are indicated

diffraction pattern for magnetite (Fe_3O_4) does not differ much from maghemite [14], but since the XPS Fe 2p spectrum shows a distinct satellite peak at 719 eV, which is characteristic for Fe^{3+} [15], it is assumed that the iron particles in the calcined Fe-Stöber sample are present as maghemite.

6.4 CONCLUSIONS

The aim of the research described in this chapter was to prepare a high surface area model catalyst, involving colloidal uniform nanoparticles on a non-porous support.

It has been shown that Stöber spheres with diameters between 850 - 900 nm could be synthesized with a relatively small size distribution. These spheres can serve as a model support for well-defined powder iron/SiO$_2$ model catalysts.

The impregnation of iron nanoparticles on these Stöber spheres resulted in a dispersed Fe/SiO$_2$ model catalyst, which can be studied with both electron microscopy and XPS on one hand and with XRD and other bulk characterization techniques on the other hand.

The Stöber sphere powder constitute an excellent, well-defined model system with properties in between the simplified flat model catalyst and a real supported powder catalyst. This will allow for measurements of catalytic activity in micro-reactors, where diffusion problems are kept at a minimum and where both surface science techniques and bulk techniques can be applied. This model catalyst is also eminently suited for studying particle morphology in transmission electron microscopy.

REFERENCES

[1] P. L. J. Gunter, J. W. Niemantsverdriet, F. H. Ribeiro and G. A. Somorjai, Catalysis Reviews 39 (1997) 77–168.

[2] P. C. Thüne, C. J. Weststrate, P. Moodley, A. M. Saib, J. van de Loosdrecht, J. T. Miller and J. W. Niemantsverdriet, Catalysis Science & Technology 1 (2011) 689–697.

[3] P. Thüne, P. Moodley, F. Scheijen, H. Fredriksson, R. Lancee, J. Kropf, J. Miller and J. W. Niemantsverdriet, The Journal of Physical Chemistry C 116 (2012) 7367–7373.

[4] A. K. Datye and N. J. Long, Ultramicroscopy 25 (1988) 203–208.

[5] A. K. Datye, Topics in Catalysis 13 (2000) 131–138.

[6] E. de Smit and B. M. Weckhuysen, Chem. Soc. Rev. 37 (2008) 2758–2781.

[7] N. A. M. Nasir, N. A. M. Zabidi and C. F. Kai, Journal of Applied Sciences 11 (2011) 1391–1395.

[8] W. Stöber, A. Fink and E. Bohn, Journal of Colloid and Interface Science 26 (1968) 62–69.

[9] G. H. Bogush, M. A. Tracy and C. F. Zukoski, Journal of Non-Crystalline Solids 104 (1988) 95–106.

[10] T.-S. Deng, Q.-F. Zhang, J.-Y. Zhang, X. Shen, K.-T. Zhu and J.-L. Wu, Journal of Colloid and Interface Science 329 (2009) 292–299.

[11] C. A. C. Escobedo, J. M. noz Saldaña, D. J. Vigueras and F. J. E. Beltran, Materials Science Forum 509 (2006) 187–192.

[12] T. Hyeon, S. S. Lee, J. Park, Y. Chung and H. B. Na, Journal of the American Chemical Society 123 (2001) 12798–12801.

[13] A. M. Saib, A. Borgna, J. van de Loosdrecht, P. J. van Berge, J. W. Geus and J. W. Niemantsverdriet, Journal of Catalysis 239 (2006) 326–339.

[14] K. Woo, J. Hong, S. Choi, H.-W. Lee, J.-P. Ahn, C. S. Kim and S. W. Lee, Chemistry of Materials 16 (2004) 2814–2818.

[15] T. Yamashita and P. Hayes, Applied Surface Science 254 (2008) 2441–2449.

7

Conclusions and Outlook

How does olivine change during exposure to the different conditions, representative for gas environments present in indirect biomass gasification reactors and how does this behavior relate to the performance of olivine as a biomass gasification catalyst? These are central questions in the research project that is reported in this thesis. This chapter summarizes results, obtained with different characterization techniques and these results are related to the performance of olivine as a biomass gasification catalyst. Since the process conditions influence the state of olivine to a large extent, considerations are presented to optimize the catalytic functionality of olivine.

7.1 DYNAMIC OXIDATION AND REDUCTION BEHAVIOR

Olivine is a useful bed material for reducing tar in indirect biomass gasification, thanks to its dynamic oxidation and reduction behavior. The iron migrates to the surface in oxidizing environments and is reduced to a catalytically active phase in reducing environments.

In this work, this dynamic behavior was investigated with both bulk and surface sensitive characterization techniques, as described in chapters 3 and 4. SEM-EDS analysis of the cross-section of an olivine particle showed that the iron-silicate and magnesium-silicate phases in olivine are not homogeneously distributed, but are present as distinctly different Fe- and Mg- rich domains. This is schematically illustrated in Fig. 7.1a.

In an oxidizing environment, SEM shows the formation of iron-oxide crystallites at the surface and an inhomogeneous material. XPS shows surface enrichment of Fe, primarily at the expense of Si. This was interpreted as segregation of Fe out of Fe-rich domains, as schematically shown in figure 7.1b.

If the oxidation is sustained for a longer time (Fig. 7.1c), more iron will be extracted from the olivine matrix to form free iron phases, where iron
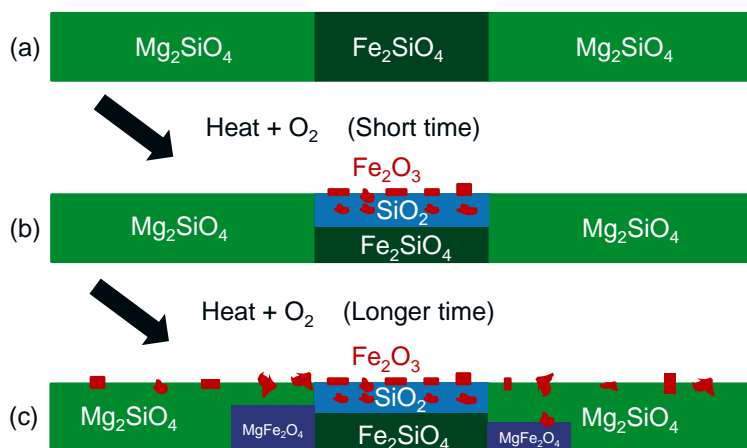

Figure 7.1: Schematic representation of (a) untreated olivine, (b) olivine after oxidation for a short time and (c) olivine after oxidation for a long time

is not present as silicate, as seen by XPS. Mössbauer Spectroscopy showed that these free iron phases can exist as iron-oxide or as magnesioferrite ($FeMg_2O_4$). XPS results showed that during oxidation for 1 h, iron was also replacing Mg at the outer surface , where iron then is present as Fe^{3+}. This was explained by diffusion of Fe from Mg-rich parts of the olivine.

Mössbauer spectroscopy and XRD revealed that in the 'fresh' olivine from Magnolithe GmbH in Austria, a commonly used olivine for biomass gasification, around 45% of the iron was extracted from the olivine phase after a 3 h pretreatment at 1600 °C, performed by the mineral supplier. Since the samples used in this work have been exposed to such a high temperature prior to experiments, it may seem counterintuitive that additional iron extraction was observed. This is caused by difference in grain size; during the suppliers pretreatment, the grain size was around 30 mm, whereas the olivine particle size during the research presented in this thesis was much smaller, with a maximum particle size of 500 micrometer.

After oxidation for 1 h, XPS in combination with depth profiling showed that the iron surface concentration increased from 1 at.% in the fresh material to 6 at.% in material after oxidation. An iron rich surface layer of 400 nm was observed, in which the iron concentration decreased exponentially from the outer surface concentration of 6% to 2%, which is still double the bulk concentration of fresh olivine. Moreover an additional 7% of iron was extracted from the olivine matrix and 20% of iron was present as Fe_2O_3.

When the surrounding gas atmosphere is switched from an oxidizing environment to a reducing environment containing only H_2, the free iron-phases at the surface of pre-oxidized olivine quickly reduce to from metallic iron.

XPS showed that this reduction of olivine in H_2 takes place on two time scales, as shown in Figure 7.2. The fast process, from Fig. 7.2a to b, is associated with the reduction of the surface iron, mostly present at the surface of Fe-rich parts of the olivine. This fast reduction re-exposed silicon at the surface. Moreover, the size of the iron crystallites decreased, as observed in SEM pictures. This is because the size of metallic iron
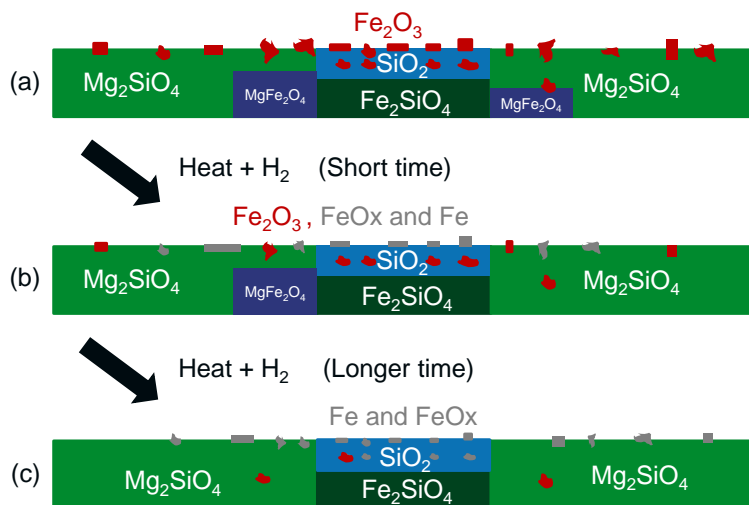
Figure 7.2: Schematic representation of (a) oxidized olivine during reduction in hydrogen (b) for a short time and (c) after a longer time

particles is smaller than the size of iron-oxide particles, containing the same amount of iron.

When olivine is reduced for longer times, from Fig. 7.2b to c, the iron surface concentration decreases further. XPS depth profiling showed that during reduction for 1 minute, only the upper 100 nm of the iron-rich surface layer is affected, whereas if the reduction is carried out for 1 hour, the iron concentration in the entire surface layer decreases to the bulk value of 1%, as observed for fresh olivine.

During reduction in H_2, part of the iron, present as $MgFe_2O_4$ phases, reintegrates back into the olivine matrix, as indicated by Mössbauer spectroscopy. The remaining $MgFe_2O_4$ phases are converted to metallic iron.

Since H_2 is only one of the reducing gases present in indirect biomass gasification reactors, treatments were also carried out with CO as the reducing agent, as shown in Fig. 7.3.

With CO present in the gas environment of pre-oxidized olivine, the iron at the surface reduces from mostly Fe^{3+} to a combination of Fe^{2+} and Fe^0-dominated iron phases, such as Fe_3O_4, FeO, metallic iron and
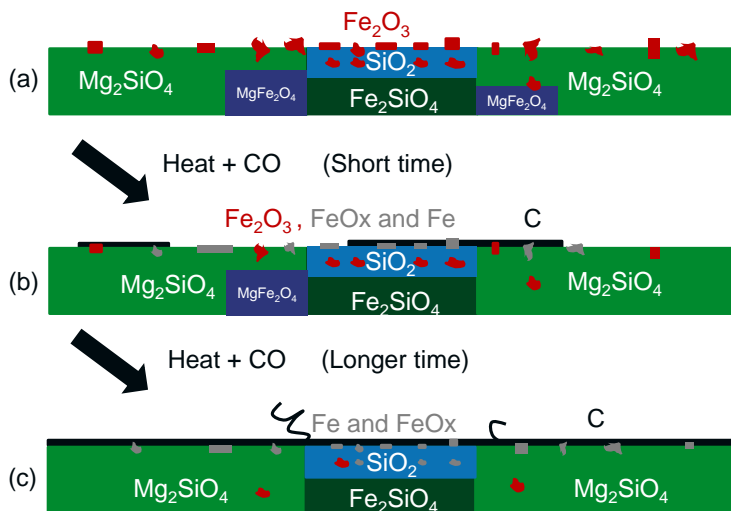
Figure 7.3: Schematic representation of (a) oxidized olivine during treatment in a CO-containing gas environment (b) for a short time and (c) after a longer time

iron carbide. XPS showed that the iron surface concentration decreased again, after the increase during oxidation. However, the most important change at the surface is that reduction in CO-containing gas leads to a rapid build-up of carbon on the surface of the particles. After one minute, the carbon surface concentration already reaches 10 at.% and after reduction for 1 h in CO, more than 90% of all surface atoms detected by XPS is carbon.

This carbon deposition is caused by the Boudouard reaction, in which CO is converted to solid carbon and carbon dioxide. Moreover, SEM analysis of a sample, which was reduced in a mixture of CO and H_2 showed the presence of carbon fibers. This carbon deposition is undesired in view of the use of olivine as a tar degradation catalyst, since the carbon blocks the catalytically active sites of the material and decreases the CO and H_2 content in the product gas.

7.2   CHANGES DURING USE IN INDUSTRIAL GASIFICATION REACTORS

When olivine is used as a circulating bed material in indirect biomass gasification reactors, the gas environment of the olivine changes twice every cycle, from an oxidizing to a reducing environment and from the reducing environment back to the oxidizing environment. Apart from the changes in the olivine properties described in figures 7.1, 7.2 and 7.3, some long term changes related to the alternation in chemical environment occur as well.

In the ECN MILENA process, the combustor zone is a bubbling fluidized-bed, where the residence time of the olivine is relatively long. Therefore, when the bed material particles enter the gasification zone, the olivine can be seen as oxidized. The surface of oxidized olivine is rich in iron, present primarily as Fe_2O_3, but other free iron-phases, such as Fe_3O_4 and $MgFe_2O_4$, are present in the material as well.

When the oxidized olivine is circulated to the gasification zone, the environment changes to a reducing environment, where the gas atmosphere contains H_2 and CO. The residence time in this zone is dependent on the design of the indirect biomass gasification system. The ECN MILENA process uses a riser reactor as the gasification zone, where the residence time of the bed material and the gas phase is less than one minute. This residence time is too short for complete reduction of all free iron phases. The free iron phases at the surface reduce quickly, but the iron-oxide and $MgFe_2O_4$ phases inside the material do not reduce completely.

Since CO is present in the gas phase, carbon deposition on the surface of the particles can occur immediately. However, since the residence time in the CO containing environment is short, active surface, which is not covered by carbon, is still available for catalytic reactions. XPS results showed that if carbon-covered olivine is exposed to oxidizing conditions, the accumulated carbon is quickly combusted and the original surface of olivine is recovered. This is schematically shown in figure 7.4a.

Experiments with short (1 min) alternating air and CO treatments showed that the surface of olivine adapts quickly to the surrounding gas environment. After each oxidation step, the amount of surface iron
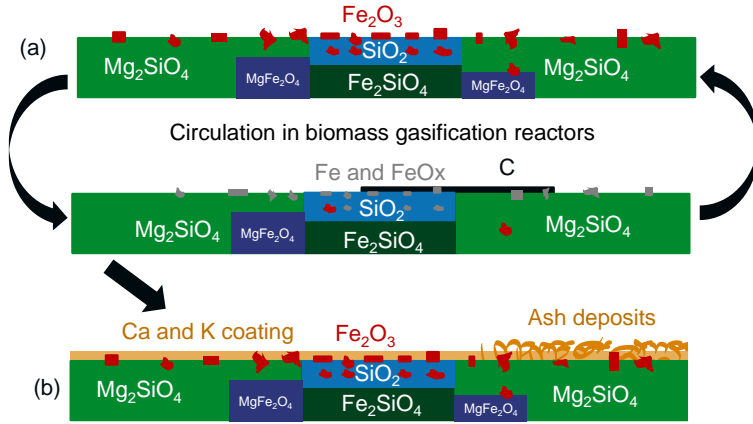
Figure 7.4: Schematic representation of the changes in olivine during use as circulating bed material

increased significantly, whereas the opposite was observed after reduction in CO.

When these short cycles are repeated for an increased number of times, the same long term effect that was observed for the longer treatments occurs, i.e. surface iron increase at the expense of magnesium. The absolute concentration of iron at the surface increases with increasing number of treatments.

Furthermore, accumulation of carbon on the surface is not observed, even not after repeated cycles, indicating the all carbon that is deposited on the olivine is combusted during each cycle.

The oxidation of iron in the combustion zone and the subsequent reduction in the gasification zone implies that the iron in olivine transports oxygen from the combustor to the gasifier. Because this oxygen is released in the gasification zone, the process requires less steam as a gasifying agent. The oxygen-transport capability of olivine was investigated in the research described in chapter 4.

TGA was used to quantify the oxygen transport under realistic process conditions. TGA result indicated that at least 18% of all the iron in olivine actively participates in the oxygen transport. The oxygen transport amounted 0.5 wt.% of the olivine bed material. Given the high percentage

of iron that participates in oxygen transport, this indicates that oxygen transport can not only be a surface phenomenon, even on short time scales. The iron in the subsurface iron-rich phases also contributes to these gas phase interactions.

Apart from the gas phase, the olivine also interacts with the biomass particles and the gasification residues when used as circulating bed material. This interaction results in the formation of a coating on the bed material particles formed by components originating from the biomass ash, as shown in Fig. 7.4b. This coating consists of calcium-, potassium- and magnesium oxides or carbonates and has a chemical similarity with the mineral dolomite (CaO-MgO). The coating increases the tar degradation and enhances the production of hydrogen from the biomass. The ash deposits on the bed material also nearly doubled the surface area of the particles, since the formed coating layer is porous.

The nature of this coating and its influence on the reactivity of olivine were investigated in chapter 5 and a mechanism for the coating formation was suggested. Coated olivine is much more active in the water-gas shift reaction compared to uncoated olivine and this is attributed to the combined presence of calcium, potassium and carbonate species at the surface. Moreover, the increased porosity is an advantage in view of tar removal from the gasification zone in indirect gasification systems.

7.3   IMPLICATIONS FOR INDIRECT GASIFICATION PROCESSES

Since tar formation is one of the main problems during indirect biomass gasification, it is desirable to reduce the tar concentration in the product gas as much as possible. This can in principle be done in four ways: 1) Prevent the formation of tars during the gasification process, 2) Transport the tars together with the bed material to the combustion zone, where the tars are combusted, 3) Convert the tars inside the gasification zone or 4) Remove the tars in a separate step after gasification.

To prevent tar formation in the gasification zone, the gasification process should be performed at very high temperature and high pressure, conditions which are not suitable for gasification of biomass. Tar transport or conversion is typically done by the circulating bed material in

indirect biomass gasification. Although, when using olivine as a primary catalyst, a large fraction of the tars produced inside the gasification zone can be removed. However, the product gas will not be completely free of tars when it leaves the gasification reactor. If the product gas is used to produce hydrogen, SNG or chemicals, it interacts with other catalysts downstream. These are usually catalysts in fixed-bed reactors which can easily be poisoned by pollutants in the gas stream. Therefore, industrial biomass gasification systems have a gas cleaning system downstream of the gasification reactor. ECN, for example, has developed the OLGA gas cleaning technology, in which tars can be removed to a level where the tar dewpoint is below 5 °C. This makes the product gas clean enough to perform for instance the Fischer-Tropsch synthesis. Despite the possibility of producing a tar-free product gas by after treatments, tar conversion inside the gasification zone is still desirable, since it increases the total energy efficiency of the indirect gasification process and decreases risk for fouling in the reactor and pipes.

The good thing about olivine as a catalytic bed material is that it is activates itself by its dynamic behavior. On the downside, it is difficult to prepare olivine in an optimal form and it is hard to predict how the optimal catalytic activity of olivine can be achieved, since it has been shown in this work that the olivine adapts very quickly to its surrounding gas environment. This gas environment in turn, depends on the process control parameters, including temperature, type of biomass, feed rate of biomass and steam, residence time in the different zones, etc. etc. This does, however, not mean that a steady-state operation cycle is readily reached, even if the control parameters are fixed. Several slow, long term changes in olivine have been observed which may contribute to a change in the catalytic behavior. These changes, including iron surface enrichment, oxygen transport and coating formation will influence the process parameters.

If one considers a gasification experiment, based on the results of this work, the optimal olivine catalyst will have a significant amount of free iron at the surface and a porous coating consisting of ash components. The porous coating facilitates tar absorption on the bed material. If free iron phases, in the appropriate oxidation state, are present at the surface

as well, they can catalytically convert the tar to CO and H_2. Moreover, the catalytically active ash components at the surface increase the WGS reaction rate and are able to convert tars on their own as well , thereby increasing the energy content of product gas.

To bring and keep fresh olivine in the most active state, it should be activated by the gasification process itself. This activation increases the iron surface concentration and induces coating formation. In the combustor section, iron is extracted from the olivine matrix to form free iron phases. These iron phases should be subsequently reduced to make them catalytically active. Since this reduction takes place inside the gasification zone by gases present there, the residence time in the gasification zone should not be too short. At intermediate residence time (>10 s), there is a longer contact time between the bed material, the biomass and the surrounding gas environment, thus allowing the catalyst to reduce and convert tars.

During these processes, the olivine will get the desired coating by interaction with the biomass ash. However, this coating formation can be accelerated by adding additives to the gasification reactor, which contain the active components that are present in the biomass ash, such as CaO.

This work contributes with important information on the fundamental properties of olivine, when it is used as catalytically active bed material in indirect biomass gasification. Significant changes in surface chemistry and morphology were observed. Iron, a well-known catalytic material, is highly mobile in olivine. This high mobility leads to redox behavior and oxygen transport. Moreover, during use, a Ca-rich layer will form on the bed material, which influences its reactivity.

These observations contribute to revealing the details of the catalytic processes in biomass gasification and will help selecting the optimal process conditions to achieve optimal performance for indirect gasification reactors.

DANKWOORD

Eindelijk is het af! De promotie-tijd is voor mij bijzonder leerzaam geweest en dat niet alleen op inhoudelijk vlak. Het was interessant, verbredend, uitdagend, gezellig en soms ook moeilijk. Nu deze tijd dan toch echt bijna voorbij is, wil ik graag een aantal mensen bedanken die bijgedragen hebben aan het succesvol volbrengen van mijn promotie-project.

Allereerst mijn promotor, Hans Niemantsverdriet. Beste Hans, allereerst wil je bedanken dat je mij de mogelijkheid wilde bieden om mijn project bij jou in de groep uit te voeren. Je bent altijd erg betrokken bij je promovendi en bij vragen of problemen kunnen we altijd binnenlopen. Graag wil ik je ook ontzettend bedanken voor alle kansen die je me geboden hebt om mezelf te ontwikkelen, o.a. door mijn werk te presenteren op verschillende conferenties in binnen- en buitenland en mij te betrekken bij projecten die niet direct gerelateerd aan mijn onderzoek waren. Graag wil ik je heel veel succes wensen met je nieuwe uitdaging in China en ik weet zeker dat daar met jouw kennis, kunde en drive al snel hoogstaand onderzoek gedaan zal worden.

Ook wil ik graag mijn tweede promoter Hubert Veringa bedanken. Beste Hubert, jouw kennis op het gebied van biomassa en vergassing is zo groot dat gelijk aan het begin van het project de juiste onderzoeksvragen gesteld werden en er voortvarend gestart kon worden. Ook zorgde je ervoor dat tijdens meetings, waar we soms verdwaalden in te wetenschappelijke details, nooit het overall plaatje uit het oog verloren werd. Zo werd alles goed in perspectief geplaatst en is er een mooi samenhangend werk uitgekomen.

Hans Fredriksson, ook jij heel erg bedankt voor je enthousiasme waarmee je mij dagelijks in en buiten het lab begeleid hebt. Door jouw ervaring heeft het project een bliksemstart gehad. Als een experiment niet veelbetekenend leek voor mij zag jij er soms een mooie aanleiding voor verder onderzoek in en dat heeft geleid tot mooie publicaties. Ook heb je ervoor gezorgd dat mijn schrijfkunsten heel erg verbeterd zijn door je altijd snelle en uitgebreide commentaar. Bedankt voor alles!

De overige leden van mijn promotiecommissie, prof. Hofbauer, prof. Kersten, prof. Hensen en dr. Van der Meijden, bedank ik voor hun deelname aan de commissie en het lezen en becommentariëren van dit proefschrift in een vroeg stadium.

Zonder de technische ondersteuning van Tiny was het zeker niet zo goed gelopen als dat het gegaan is. Tiny, bedankt voor al je hulp in het lab en daarbuiten. Buiten een uitstekend technicus ben je ook een bijzonder fijn persoon. Vooral de BBQ en muziek avonden in Landhorst waren legendarisch en zorgden zowel daar als bij ons voor mooie verhalen.

Ook wil ik graag Peter Thüne bedanken voor zijn hulp in het begin van het project, waar ik helaas door omstandigheden niet lang gebruik van heb kunnen maken.

Paul Hamers (TGA), Iulian Dugulan (Mössbauer) en Adelheid Elemans (ICP), bedankt voor de hulp met de experimenten die ik zelf niet kon uitvoeren. Ook de administratieve ondersteuning van Thérèse-Anne, José en Agnes was onmisbaar.

De mensen bij ECN, in het bijzonder Christiaan van der Meijden, Rian Visser en Sander Grootjes, wil ik graag bedanken voor hun bijzonder nuttige input gedurende het project. Hierdoor werd de wetenschap snel aan de praktijk gekoppeld, waardoor ik weer extra gemotiveerd raakte.

Alle groepsgenoten van de PCS groep wil bedanken voor de gezelligheid en gevraagd en ongevraagd advies: Kees-Jan, Tiny, Gilbère, Jasper, Emad, Deshen, Yibin, Huapeng, Chenghua, Zhenghang, Ajin, Ali, Basar, Olush en Antonio. Ook de buitenlandse gasten in het kantoor: Tyne, Jonathan and Amanda (Stöber-buddy!), thanks for all the fun!

Special thanks for you Emad, for all your help in preparing the Stöber-spheres and the model-catalysts! Hope we can extend this concept further!

Koen, mijn enige student, ook jij bedankt voor je bijdrage in de tot-standkoming van hoofdstuk 6!

Gilbère, Tiny, Arjan, Jarno, Jasper, Andreas, Coen, Dennis, Mariët, Iris, Jos, Gijsbert, Esther, Giulia, James, Ivo, William, Yoran, Bart, Arno, Leen, Sabriye, Hans F., Erik, Dieter, Christian, Adelheid, Ad, Jan en iedereen die ik hier vergeten ben, bedankt voor alle gezelligheid gedurende de koffie- en lunchpauzes, in de F.O.R.T. en bij de vrijdagborrel en tijdens alle spontane ad-hoc-borrels!

Gilbère, bedankt voor het organiseren van de SKA-tripjes naar de meest uiteenlopende bestemmingen, met als onbetwist hoogtepunt ons avontuur in Noord-Korea. Jarno, Matthijs, Andreas, Coen, Tiny, Arjan en Jasper, bedankt voor de gezelligheid tijdens deze avonturen!

Ook bleken sommige contacten, gelegd tijdens conferenties, heel waardevol als het wetenschappelijk programma ten einde was. Vooral Ewa, Tatyana en Ilona wil ik graag bedanken voor alle gezelligheid tijdens en vooral ook na deze verschillende conferenties en Summerschools.

Bij mijn tweede baan in het Parktheater kon ik altijd goed mijn zinnen verzetten. Alle collega's, in het bijzonder mijn receptie-collega's Tom, Arjan, Nic, Jan, Rob en Etiënne, bedankt voor alle mooie borrels, uitjes en sluitdrankjes.

Ontspanning buiten en tijdens het werk is ook bijzonder belangrijk. Maurice, bedankt voor je vriendschap, alle mooie theater-avondjes, het consequent volhouden van het zwemmen 's ochtends en onze mooie "cultuur"-reis naar Schotland!

Mariët, heel erg bedankt voor alle (opstart-)koffie-breaks en de vele avonden gezelligheid, waarbij we het regelmatig moesten opnemen tegen de kabouters.

Ook in onze nieuwe straat is het vaak erg gezellig: Eddy en Mariëlle, Jolanda en Maarten en Niels en Brigitte, hopelijk volgen er nog vele mooie buurt-borrels!

Mijn vrienden binnen en buiten Eindhoven: Joep, Jorien (bedankt voor de cover!), Marijne, Marloes, Mark, Paul, Robin, Yvette en iedereen die ik vergeten ben, bedankt voor jullie interesse in mijn promotie-traject en de nodige ontspanning.

Familie, schoonfamilie, pap, mam en Bart, bedankt voor jullie steun en belangstelling in wat ik de afgelopen vier jaar op de universiteit heb uitgespookt. Ik hoop dat ik het uiteindelijk toch een beetje begrijpelijk heb gemaakt.

Als laatste wil ik heel graag mijn lieve vriendin bedanken. Ellen, bedankt voor je onvoorwaardelijke steun voor alles wat ik doe. Je hebt het soms best lastig met mij, maar samen zijn we altijd overal gekomen waar we wilden zijn! Bedankt voor alles!

CURRICULUM VITAE

Remco Lancee was born on September 6, 1984 in Utrecht, where he lived for 4 years. After having moved to the small village of Nuenen, near Eindhoven, he graduated for his Gymnasium diploma at the Lorentz Casimir Lyceum in 2002. In that same year, he started studying Chemical Engineering and Chemistry at the Eindhoven University of Technology. He was an active member of the study association "Jan Pieter Minckelers" where he, amongst others, managed the student bar, organized the Eindhoven career event and took care for the festivities accompanying the 50th anniversary of the study association.

During his studies, Remco went abroad for 5 months for his industrial internship. He investigated novel supports for Fischer-Tropsch catalysts at the Institute of Chemical and Engineering Sciences in Singapore.

In February 2010, he obtained his Master of Science degree under supervision of prof.dr.ir. Emiel Hensen. His graduation project focused on the design of optimal Rh-based catalysts for steam reforming of methane.

In May of that same year, he started his PhD research under supervision of prof.dr. Hans Niemantsverdriet and prof.dr. Hubert Veringa. The most important results of this work are described in this thesis.

LIST OF PUBLICATIONS

Journal Publications:

- <u>Remco J. Lancee</u>, A.J. (Sander) Grootjes, Christiaan M. van der Meijden, Hubert J. Veringa, J.W. (Hans) Niemantsverdriet and Hans O.A. Fredriksson: *Characterization and Reactivity of Ca-rich Bed Material Coating, formed during Indirect Biomass Gasification*, Manuscript in preparation.

- <u>Remco J. Lancee</u>, A. Iulian Dugulan, Peter C. Thüne, Hubert J. Veringa, J.W. (Hans) Niemantsverdriet and Hans O.A. Fredriksson: *Chemical Looping Capabilities of Olivine, used as a Catalyst in Indirect Biomass Gasification*, Applied Catalysis B: Environmental 145 (2014) 216–222.

- Hans O.A. Fredriksson, <u>Remco J. Lancee</u>, Peter C. Thüne, Hubert J. Veringa and J.W. (Hans) Niemantsverdriet: *Olivine as tar removal catalyst in biomass gasification: Catalyst dynamics under model conditions*, Applied Catalysis B: Environmental 130–131 (2013) 168–177.

- Peter Thüne, Prabashini Moodley, Freek Scheijen, Hans Fredriksson, <u>Remco Lancee</u>, Jeremy Kropf, Jeffrey Miller and J.W. (Hans) Niemantsverdriet: *The Effect of Water on the Stability of Iron Oxide and Iron Carbide Nanoparticles in Hydrogen and Syngas Followed by in Situ X-ray Absorption Spectroscopy*, Journal of Physical Chemistry C 116 (2012) 7367–7373.

Conference Presentations:
<u>Oral</u>:

- North American Catalysis Society Meeting
  Louisville, KY, United States, June 2013

- Annual Meeting of the American Institute of Chemical Engineers
  Pittsburgh, PA, United States, October 2012
  "Best Presentation of Session"-Award

- Advances in Catalysis for Biomass Valorization
  Thessaloniki, Greece, July 2012

Poster:

- North American Catalysis Society Meeting
  Detroit, MI, United States, June 2011

- Netherlands Catalysis and Chemistry Conference
  Noordwijkerhout, The Netherlands, March 2011